From: FNAL::IN%"BRACKER@fnalv.fnal.gov" 7-MAR-1994 00:05:41.49
To: IN%"SANDRA@lafex.CBPF.BR", IN%"JANJOS@LAFEX.CBPF.BR", IN%"BEDIAGA@lafexsu1.lafex.cbpf.b
CC:
Subj: Getting It Right

Return-path: <BRACKER@fnalv.fnal.gov>
Received: from FNAL.FNAL.GOV by FNAL.FNAL.GOV (PMDF V4.2-12 #3998) id
<01H905HOLT5I001GNY@FNAL.FNAL.GOV>; Mon, 7 Mar 1994 00:04:19 CDT
Date: Mon, 07 Mar 1994 00:01:44 -0600 (CST)
From: BRACKER@fnalv.fnal.gov
Subject: Getting It Right
To: SANDRA@lafex.CBPF.BR, JANJOS@LAFEX.CBPF.BR, BEDIAGA@lafexsu1.lafex.cbpf.br
Resent-message-id: <01H905HOLT5K001GNY@FNAL.FNAL.GOV>
Message-id: <940307000144.2760fde2@FNALV.FNAL.GOV>
X-VMS-To: IN%"SANDRA@lafex.CBPF.BR", IN%"JANJOS@LAFEX.CBPF.BR",
IN%"BEDIAGA@lafexsu1.lafex.cbpf.br"
Content-type: TEXT/PLAIN; CHARSET=US-ASCII
Content-transfer-encoding: 7BIT

Getting It Right

Steve Bracker
March 6, 1994

Traditionally, the first thesis out of each TPL experiment has become a mini-reference manual for the experiment as a whole, often consulted years later by people working on subsequent experiments. In general, this is a tradition I disapprove of; I believe that it's much better for a thesis to focus quite narrowly on its essential subject matter (thus maximizing the probability that people on the committee will actually read it), and simply to cite references to descriptions of apparatus not central to the student's analysis. However, if the student, adviser, thesis committee or whoever decides that a thesis should be padded with an overview of the entire experiment, then some substantial attempt should be made to get the information right, because there's always the chance that other people may read it and believe it.

I have read that part of Pauline's thesis dealing with triggering and data acquisition. It is replete with serious errors. Since a detailed understanding of these systems is not vital to carrying out the form factor analysis that is the essential subject matter of the thesis, there is no reason to believe that the physics in the thesis is in any way compromised. But if that be so, why is the Trigger and Data Acquisition section in the thesis at all? Given that it is present, why wasn't it reviewed by someone familiar with triggering and data acquisition before the thesis was published?

Among the many problems in section 3 (starting on page 45):

"The signal from the interaction counter was required to be at least as large as the mean signal from five charged particles." [p. 45] The threshold is set to 4-5 times the signal from a minimum ionizing (minimum signal) particle.

"This weighted sum gave an estimate of the total energy in an event for the trigger decision." [p. 45] There are actually two calorimeter energy

sums in the trigger: an unweighted sum to measure total energy, and a weighted sum to measure transverse energy. The unweighted sum was used to veto events with multiple beam particles (>700 GeV total energy); the weighted sum was used to reject events with low transverse energy.

Table 3.1: The total energy veto (last entry) looks for multiple beam particles in a narrow time window around the event, not multiple interactions (which with a single 500 GeV beam particle still cannot produce 700 GeV of total energy).

"The average time between beam particles was about 500 ns. Since this is greater than the 470 ns to make the full trigger decision, there was very little deadtime due to the trigger decision." [p. 47] This would be true only if the particles were arriving at exactly 500 ns intervals; if 470 ns of deadtime were incurred for each particle arriving (randomly distributed at an average rate of 2 megahertz), the trigger-induced deadtime would be quite large. The real reason that trigger deadtime is low is that most pretriggers required an interaction, which occurred only every 20-25 microseconds; that is the number that 160 ns or 470 ns should be compared to.

"[The DA system] was designed to accept large bursts of data at a faster rate than it could fully process them but made use of dead time in the beam delivery structure to process and record the data to memory in a continuous manner." [p. 48] In fact the in-spill data burst was recorded real-time in MEMORY so it could be processed and written to TAPE during the entire spill cycle (spill and interspill).

"The DA is composed of three major components: memory buffers, event buffer interfaces and Exabyte tape drives." [p. 48] That is an odd emphasis given the fact that the behavior of the system is totally determined by programs running in the 54 ACP PROCESSORS and the VAX. By comparison, the Event Buffer Interfaces are trivial protocol translators between the VME bus and the memory buffers.

"This parallel structure of the DA allowed 24,000 channels to be read out in 50 [microseconds]...." [p. 48] This is at least seriously misleading. Most of the deadtime reduction is due to very fast digitizing systems and readout controllers which send data to the DA system. Only about 5% of the channels report any data at all for a typical event. The DA system does make a contribution to low deadtime readout by providing parallel input paths, but most of the reason that 24000 channels can be read out in 50 microseconds lies upstream of the DA.

Table 3.3 (p. 48): The typical event length is 2.5 (not 1.5) kilobytes. The 9000 events/second is correct for the spill (as noted in the text above the table), but is misleading following as it does the continuous (spill + interspill) bandwidth. The event rate averaged over an entire spill cycle is about 23/58 x 9000 = 3570 events/second. Multiplying that event rate times the (incorrect) event size of 1.2 kilobytes per event yields a continuous rate to tape of 4.28 (not 9.6) megabytes/second; table 3.3 is not even self-consistent.

"The eight EFB's provided a total of 640 Mbytes of memory, enough to store one spill of data." [p. 48] That's not right. The EFBs need store only enough data to keep the system downstream of them running during the interspill, about 60% of a spill's data. Storing a full spill would only make sense if the buffers could only read or write (but not both) at any one time. We went to a great deal of trouble to ensure that the buffers could read and write at full bandwidth concurrently; that's an essential

aspect of the design.

If you multiply 9.6 megabytes per second by 58 seconds per spill cycle, a full spill cycle's data (going to tape) is 557 megabytes -- small enough, you might think, to fit in a 640 megabyte buffer memory system. But it's actually not true, for two different reasons. First, the buffers do not fill exactly evenly; when the fastest-filling buffer becomes nearly full and inhibits triggers, there is some unused memory left in the others. More important, the events in the buffers are larger than the events going to tape because the additional TDC data compression performed in the Event Handlers has not yet been carried out. The buffers will not (and need not) hold a full spill of data.

All references to ACP II processors (p. 50) are incorrect; the processors used were ACP-1 single board computers, a processor many times slower than an ACP II. The ACP-1 has only about 0.8 Vax-equivalents of computing power. The ACP II processors, abandoned by the Fermilab computing division, are now being used at CBPF to reconstruct a portion of the E-791 data. They were not available for the DA system. Had they been available, the entire DA system configuration would have been very different.

Referring to 3.3.2: The ACP processors are modules distinct from the Event Buffer Interfaces, which are VME cards designed and built at Fermilab by Sten Hansen, myself, and several students. Figure 3.2, a system drawing similar to the one I prepared for my DA talks, makes that clear.

The ACP processors were of two kinds: BOSSES (1 per crate) and EVENT HANDLERS (many per crate). The hardware was identical; the programs were different. The Boss supervised the flow of data through the crate and controlled the tape system; the Event Handlers extracted data from the buffers, assembled complete events, and prepared them for output to tape.

Event Handlers could be in one of two states: GRABBER (responsible for extracting events from the buffers through the EBI) and MUNCHER (processing events already grabbed). Typically grabbership was passed from Event Handler to Event Handler a couple of times per second.

It is impossible to reconcile the first sentence of the second paragraph of 3.3.2 with the rest of that paragraph. It bespeaks fundamental confusion about the design of the DA system.

And so on.... In fairness, if I had to summarize Pauline's form factor analysis, I would flounder at least as badly. I'd either have to study it carefully (and learn a lot of background information beforehand) or write about something else that I understand better. No one can be a specialist on everything in an experiment as big as E-791, but one should try to resist the temptation to just wing it.

Again, two requests directed especially to future thesis writers and their thesis advisers:

(1) Whenever possible, avoid padding theses with information about systems the candidate had little or nothing to do with. Keep the thesis focused on the analysis being presented. If technical details about a system are necessary to support the analysis, cite technical reports written by people who know the system whenever possible, and summarize the significance of those details for the analysis being reported.

(2) If technical information about a system outside the candidate's area of expertise must be included in a thesis for whatever reason, then get it right. Interview the people who worked with the system. Read any publications or internal notes that are available. Have the draft of the chapter checked by someone who knows the system well.

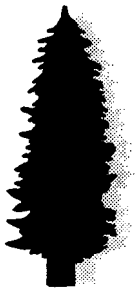

SCIPP 93/47
December 1993

UNIVERSITY OF CALIFORNIA

SANTA CRUZ

MEASUREMENT OF THE FORM FACTORS IN THE SEMILEPTONIC DECAY $D^+ \to \bar{K}^{*0} e^+ \nu_e$

PAULINE GAGNON

A dissertation submitted in partial satisfaction
of the requirements for the degree of
DOCTOR OF PHILISOPHY
in
PHYSICS

ABSTRACT

A measurement of the ratios of the form factors in the semileptonic decay channel $D^{\pm} \to K^{0*} e^{\pm} \nu$ is performed using data collected by the E791 collaboration at the Tagged Photon Spectrometer at Fermilab in a hadroproduction of charm experiment. Charmed events are selected if a secondary vertex of charged tracks is found clearly separated from the primary vertex. Semileptonic events for this particular decay mode are required to have a well identified electron as well as an invariant mass for the (Kπ) system consistent with the $K^*(892)$ mass. The form factors are extracted by comparing the data to a Monte-Carlo-simulated sample using a continuous maximum-likelihood method to simultaneously fit to four kinematic variables characteristic of this decay mode. The measured values for the form factor ratios are $R_2 = 0.32^{+0.26}_{-0.27} \pm 0.13$ and $R_V = 2.4^{+0.39}_{-0.37} \pm 0.27$.

Table of Contents

List of Figures

List of Tables

THESIS ABSTRACT

MEASUREMENT OF THE FORM FACTORS IN THE SEMILEPTONIC DECAY $D^+ \to \bar{K}^{*0} e^+ \nu_e$

Pauline Gagnon

A measurement of the ratios of the form factors in the semileptonic decay channel $D^{\pm} \to K^{0*} e^{\pm} \nu$ is performed using data collected by the E791 collaboration at the Tagged Photon Spectrometer at Fermilab in a hadroproduction of charm experiment. Charmed events are selected if a secondary vertex of charged tracks is found clearly separated from the primary vertex. Semileptonic events for this particular decay mode are required to have a well identified electron as well as an invariant mass for the (Kπ) system consistent with the $K^*(892)$ mass. The form factors are extracted by comparing the data to a Monte-Carlo-simulated sample using a continuous maximum-likelihood method to simultaneously fit to four kinematic variables characteristic of this decay mode. The measured values for the form factor ratios are $R_2 = 0.32^{+0.26}_{-0.27} \pm 0.13$ and $R_V = 2.4^{+0.39}_{-0.37} \pm 0.27$.

Acknowledgements

A celle à qui je dois tout*
(To the one I owe everything)

First of all, I wish to thank my advisor, Pat Burchat, not only for suggesting an interesting and challenging thesis topic, but also and mostly for her continuous support and friendship over the years we worked together. There is no way I can thank her enough for the many hours she took to explain difficult points or guide me through the usually dark world of form factors. Her enthusiasm was stimulating; her patience invaluable! She taught me how to do physics as well as how to enjoy doing it. I am now totally convinced that it does not have to hurt to be good physics.

This work would not have been completed without the support of many dear friends who stood by me throughout these years. I am specially grateful to my friend and collaborator Danying Yi for her friendship, advice, wonderful cooking and excellent humor. I also want to thank my bad weather friend Laura Kay for watching out for me and for always being there during the roughest times (in particular for keeping me going with all those bets about when I'd graduate!); Jolie Pearl for suggesting going back to school and then providing support and comfort when I was ready to give up; Cate Hieke for her continous friendship during my stay in California, her patience over the last six months and her deadly sense of humor when I had nearly lost mine; Marize Pommot-Maia for encouraging me to be my best, her good sense of humor as well as for everything she left behind.

I am very grateful to all my collaborators on the E791 experiment for their support and the excellence of their work. In particular, my life at Fermilab would not have been the same without both the friendship and expertise of Penny Kasper, Jean Slaughter, Sudeshna Banerjee, Tom Carter, Keith Thorne and Jeff Appel.

Special thanks to my collaborators here at Santa Cruz (Guy Blaylock, Judy Leslie, Kathy O'Shaughnessy, Renata Zaliznyak and Katsu Sugano) for all the fruitful discussions, advice and the good times we had together. Since this might be a precedent in the history of particle physics, I must mention how carefully Pat, Guy and Kathy, as well as Abe Seiden and Peter Young from my advising committee read my thesis; their many suggestions and editing comments largely contributed to the production of a readable document.

My stay at Santa Cruz would not have been as interesting without the warm support from the SCIPP staff: Nora Rogers, Georgia Hamel, Merle Pendell and Alec Webster. Thanks to the many friends at Santa Cruz and SLAC, in particular Mary King for her continuous encouragement. Thanks also to all those at UCSC who willingly or not fed exabyte tapes for me remotely. I also want to mention David Stricker for his faithful, entertaining e-mail and continuous friendship over the years. Finally, special thanks to Tony Norcia for cooking wonderful meals on rainy Thursdays.

Lastly but certainly not the least, I want to thank my family in Québec (and all over the world): my parents, my godmother, my brothers (Louis and Hubert) and my sisters (Sylvie and Elise) for their support and interest in my work, even though I did not always manage to properly explain what I was working on. They provided entertainment and encouragement when I most needed it. Their enthusiasm and passion for their own endeavors has always been a source of inspiration. I specially want to thank my mother for her innumerable prayers and my brother Hubert for his genuine interest in my work and for reading this thesis even though he must know I might not reciprocate on his!

It has been a long journey, sometimes frustrating but always exciting, thanks to so many people. It will be hard to leave so many good friends behind but hopefully, our paths will cross again.

* çà coute pas cher et çà fait plaisir à plein de monde...(it doesn't cost anything but it pleases a lot of people...)

September 1961: The beginning of a long journey... little did I know!

1. Theoretical aspects and motivation

1.1 Introduction

Over the past three decades, a very succesful theoretical model - now called the Standard Model- has evolved to describe the most elementary particles and the interactions between them. In this theory, strong interactions are mediated by eight massless gluons and are described by quantum chromodynamics or QCD. Weak interactions proceed through the exchange of two charged massive particles, called $W^{\pm}$, and one massive neutral particle, the Z^0. Electromagnetic processes are described by quantum electrodynamics or QED and are mediated by neutral, massless photons. The weak and electromagnetic interactions are together described by a single unified theory named after the theorists who made the most significant contributions to the development of the theory- Weinberg, Salam, Glashow, Iliopoulos and Maiani. It is often just referred to as the electroweak theory. With the Standard Model, it is possible to predict decay rates and hence lifetimes for particles decaying through the weak or electromagnetic interactions. Such calculations are possible for electroweak interactions but not for the strong interaction due to the relative strength of their coupling constants. The magnitude of the electroweak coupling constants are much smaller than one, but for the strong interaction, the coupling constant α_s is of the order of one. Consequently, when using perturbative theory to perform calculations, we can neglect higher order terms in electroweak interactions which greatly reduces the complexity of the calculations. However, the higher order terms must be included when performing QCD calculations.

Although the Standard model succesfully describes experimental observations, it cannot predict the values of 18 free parameters: the masses of the elementary fermions (six quarks and three leptons, assuming that neutrinos are massless), three coupling constants for the weak, electromagnetic and strong interactions (G_F, α and α_s), the weak mixing angle (θ_W), the mass of the Higgs particle and, finally, three angles and one phase in the Cabibbo-Kobayashi-Maskawa matrix V_{CKM} relating quark weak eigenstates and mass eigenstates:

$$V_{CKM} = \begin{pmatrix} V_{ud} & V_{us} & V_{ub} \\ V_{cd} & V_{cs} & V_{cb} \\ V_{td} & V_{ts} & V_{tb} \end{pmatrix}. \tag{1.1}$$

Much experimental effort has been aimed at measuring these free parameters. In particular, semileptonic decays have been extensively studied to extract some of the CKM matrix elements. Processes involving the charged weak interaction, such as semileptonic decays, contain two vertices at which the virtual W couples to a pair of fermions as shown on Figure 1.1. If the fermions are two quarks, q_i and q_j, the CKM

matrix element V_{ij} is associated with the vertex. If the fermions are leptons, no such factor is needed. Therefore, the weak decay of a hadron to a final state involving leptons are particularly useful for measuring CKM matrix elements. If the final state contains both hadrons and leptons, the decay is referred to as a *semileptonic* decay. As an example, the semileptonic decay $D^+ \to \bar{K}^{*0} l^+ \nu_l$ is shown in Figure 1.1.

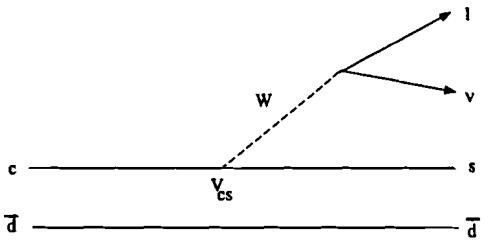

Figure 1.1. Feynman diagram for the semileptonic decay $D^+ \to \bar{K}^{*0} l^+ \nu_l$.

Semileptonic decays are particularly interesting to study due to their simplicity given that the hadronic and leptonic vertices separate; that is, the hadrons and the leptons in the decay are connected by a virtual W but no other particles or mediators of interactions, as can be seen in Figure 1.1. In hadronic decays, on the other hand, the W decays into quarks, and the decay is then complicated by possible gluon exchange between the quarks from the two vertices. In that case, the amplitude for the decay cannot necessarily be factorized. Because of the separation of vertices in semileptonic decays, the decay amplitude can be factorized into a hadronic current and a leptonic current. The leptonic current can be calculated exactly. The hadronic current contains the currently uncalculable form factors which we measure in this analysis.

In this chapter, the form factors in the decay $D^+ \to \bar{K}^{*0} l^+ \nu_l$ are defined. Then, the relationship between these form fators and experimentally measured quantities used to extract the form factors is described. Finally, theoretical predictions of the form factors are discussed and compared to previous experimental measurements.

1.2 Origin of the form factors

From the Feynman diagram shown in Figure 1.1, one can write the matrix element for the decay $D^+ \to \bar{K}^{*0} l^+ \nu_l$ as

$$A(D^+ \to \bar{K}^{*0} l^+ \nu_l) = \frac{G_F}{\sqrt{2}} V_{cs}\, \mathcal{L}^\mu\, \mathcal{H}_\mu \tag{1.2}$$

where G_F is the Fermi coupling constant for the weak interaction and V_{cs} is the CKM matrix element. $\mathcal{L}^\mu$ and $\mathcal{H}_\mu$ represent the leptonic and hadronic currents. The leptonic current follows from the $V-A$ structure of the charged interaction:

$$\mathcal{L}^\mu = \bar{u}_e\, \gamma^\mu\, (1-\gamma_5)\, v_\nu. \tag{1.3}$$

The hadronic matrix element cannot be written down exactly because of the possible exchange of gluons at the hadronic vertex. We therefore write the $\mathcal{H}_\mu$ in a general form

$$\mathcal{H}_\mu = \langle K, \varepsilon |\, J_\mu | P \rangle \tag{1.4}$$

with $J_\mu = (V_\mu - A_\mu)$. P and K are the respective 4-momenta for the D and K^*, and ε, the polarization vector for the K^*. These are the only 4-vectors available for this process. Since the amplitude must be a Lorentz invariant after contracting the hadronic current with the leptonic current, it can be shown that for a vector meson in the final state, the only possible vector and axial-vector terms linear in ε and containing the available 4-vectors are:

$$\begin{aligned}\langle K, \varepsilon |\, J_\mu \,| P \rangle = (M_D + M_{K^*})\, A_1(q^2) \varepsilon^*_\mu - \frac{A_2(q^2)}{M_D + M_{K^*}}\, (\varepsilon^* \cdot P)(P+K)_\mu \\ - \frac{A_3(q^2)}{M_D + M_{K^*}} (\varepsilon^* \cdot P)(P-K)_\mu - i \frac{2\, V(q^2)}{M_D + M_{K^*}} \epsilon_{\mu\nu\rho\sigma} \varepsilon^{*\nu} P^\rho K^\sigma.\end{aligned} \tag{1.5}$$

Here q^2 is the invariant mass of the virtual W. $V(q^2)$, $A_1(q^2)$, $A_2(q^2)$, and $A_3(q^2)$ are the form factors, functions which depend on q^2 and which parametrize the hadronic matrix element. In the zero lepton mass limit, the term containing A_3 goes to zero when contracted with the leptonic matrix element. We are then left with three independent form factors to describe the effects of the strong interactions when a pseudoscalar meson decays semileptonicly into a vector meson. We cannot calculate the form factors explicitly but various models attempt to estimate them. In addition, the heavy quark effective theory relates the independent form factors at particular kinematic points. In this analysis, we extract the form factors from experimental data.

1.3 q^2-dependence of the form factors (nearest pole dominance)

The form factors introduced above can be a function of q^2, the invariant mass of the virtual W. The exact form of this function is not known. A dipole shape is assumed by many theoretical models [1, 2, 3, 4] since one believes that the c quark is most likely to decay into an s quark near a $c\bar{s}$ resonance as depicted in Figure 1.2. Since the W carries spin 1 but no definite parity (it mediates the V-A interaction), the $q\bar{q}$ resonance should also carry spin 1 to conserve spin. The vector part of the hadronic current will have negative parity whereas the axial part will carry positive parity. We expect a pole for the axial part near the mass of the lowest lying $J^P = 1^+$

state, that is, at the mass of the D_{S1}^* at 2.5 GeV/c^2, and for the vector part, near the 1^- state, the D_S^* at 2.1 GeV/c^2. The assumed form of the q^2-dependence for a form factor F is expressed as

$$F(q^2) = \frac{F(0)}{1 - q^2/m_{pole}^2}$$

where m_{pole} is the mass of the appropiate pole described above. This is still just an assumption and can be tested by a high-statistics experiment such as E791 when the full data sample becomes available.

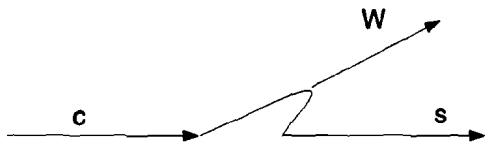

Figure 1.2. A simple illustration of the nearest-pole-dominance model. The W line is stretched to look like a vacuum fluctuation into a $q\bar{q}$ pair. The W is assumed to be produced preferentially near the mass of the lowest lying $c\bar{s}$ resonance with appropriate value of J^P to conserve spin and parity.

1.4 The measurable parameters for the differential decay rate

We can look at the decay $D^+ \to \bar{K}^{*0} l^+ \nu_l$ as a succession of 2-body decays where the initial D^+ first decays into K^* and a virtual W. Since the D^+ is a spinless particle, it decays isotropically. Therefore, the only free parameters at this point are the invariant mass of the virtual W (q^2), and the invariant masss of the K^* ($M_{K\pi}$). Next the $K^* \to K^- \pi^+$ and $W^+ \to l^+\nu_l$. Since both decaying particles carry spin, their decay will not necessarily be isotropic and we can measure the relative angles between their decay products. We define θ_l to be the angle between the lepton and the direction opposite to the recoiling D^+ in the W rest frame, and θ_V the angle between the kaon and the direction opposite to the recoiling D^+ in the K^* rest frame. The last angular variable χ is defined as the angle between the decay planes for the K^* and W. The three angles are shown in Figure 1.3. The five kinematic variables $\cos\theta_l$, $\cos\theta_V$, χ, q^2 and $M_{K\pi}$ are all independent and together completely describe the decay.

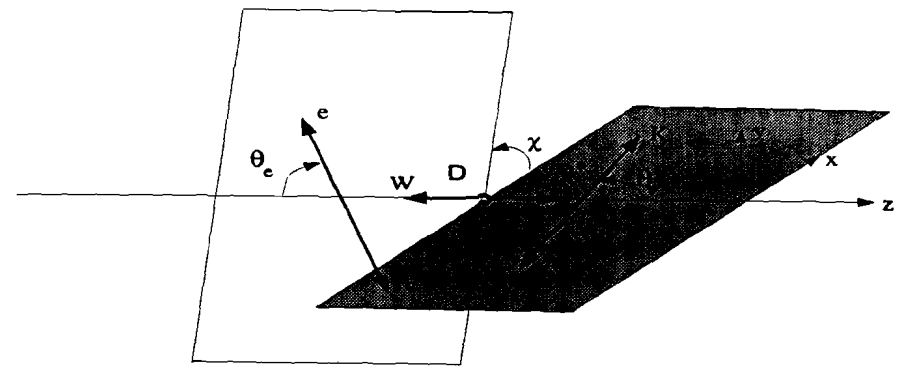

Figure 1.3. The three characteristic decay angles θ_l, θ_V, and χ for $D^+ \to \bar{K}^{*0} l^+ \nu_l$.

1.5 Differential decay rate using helicity formalism

The differential decay rate is given by the formula

$$d\Gamma = \frac{(2\pi)^4}{2M_D} \mid \mathcal{M} \mid^2 d\Phi_4(D; K, \pi, l, \nu) \tag{1.6}$$

where $d\Phi_4(D; K, \pi, l, \nu)$ is the four-body phase space element. The matrix element $\mathcal{M}$ can be obtained from the expressions for the leptonic and hadronic current described in the previous section. Alternatively, the decay $D^+ \to \bar{K}^{*0} l^+ \nu_l$ can be broken into a series of two-body decays, $D^+ \to \bar{K}^{*0} W^+$ followed by $W^+ \to l^+\nu_l$ and $K^{*0} \to K^-\pi^+$, and treated in the helicity formalism. The matrix element can then be expressed as

$$\begin{aligned} \mathcal{M}_i = \sum_{\varepsilon,\lambda} \mathcal{M}_i(D^+ \to \bar{K}^{*0}_\varepsilon W^+_\lambda) \times \\ \mathcal{M}_\varepsilon(\bar{K}^{*0} \to K^-\pi^+)\, \mathcal{P}_\varepsilon(\bar{K}^{*0}) \mathcal{M}_\lambda(W^+ \to l^+\nu_l)\, \mathcal{P}_\lambda(W^+). \end{aligned} \tag{1.7}$$

where $\mathcal{P}_\varepsilon = [M_{K^*}^2 - M_{K\pi}^2 - iM_{K^*}\Gamma(M_{K\pi})]^{-1}$ is the K^* propagator, $\mathcal{P}_\lambda(W^+) = G_F$ is the W propagator. The sum is taken over the helicities ε and λ of the K^{*0} and W, respectively, with ε and λ taking on the values $\{-1, 0, +1\}$. The matrix element for $D^+ \to K^*\, W^+$ can be written in terms of the helicity states of the K^* and the W. Each state will be multiplied by a helicity amplitude denoted by H_i that will depend on the form factors. That is,

$$\mathcal{M}_i(D^+ \to \bar{K}^{*0}_\varepsilon W^+_\lambda) = C(q^2) H_i. \tag{1.8}$$

The relative angle between the planes of the decay products of the K^* and W^+, χ,

will relate the two coordinate systems. Using the Wigner D-function, one can write the matrix element for $W \rightarrow l\nu$ appearing in eq. (1.7) in terms of the helicity states of the W^+:

$$\mathcal{M}_\lambda(W^+ \rightarrow l^+\nu_l) \propto \begin{cases} 1+\cos\theta_l, & \lambda = +1 \\ 1-\cos\theta_l, & \lambda = -1 \\ -\sqrt{2}\sin\theta_l, & \lambda = 0 \end{cases} \tag{1.9}$$

The angle θ_l is defined in Figure 1.3. Similarly, the matrix element for the decay $K^* \rightarrow K\pi$ can be written as

$$\mathcal{M}_\varepsilon(\bar{K}^{*0} \rightarrow K^-\pi^+) \propto \begin{cases} \pm\sin\theta_V, & \varepsilon = \pm 1 \\ \sqrt{2}\cos\theta_V, & \varepsilon = 0. \end{cases} \tag{1.10}$$

Substituting eq. (1.7)-(1.10) into eq. (1.6) and evaluating the phase space factors, we can write the differential decay rate in terms of the five kinematic variables available for this process:

$$\begin{aligned} \frac{d\Gamma}{dM^2_{K\pi}\, dq^2\, d\cos\theta_V\, d\cos\theta_l\, d\chi} &= G_F^2 |\, V_{cs}\,|^2 \frac{3}{2(4\pi)^5} \frac{M_{K^*}}{M_D^2\, M_{K\pi}}\, Kq^2 \\ &\times \frac{M_{K^*}\Gamma(M_{K\pi})}{(M^2_{K\pi} - M^2_{K^*})^2 + M^2_{K^*}\,\Gamma^2(M_{K\pi})} \\ \times \{\, [\,(1+\cos\theta_l)^2 \mid H_+(q^2)\mid^2 &+ (1-\cos\theta_l)^2 \mid H_-(q^2)\mid^2]\ \sin^2\theta_V \\ &+4\sin^2\theta_l\ \cos^2\theta_V \mid H_0(q^2)\mid^2 \\ &-2\sin^2\theta_l\ \sin^2\theta_V\ Re\,(e^{i2\chi}\, H_+^* H_-) \\ &-4\sin\theta_l\,(1+\cos\theta_l)\ \sin\theta_V\ \cos\theta_V\ Re\,(e^{i\chi} H_+^* H_0) \\ &+4\sin\theta_l\,(1-\cos\theta_l)\ \sin\theta_V\ \cos\theta_V\ Re\,(e^{i\chi} H_-^* H_0)\ \} \end{aligned} \tag{1.11}$$

where $M_{K\pi}$ = invariant mass of the K-π system,

M_{K^*} = central mass of the $\bar{K}^{*0}$,

V_{cs} = CKM matrix element, and

K = K^* momentum in the D^+ rest frame.

In the above expression, the form factors are contained in the helicity amplitudes [2]:

$$H_\pm(q^2) = (M_D + M_{K\pi})\ A_1(q^2) \mp 2\frac{M_D\, K}{M_D + M_{K\pi}}\, V(q^2) \tag{1.12}$$

and

$$H_0(q^2) = \frac{1}{2qM_{K\pi}}\left[(M_D^2 - M^2_{K\pi} - q^2)(M_D + M_{K\pi})\ A_1(q^2) - 4\frac{M_D^2\, K^2}{M_D + M_{K\pi}} A_2(q^2)\ \right].$$

The first two amplitudes $H_\pm$ correspond to the transverse modes of the K^* and the last one refers to the longitudinal polarization mode. Since $A_1(q^2)$ is common to all helicity amplitudes $H_\pm$ and H_0, it is customary to measure the ratios $R_2 = A_2(0)/A_1(0)$ and $R_V = V(0)/A_1(0)$. Notice that in eq. (1.11), $\mid H_0 \mid^2$ dominates when $\cos\theta_V \rightarrow \pm 1$ (and q^2 is small) but $\mid H_\pm \mid^2$ dominates everywhere else. Also, H_+ and H_- are enhanced in regions with opposite signs of $\cos\theta_l$. These facts make it possible to separate the contributions of the different helicity amplitudes in the 5-dimensional space formed by θ_l, θ_V, χ, $M_{K\pi}$ and q^2. No form factor information is contained in the distribution of $M_{K\pi}$. However, it will enable us later on to discriminate against background events when performing a multidimensionnal fit to the data.

We can also define the ratio of the transverse to longitudinal decay rates as

$$\Gamma_L/\Gamma_T = \frac{\int Kq^2 |\, H_0(q^2)\,|^2\, dq^2}{\int Kq^2 [|\, H_+(q^2)\,|^2 + |\, H_-(q^2)\,|^2] dq^2} \tag{1.13}$$

where again K is the K^* momentum in the D rest frame.

1.6 Heavy quark effective theory

Much interest has been renewed in the past few years in accurate measurements of form factors in semileptonic decays since Mark Wise and Nathan Isgur [5] postulated a new theoretical framework relating all form factors to a universal function. This new theory, called the heavy quark effective theory or HQET, establishes the existence of an $SU(3)$ flavor symmetry and an $SU(2)$ spin symmetry in the limit that all heavy quarks have infinite mass. "Heavy" here means that the quark masses are large compared to the QCD parameter, Λ_{QCD}. The QCD parameter is of the order of 200-400 MeV, making the c, b and t quarks relatively "heavy".

1.6.1 The flavor symmetry [6]

The flavor symmetry of the HQET stipulates that transitions between different heavy quarks can be related if they involve the same four-velocity transfer. The theory then predicts that $R_2 = R_V = 1$ in the limit of infinite quark masses. In addition, the HQET relates the form factors for decays of heavy quarks into light quarks to a universal form factor ξ called the Isgur-Wise universal function. This has an important application in the semileptonic decay of B and D mesons to light hadronic systems such as π or ρ. Measurements of the $c \rightarrow d$ matrix elements in semileptonic D decay can provide information on the $b \rightarrow u$ matrix elements crucial to the determination of V_{ub}.

Semileptonic D decays with a kaon in the final state such as $D^+ \rightarrow \bar{K}^{*0} l^+ \nu_l$ *cannot* be related to semileptonic B decays with a kaon in the final state since $b \rightarrow s$ transitions are not allowed at tree level. However, $b \rightarrow s$ transitions can occur via rare

processes such as Penguin diagrams and are sensitive to the existence of particles like the charged Higgs bosons. The heavy quark flavor symmetry can be used to relate the form factors in $D \rightarrow K^*$ transitions to those in $B \rightarrow K^*$ transitions [7]. Therefore, experimental data on the semileptonic decay $D^+ \rightarrow \bar{K}^{*0} l^+ \nu_l$ provide information on matrix elements relevant for the rare B-meson decays $B \rightarrow K^* e^+ e^-$ and $B \rightarrow K^* \gamma$. The recent observation of the decay $B \rightarrow K^* \gamma$ by the CLEO collaboration, the first direct observation of a decay occurring via a Penguin diagram [8], revives the interest for a more precise measurement of the form factors in the decay $D^+ \rightarrow \bar{K}^{*0} l^+ \nu_l$.

1.6.2 The spin symmetry [6]

The spin symmetry leads to the prediction of degenerate mass states for hadrons containing a heavy quark. In the infinite mass limit, the mass of the hadron containing a heavy quark is independent of the spin state of the heavy quark. This situation is very much analogous to the hyperfine splitting of the hydrogen atom. Because of the large proton mass, the corrections to the mass of the bound state, due to the coupling of the proton spin with the electron spin and with the orbital angular momentum, are much smaller than the mass of the bound state.

A consequence of the spin-symmetry relevant to semileptonic decays is that pseudoscalar-to-vector transitions can be related to the pseudoscalar-to-pseudoscalar transitions. Therefore, the form factors for $D^+ \rightarrow \bar{K}^{*0} l^+ \nu_l$ can be written in terms of the same universal function Ξ and related to the single form factor for $D^0 \rightarrow K^- l^+ \nu_l$.

1.7 Theoretical models

Since QCD does not provide exact calculations for the form factors, we are forced to use theoretical models to make predictions for the form factors. These models can be categorized as follow [9]:

- Phenomenological form factor models.
- Lattice gauge theory calculations.
- QCD sum rules.

The phenomenological form factor models assume different forms for the q^2-dependence of the form factors and can be relativistic or non-relativistic models. The form factors are assumed to be described by

$$f_i(q^2) = f_i(q^2_\alpha)\ \phi(q^2_\alpha, q^2) \tag{1.14}$$

where $f_i(q^2_\alpha)$ is the value of the form factor at a particular value of q^2 and $\phi(q^2_\alpha, q^2)$ is an evolution function describing the assumed q^2 dependence of the form factors. Some of these models are described below:

- The ISGW model [1] is a non-relativistic model which describes the form factors at $q^2_\alpha = q^2_{max} = M^2_D - M^2_{K^*}$. The q^2-dependence is represented by an exponential function

$$\phi\,(q^2) \approx exp\left(\frac{q^2 - q^2_{max}}{constant}\right).$$

- The GS/AW model [2]assumes a single pole form for the q^2-dependence of the form factors as used in this analysis and described in section 1.3 .
- The WSB [3] model is a relativistic model which calculates the form factors at $q^2_\alpha = 0$. The model assumes a single-pole function to describe the q^2-dependence

$$\phi\,(q^2) = \frac{1}{1 - q^2/M^2_{pole}}$$

as described in section 1.3 .

- The KS model [4] is very similar to the WSB model but parametrizes some of the form factors according to a dipole function

$$\phi(q^2) = \left(\frac{1}{1 - q^2/M_{pole}}\right)^2 .$$

The predictions of these models are shown in Table 1.1 along with all experimental measurements of the form factors for the decay $D^+ \rightarrow \bar{K}^{*0} l^+ \nu_l$.

From this table, one realizes that the measurements of R_V, from E687, E653 and E691, all agree with each other within errors but the measured values are substantially higher than values calculated using phenomenological models. The other theoretical models based on lattice calculations or QCD sum rules predict closer values to the experimental measurements but these calculations carry large uncertainties. However, E691 measurement for R_2 is barely compatible with the value measured by E653 and E687. The three experimental results for R_2 only agree at the 1.5 σ level. While E691 measured R_2 near zero, the two other experiments obtained a value closer to 1 which is more consistent with all theoretical models. Until the publication of the E687 result in early 1993, this discrepancy had sparked a lot of interest, since most theoretical models could not be reconciled with the E691 measurement. This analysis provides one more precise measurement which should bring more light to this issue.

Table 1.1 Experimental measurements and theoretical predictions for R_2, and R_V [9]

Group	R_2	R_V	Γ_L/Γ_T	# of events used for measurement
experimental measurements [10, 11,12,13,14]				
E687	$0.78 \pm 0.18 \pm 0.10$	$1.74 \pm 0.27 \pm 0.28$	$1.20 \pm 0.13 \pm 0.13$	875
E653	$0.82^{+0.22}_{-0.23} \pm 0.11$	$2.00^{+0.34}_{-0.32} \pm 0.16$	$1.18 \pm 0.18 \pm 0.08$	305
E691	$0.0 \pm 0.5 \pm 0.2$	$2.0 \pm 0.6 \pm 0.3$	$1.8^{+0.6}_{-0.4} \pm 0.3$	204
MARK III			$0.5^{+1.0+0.1}_{-0.1-0.2}$	14
WA82			$0.6 \pm 0.3^{+0.3}_{-0.1}$	50
theoretical calculations				
phenomenological models [1,2, 3,4]				
ISGW	1.0 ± 0.3	1.4 ± 0.4	0.9	
GS/AW	0.8	1.9	1.2	
WSB	1.3	1.4	1.1	
KS	1.0	1.0	1.2	
lattice gauge calculations [15,16]				
BBD	1.2 ± 0.2	2.2 ± 0.2	0.86 ± 0.06	
AOS	0.9 ± 0.7	1.9 ± 0.8		
QCD sum rules [17,18]				
BKS	$0.70 \pm 0.16^{+0.20}_{-0.15}$	$1.99 \pm 0.22^{+0.31}_{-0.35}$		
LMS	0.01 ± 0.7	1.6 ± 0.3	1.7 ± 0.6	

2. The Tagged Photon Spectrometer

2.1 Introduction

Experiment E791, a fixed target experiment conducted at Fermilab from July 1991 to January 1992, used an upgrade of the Tagged Photon Spectrometer, a detector first commissioned in 1979 for E516. The E516 experiment was the first of a series of charm experiments to be done using different upgrades of the detector located in what is now known as the Tagged Photon Lab or TPL. The initial spectrometer, designed for photoproduction of charm, had no vertex reconstruction capabilities, which limited the number of charmed events reconstructed by E516. This experiment was followed by E691, a very successful charm photoproduction experiment. Using ten planes of silicon microstrip detectors, the E691 collaboration could adequately separate primary and secondary vertices, identifying the points of formation and decay of a particle containing a heavy quark. This feature enabled E691 to fully reconstruct about 10,000 charmed events. E769 followed E691, using π^+, π^-, K^+, K^-, and protons beams, as well as more silicon planes, to study hadroproduction of charm.

The whole detector as used by the E791 collaboration is shown in Figure 2.1. Charged particles are detected with 23 planes of silicon microstrip detectors, ten proportional wire chambers (PWC), and four drift chamber modules containing a total of 35 planes. Two dipole magnets provided the magnetic field necessary for momentum measurement. There were two threshold Čerenkov counters used to distinguish between electrons, pions, kaons, and protons, followed by electromagnetic and hadronic calorimeters. Finally, a series of scintillation counters used for muon detection completed the spectrometer.

2.2 The beam line and the target

For these fixed target experiments, one had to extract the 800-GeV protons from the main ring of the Tevatron and inject them into one of the three beamlines heading for the experimental area. The extraction process, called a spill, lasted 22 seconds and was repeated every minute. Between spills, the Tevatron was filled again with protons. During each spill, about 10^{13} protons were sent to the experiments, of which two teraprotons were allocated to E791.

Right after extraction, the proton beam was split electrostatically and sent to three experimental areas called the Meson, Neutrino, and Proton areas. The beam for the proton area was split once more between the P-East line where the TPL is located, P-West, P-Center and Broad-Band lines. The different beamlines as well as the Tevatron itself are shown in Figure 2.2.

Upstream from the spectrometer, the proton beam hit a 30 cm-long beryllium target after which pions were momentum-selected and steered onto the E791 target.

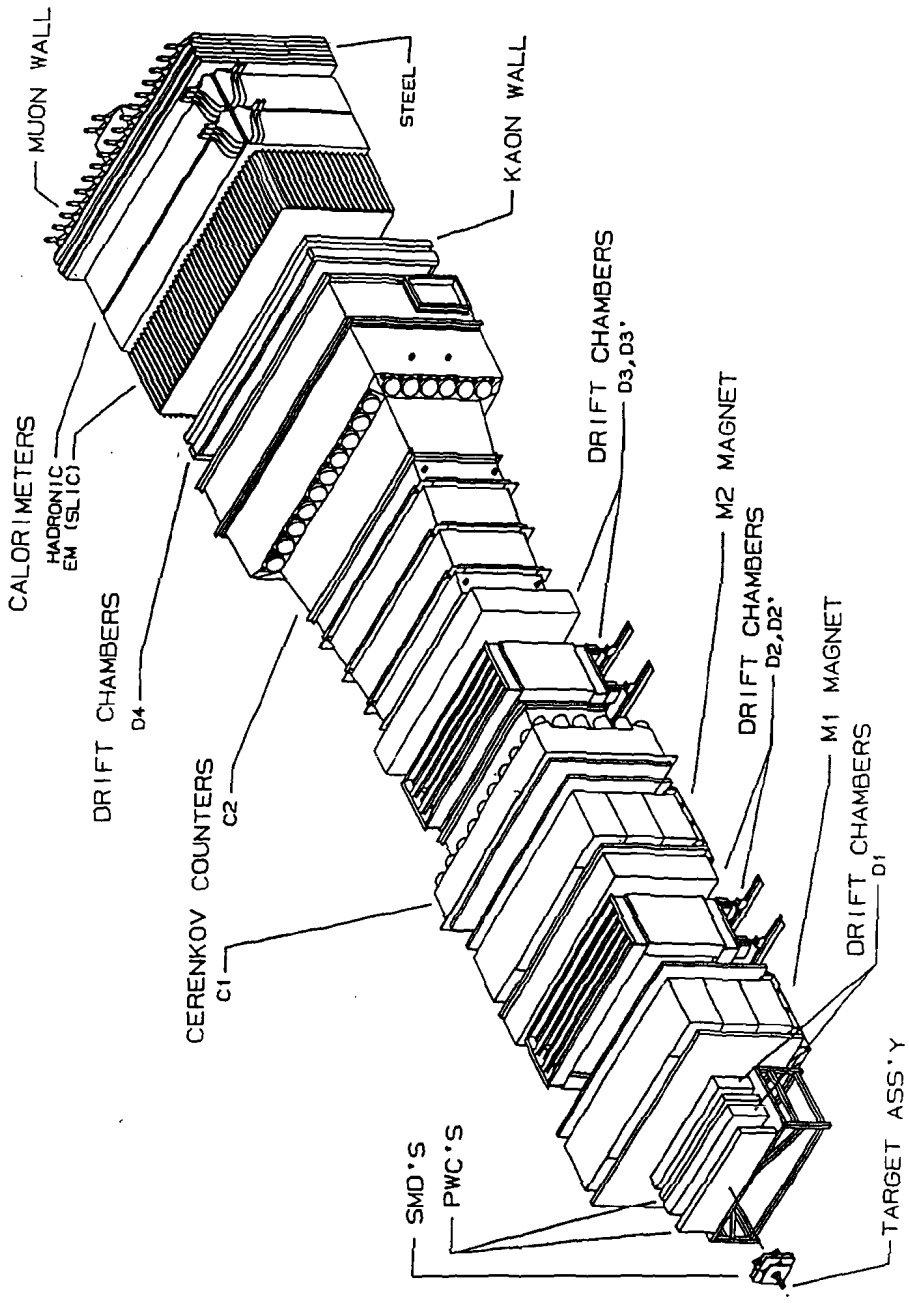

Figure 2.1. The Tagged Photon Spectrometer in the configuration used by E791.

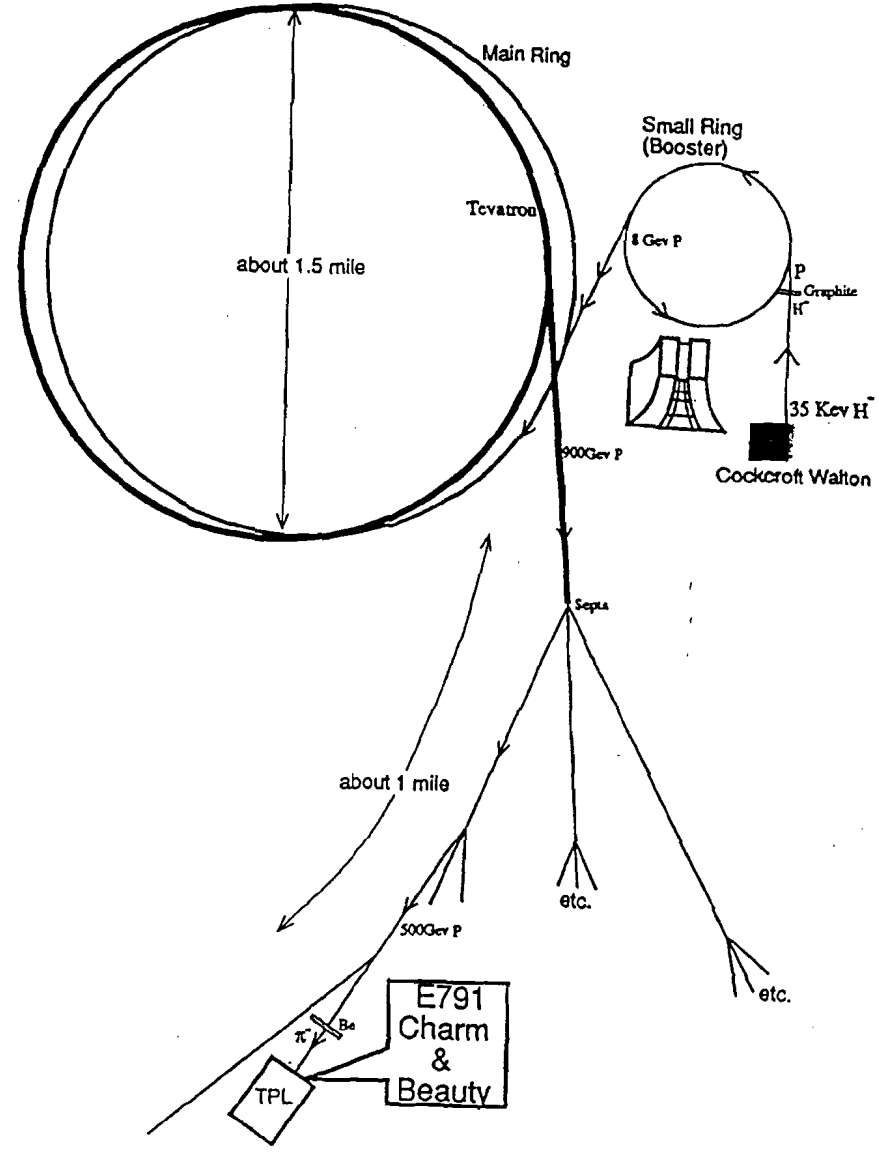

Figure 2.2. A view of the Tevatron and the different beamlines serving the fixed target experiments.

The typical pion yield from the primary target was 42 million secondary pions per spill. Final focussing and alignment of the pion beam just before the target was done using two quadrupole and two dipole magnets. These last magnets were adjusted from the control room at TPL by the shift crew to optimize the interaction rate.

2.2.1 The target

One crucial issue for a successful charm experiment is the ability to clearly reconstruct and separate the primary vertex, where charm quarks are produced, and the secondary vertex, at which they decay. Therefore, the target design involved conflicting needs of maximizing the target thickness (to increase the interaction rate) while minimizing the overall chances for multiple scattering and secondary interactions, which degrade the vertex resolution and increase the background. It is advantageous if the charmed particle decays outside the target to facilitate identification of the secondary vertex. Consequently, the target foils should be thin and arranged such that typically, the charmed particle decays downstream from the target. Taking all of the above into account, the collaboration finally settled on a five-foil configuration with a total target thickness corresponding to 2.2% of an interaction length. The target consisted of one platinum and four carbon foils, each accounting for about 0.4% of an interaction length. Platinum was selected for its high Z, therefore allowing for the same interaction length for the a thinner foil. Each carbon foil was 1.45 mm-thick while the platinum foil was only 0.5 mm-thick. Only the upstream target is made of platinum because the high Z also results in a short radiation length which would lead to significant scattering of charged particles. The platinum foil was made from a polished Australian mint coin, the only known source of platinum disk with the required dimensions. Along the same salvaging line, the carbon foils were milled from industrial diamond drill bits. The final configuration with the exact position of each foil is shown in Table 2.1.

The target separation was chosen so that a charmed particle produced in one foil typically decayed before the next downstream foil. The mean decay length l for a particle with mean lifetime τ is given by

$$l = \gamma\beta c\tau, \tag{2.1}$$

where $\gamma = E/m$. For a D-meson produced with about 200 GeV/c of momentum, $\gamma \sim 100$, and $\beta \sim 1$. For typical lifetimes of (4-10)$\times 10^{-13}$ s, Eq. (2.1) reduces to $l \sim 1$ cm. The foils were spaced roughly 1.5 cm apart, which ensures that the secondary vertex is usually located outside a foil.

Table 2.1 The five-foil target layout.

foil number	1	2	3	4	5
z-position (cm)	-8.191	-6.690	-5.154	-3.594	-2.060
material	Pt	C	C	C	C
spacing (cm)		1.501	1.536	1.560	1.534
thickness (mm)	0.52	1.57	1.57	1.53	1.58
interaction length	0.588 %	0.412 %	0.412 %	0.402 %	0.415 %

2.3 Charged particle tracking

2.3.1 The Silicon Microstrip Detector

E516 was the first experiment to look for charm at the Tagged Photon Lab but, as mentioned before, did not have a vertex detector. Since the main method for distinguishing charmed events from the enormous light-quark background is the presence of two well-separated vertices (the production and decay points of a charm quark), E516 was unable to efficiently distinguish the signal from the background. Silicon microstrip detectors (SMD's) can provide accurate vertex information due to their fine segmentation and were incorporated into the Tagged Photon Spectrometer by the E691 collaboration in 1984. Using the vertex separation capabilities of the SMD's, E691 and E769 reconstructed about 10,000 D mesons each, out of data samples of 100 and 400 million events, respectively.

The SMD's operate as follows. When a charged particle crosses a layer of semiconductor, [19] it deposits ionization energy. This creates an electron-hole pair in the semiconductor which is separated by applying a bias voltage. Narrow aluminium strips deposited on top of a semiconducting silicon wafer provide a conducting path for the freed charged particles. By connecting electrodes to each individual strip, a small electrical pulse can be collected and amplified, giving the location of the incident particle. A series of silicon planes with strips with a pitch of a few tens of microns provides an accurate tracking device suitable for resolving separated vertices due to charm decay.

Former experiments at TPL, E691 and E769, used 9 and 13 planes of SMD's, respectively, all downstream from the target. The E791 SMD system consisted of 23 silicon planes, six upstream of the target for accurate beam position determination, and 17 downstream for early tracking. Figure 2.3 shows the layout of the different planes. Parts of the system were new and parts were inherited from the previous experiments but E791 was the first experiment at TPL to use upstream silicon planes.

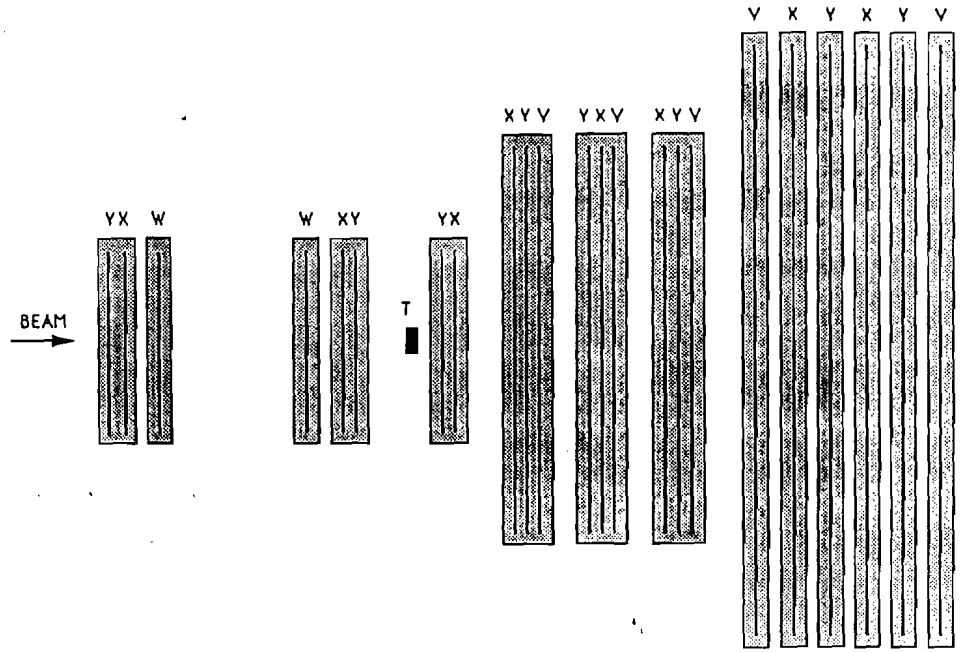

Figure 2.3. The layout of the 23 SMD planes.

Each SMD plane was only 300 μm thick to minimize multiple scattering. The overall geometrical acceptance was about $\pm$150 mrad around the beam axis. The SMD planes differed both in geometry and details of the first stage readout electronics but all shared some basic features. None of the strips were used to measure the energy deposited but simply to determine if the strip had been hit or not by comparing the voltage pulse to a set threshold. Each strip was connected to a preamplification system which was located near the detector. The preamplified signals were then sent to the digitizer, a Programmable-Array-Logic-based circuit. All the planes were fabricated by Micron Semiconductors of England. The main characteristics of the SMD planes are summarized in Table 2.2.

Table 2.2 Main characteristics of the 23 SMD planes. The last six planes had a smaller strip pitch for the central strips than for the outer strips. A negative z value indicates the plane was upstream from the target.

plane	z-position (cm)	strip spacing (μm)	dimensions (cm)	view	efficiency
1	-80.250	25	5×5	Y	80%-98%
2	-79.919	25	5×5	X	80%-98%
3	-74.529	25	5×5	W	80%-98%
4	-33.163	25	5×5	W	80%-98%
5	-30.133	25	5×5	X	80%-98%
6	-29.483	25	5×5	Y	80%-98%
7	0.670	25	5×5	Y	80%-98%
8	1.000	25	5×5	X	80%-98%
9	1.931	50	10×10	X	88%-95%
10	3.015	50	10×10	Y	88%-95%
11	6.684	50	10×10	V	88%-95%
12	11.046	50	10×10	Y	88%-95%
13	11.342	50	10×10	X	88%-95%
14	14.956	50	10×10	V	88%-95%
15	19.915	50	10×10	X	88%-95%
16	20.254	50	10×10	Y	88%-95%
17	23.878	50	10×10	V	88%-95%
18	27.558	50;200	10×10	V	92%-97%
19	31.848	50;200	10×10	X	92%-97%
20	34.548	50;200	10×10	Y	92%-97%
21	37.248	50;200	10×10	X	92%-97%
22	39.948	50;200	10×10	Y	92%-97%
23	45.508	50;200	10×10	V	92%-97%

With over 16500 strips, electronic noise was a major issue. False hits mean increased difficulties in pattern recognition resulting in ghost tracks as well as creating a larger event size. Therefore the temperature around the SMD planes had to be maintained around 60°F to avoid thermal excitation that could simulate a genuine hit. Any substantial temperature increase translated to higher background noise, leading the electronics to register false hits. The average number of hits per plane was still remarkably low, averaging about two hits per plane per beam particle for the planes upstream from the target, corresponding to a noise level of about 0.1% per strip. The typical number of hits per plane (including real hits) was about two for planes upstream from the target, and on the average exceeded ten for planes downstream from the target. The residuals for the SMD planes, that is, the difference between the expected hit position (from track interpolation) and the detected hit position, were used to determine the SMD resolution. Typical resolutions for the different SMD planes were found to be 7.2 μm and 14.4 μm for the 25 and 50 μm pitch planes, respectively.

2.3.2 The Proportional Wire Chambers

For beam tracking and help in finding the primary vertex, E769 installed proportional wire chambers (PWC's) just upstream of the target. E791 added two more PWC planes downstream from the target to increase tracking capabilities. PWC's operate as follows: when a charged particle crosses a gas, it ionizes molecules, leaving a trail of free electrons and ions. Applying a high, positive voltage to a series of evenly spaced wires between planes at ground forces these electrons to migrate towards the nearest wire. As the electrons are accelerated in the high field region around the anode, they ionize more atoms, creating a larger number of free electrons, a phenomenon known as an avalanche process. This excess of free electrons and ions creates an electrical pulse on the anode wire, registering the position of the initial charged particle. With PWC's, we record which specific wire detected an electrical pulse produced by a charged particle, but not the drift time to that particular wire. Therefore, the spatial resolution, and hence the precision they can provide for beam localization or charged particle tracking, is entirely determined by their pitch. The resolution is given by the wire spacing divided by $\sqrt{12}$.

In the E791 PWC system, the charged particles passed through a gas mixture of 82.7% Argon, 17% CO_2, and 0.3% Freon. Each plane contained 64 sense wires spaced 1 mm apart. Each station of PWC's was made of several planes arranged in different views: X, X', Y, and W. The X view and Y view wires were strung vertically and horizontally, respectively. The W view axis was rotated by -60^0 with respect to the vertical. The X' view was offset by half a cell from the X view in an attempt to improve the resolution. All PWC parameters are given in Table 2.3.

Table 2.3 PWC characteristics for all planes upstream and downstream from the target.

	upstream	downstream
number of planes	8	2
dimensions (cm)	6.4×3.2	53.0×28.8
view ordering	X, X', Y, W	X, Y
wire spacing (mm)	1.0	2.0
resolution (μm)	145 (X, X'); 289(Y, W)	577
z-position (first) (cm)	-3117.0	118.5
z-position (last) (cm)	-1212.0	161.1
applied voltage (V)	2750	3750

The charge from the electrical pulse was amplified and discriminated by a module called the Proportional Charge Operational System (PCOS). With such a small wire spacing, electron drift time to the wire was nearly negligible; the current peak was sensed at the amplifier typically about 15 ns after the ionizing particle passed through the chamber. The total charge collection process and discrimination time was about 4 μs which was too long for triggering purposes and therefore was not used in the trigger process to determine the number of incident particles in the beam.

2.3.3 The drift chambers

As part of the charged particle tracking system, in addition to the SMD's and PWC's, the Tagged Photon Spectrometer was equipped with four sets of planar drift chambers. Just like the PWC's, their operation is based on the fact that when a charged particle passes through a gas, it leaves a trail of ionized atoms behind. The free electrons are collected on wires maintained at a high positive potential with respect to other cathode wires. Being positively charged, the ions will drift toward the cathode. The electron drift velocity depends on the nature of the gas being used. The drift time for the electrons provides an accurate measurement of the position of the charged track from the wire, assuming that the electrons are drifting within a uniform electric field, which is shaped by the field wires.

The detector had four separate drift chamber modules containing a total of 35 planes measuring four different views, namely X, X', U, and V. Each plane consists of sense wires (to collect the charge freed by ionization) and field wires, whose role was to provide a uniform electric field through the drift region. The X and X' views

were made of vertically strung wires with the X' view shifted by half a cell relative to the X planes. The U and V views had their wires at ±20.5° from the vertical. The complete layout of the 35 drift chamber planes is given in Table 2.4. The first chamber D1 was located upstream of the first analysis magnet M1 and, along with the SMD's and PWC's, provided an initial measurement of the track trajectory. D2 was positioned between the two bend magnets. The third drift chamber D3 was located just after the second bend magnet M2 and added tracking information for particles with momentum high enough to make it through both magnets. The last chamber D4 came much further downstream, past the Čerenkov counters, just before the calorimeters. Despite its long lever arm, this chamber was less useful due to higher noise level and poorer resolution caused by its intrinsic design, with its basic X cell being twice as large as for D3. Typical resolutions and efficiencies per chamber are shown in Table 2.4.

Table 2.4 Drift chamber characteristics [20].

	D1	D2	D3	D4
dimensions (cm)	160 × 120	230 × 200	330× 200	550× 300
view ordering	X, X', U, V	X, U, V	X, U, V	X, U, V
number of planes	8	12	12	3
number of channels	1536	2400	1952	416
U and V cell size (cm)	0.476	.892	1.487	2.97
X cell size (cm)	0.446	0.953	1.588	3.18
z-position first plane (cm)	142.204	380.959	927.366	1736.476
z-position last plane (cm)	183.364	500.326	1046.175	1747.745
resolution (μm)	275	250	250	350
efficiency	95%	95%	95%	90%

The drift chamber planes were grouped into assemblies with a complete set of three planes allowing the determination of the x and y position of a particle at a particular location in z. Each view by itself cannot be used to determine the exact location of a hit (even in one dimension) due to left-right and double-hit ambiguities. The former arises from the fact that one cannot tell from which direction the electrons drifted to the wire. The latter happens when more than one wire in a particular view has a signal. Complete reconstruction of the x and y position requires information from three different views.

In upgrading from E769 to E791, the readout speed of the drift chamber electronics had to be increased to match the requirements of a faster data acquisition system. The small pulse collected by the sense wires first passed through a discriminator before reaching the Time-to-Digital Converters (TDC's), which were themselves controlled by 11 Fast Smart Crate Controllers (FSCC's). These programmable units could store in memory and automatically subtract the value of the electronic time offset for each wire. These were regularly measured by sending a computer-generated pulse to each drift chamber channel and recording the arrival time at the TDC's. The drift time was measured backward from a common stop for all channels. The drift time was also corrected for the z-position of the planes. At regular intervals, magnet-off muon runs were used for accurate determination of various drift chamber alignment constants such as their x, y and z-positions.

2.3.4 The analysis magnets

The Tagged Photon Spectrometer was equipped with two large-aperture copper coil magnets. They provided transverse momentum kicks of 212 MeV/c and 320 MeV/c. All the magnet parameters are listed in Table 2.5. An exact mapping of the magnetic field was conducted to allow for the best possible tracking. Every few hours during the experiment, the current on these magnets was adjusted such as to maintain it within 0.1% of its nominal value.

Table 2.5 Magnet parameters.

	M1	M2
z-position front (cm)	222.5	566.9
z-position center (cm)	263.5	617.7
z-position back (cm)	324.1	668.5
aperture (cm^2)	183.2 × 81	182.9 × 85.6
length (cm)	101.6	101.6
current (amp)	2500	1800
$\int B_y(0,0,z)dz$ (Gauss-cm)	711,097	1,077,242
p_T kick (MeV/c)	212	320

Given an accurate value for the magnetic field, one can track charged particles in the detector and determine their momentum. A particle with unit charge and velocity

v passing through a magnetic field **B** experiences a force **F** given by

$$\mathbf{F} = \frac{d\mathbf{p}}{dt} = \pm \mathbf{v} \times \mathbf{B}. \tag{2.2}$$

Since $\mathbf{v} = d\mathbf{l}/dt$, where l is the position of the particle, it follows that

$$d\mathbf{p} = \pm d\mathbf{l} \times \mathbf{B}. \tag{2.3}$$

Since most particles in our experiment were produced with a large forward boost, we can take $d\mathbf{l} \approx dl\,\hat{\mathbf{z}}$, where $\hat{\mathbf{z}}$ is taken along the beam direction. For E791, the magnetic field pointed upward, that is, $\mathbf{B} = +B\hat{\mathbf{y}}$. Eq. (2.2) then reduces to

$$d\mathbf{p} = \mp B\, dl\, \hat{\mathbf{x}}. \tag{2.4}$$

Thus, the change in momentum is independent of the initial momentum of the incoming particle. The net result was a horizontal bending of all positively charged particles towards the west side of the spectrometer and to the east for negatively charged particles. A plot showing the strength of the y-component of the magnetic field B_y inside the first magnet M1 is shown on Figure 2.4.

2.3.5 Momentum resolution

The momentum resolution depends essentially on two factors: how well can one measure the exact curvature of a charged track using the tracking system and on how much material will cause the particle to scatter away from its course. Multiple scattering goes as Z^2/p and depends on the amount of material on the charged particles path. One can parametrize the momentum resolution to take into account the effects of improperly measured curvature in the tracking system and deviations due to multiple scattering. We can write

$$\frac{\sigma(p)}{p} = A\% \left(\frac{p}{100GeV/c}\right) \sqrt{\left[1 + \left(\frac{BGeV/c}{p}\right)^2\right]} \tag{2.5}$$

where A and B are constants to be extracted from the data. In E791 data, these constants depend on how well the particle is tracked. The constant A ranges from 1.3% (if the particle is tracked from the SMD's down to the last drift chamber) to 33% for tracks detected in the first drift chamber only. Similarly, B takes on values ranging from 3.8 GeV/c for particles going through all tracking devices, hence encountering a maximum amount of material, down to 0.9 GeV/c for tracks detected only in the first drift chamber.

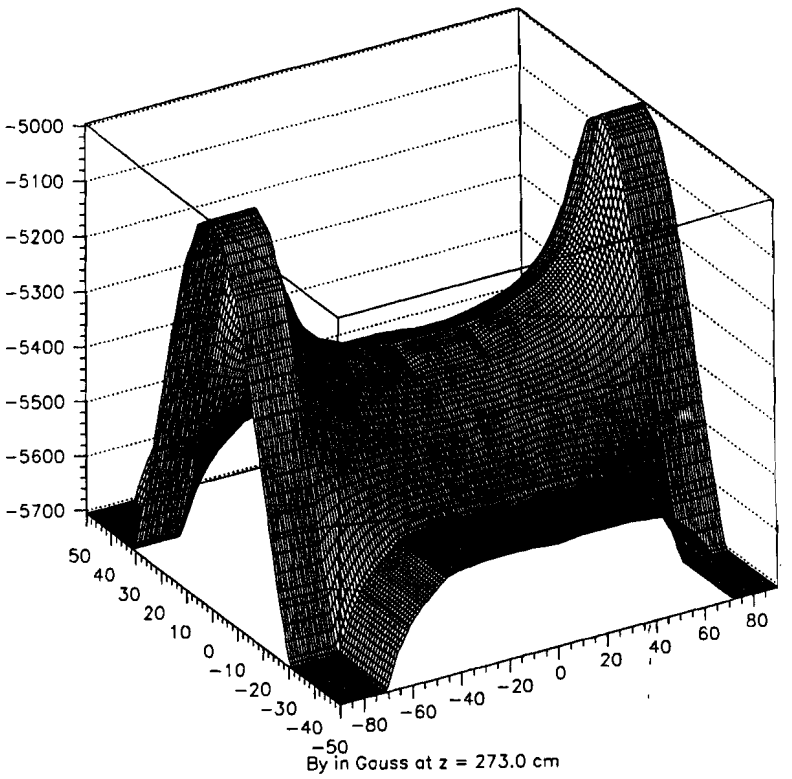

Figure 2.4. The mapping of the magnitude of the y-component of the magnetic field B_y inside the M1. Since the magnetic field points upward, charged particles travelling along the beam direction are deflected into an horizontal plane.

The momentum resolution can also be extracted directly from the data by looking at the measured width of weakly decaying particles such as the D mesons. If the detector was perfect (i.e. with infinite resolution and not inducing any multiple scattering), these long-lived mesons would have no measurable widths. In E791 data, D^+ mesons from the decay $D^+ \to K^-\pi^+\pi^+$ exhibit a width of 12.4 MeV whereas 2-body decays such as $D^0 \to K^-\pi^+$ yield a width of 2.9 MeV.

2.3.6 Vertex resolution

The primary vertex resolution along the beam axis can be extracted from a fit to the distribution of the z-position of a large number of primary vertices. The shape of the distribution was assumed to be a convolution between a Gaussian distribution and a square box of width equal to the foil thickness. The downstream target foils

exhibit a slightly poorer resolution due to multiple scattering in upstream foils. The extracted resolutions vary from 240 μm for the most downstream target foil to about 450 μm for the first, thicker platinum foil. Details are shown on Figure 2.5. The exact position of each of the five target foils along the beam axis can easily be seen from the plot as well as the interaction counter.

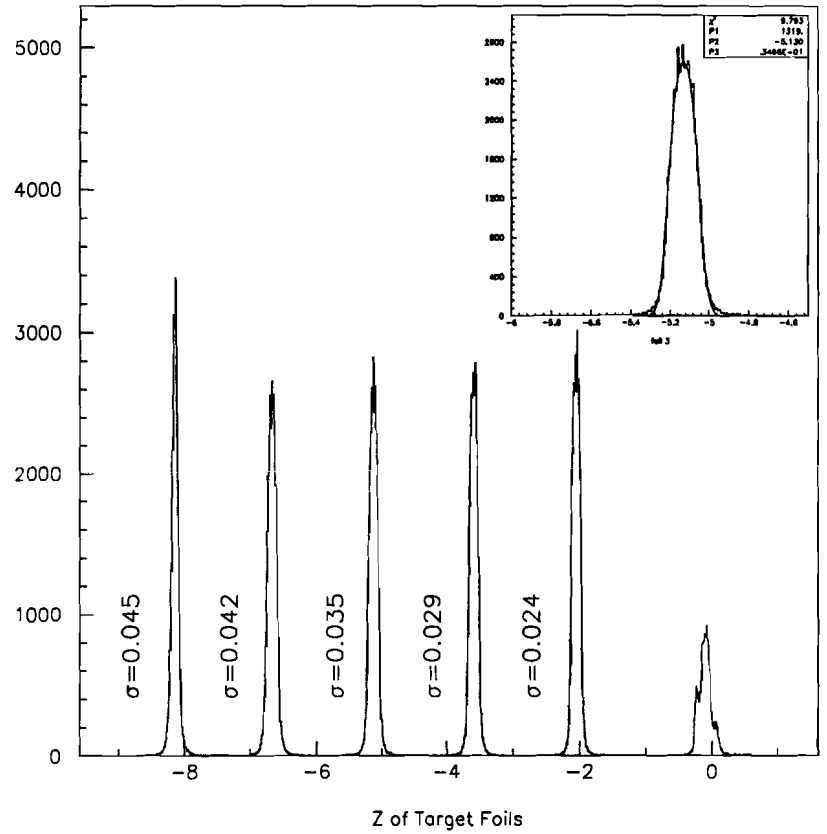

Figure 2.5. The reconstructed position of the primary vertex along the beam direction. The insert shows the fit to a convolution of a Gaussian and a step function for the third target foil. The exact z-position resolution for each vertex is indicated in cm next to each target foil.

2.4 The Čerenkov counters

For particle identification, E791 used two large gas Čerenkov threshold counters (referred to as C1 and C2), filled with different gas mixtures. They operate based on the fact that a particle traveling faster than the speed of light in a medium of index of refraction n emits ultraviolet light. This light is confined to a cone of half-angle θ given by [19] $\sin\theta = 1/\beta n$ where $\beta = \frac{v}{c}$, the ratio of the particle speed to the speed of light in vacuum. Since $\sin\theta$ cannot exceed one, βn must be smaller than unity to describe a physical process. This defines a threshold velocity β_{th}, given by $\beta_{th} = 1/n$ below which no light is emitted. Hence, a particle of mass m will leave a signal in a Čerenkov counter only above a momentum threshold set by the relation

$$p_{th} = \gamma m v_{th} = \gamma m \beta_{th} c = \gamma mc/n. \tag{2.6}$$

Substituting $\gamma = (1 - \beta_{th}^2)^{-1/2}$ with $\beta_{th} = 1/n$ leads to

$$p_{th} = \frac{mc}{\sqrt{n^2 - 1}}. \tag{2.7}$$

With a typical n close to 1, it is useful to define $\delta = (n - 1)$ and to expand in δ to reduce Eq. (2.7) to

$$p_{th} = \frac{mc}{\sqrt{2\delta}}. \tag{2.8}$$

For a particular value of momentum measured in the drift chambers, only particles below a certain mass will emit Čerenkov light in a gas of given index of refraction. By incorporating two such counters using gas mixtures with different indices of refraction, one can set limits on the mass of the incoming particle and identify it in certain momentum ranges. For example, in the Tagged Photon Spectrometer, only pions and lighter particles, such as muons and electrons, can generate a signal in both counters between 6 and 20 GeV; therefore, in this momentum range, they can be distinguished from protons and kaons.

Each Čerenkov counter was made of an array of spherical mirrors coupled to light collecting devices known as Winston cones, which have a 20° opening angle for enhanced light collection. RCA 8854 photomultiplier tubes collected the signal and were read by FERA's (ADC's described in the calorimeter section). Figure 2.6 gives a schematic view for each chamber. The tubes in C2 had to be flushed with a constant stream of nitrogen to avoid having helium ruin the phototubes. Table 2.6 summarizes the characteristics of both Čerenkov counters.

To calibrate the Čerenkov counters, one had to determine both the gain and threshold for each phototube associated with a given mirror. This procedure was

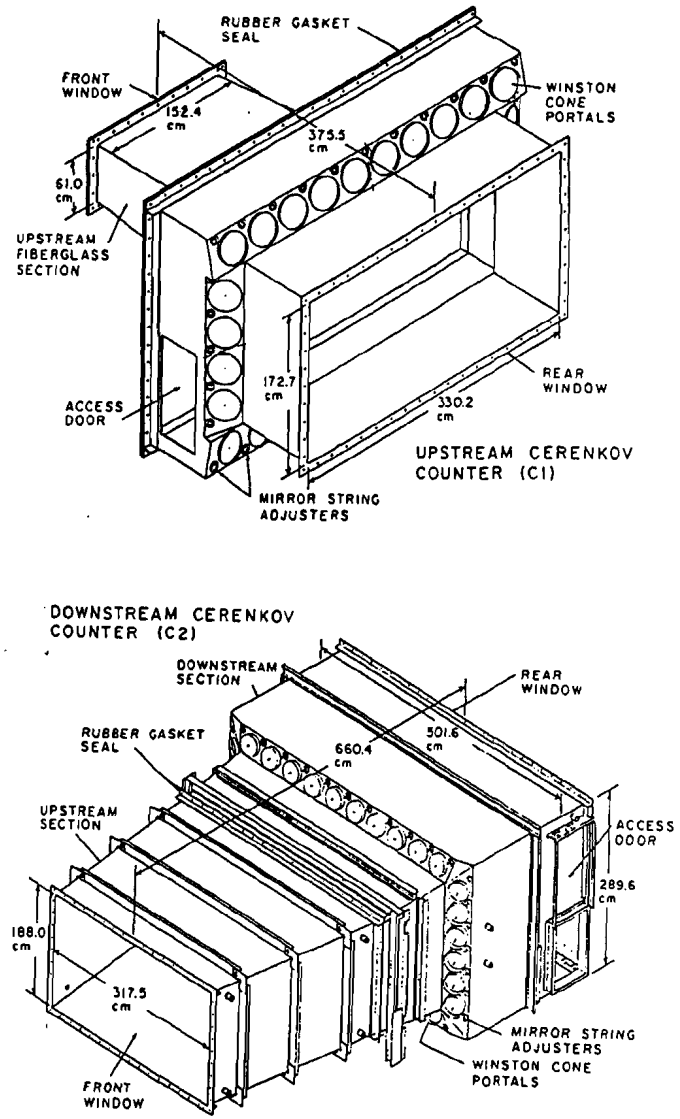

Figure 2.6. Schematic view of both Čerenkov counters.

Table 2.6 Properties of the Čerenkov counters.

	C1	C2
length (m)	3.7	6.6
number of mirrors	28	32
gas mixture	100% N_2	80% He- -20% N_2
$\delta = (n-1)$	290×10^{-6}	86×10^{-6}
pion momentum threshold (GeV/c)	6	11
kaon momentum threshold (GeV/c)	20	36
proton momentum threshold (GeV/c)	38	69

carried out using tracks for which the ellipse* of Čerenkov light did not intersect mirrors illuminated by other tracks. Each of these tracks was assumed to have been produced by an electron, giving the largest possible ellipse. The mean number of photons emitted per unit length by a particle with velocity βc is given by [2.6]

$$\frac{dN}{dl} = 2\pi\alpha \int \left(1 - \frac{1}{\beta^2 n^2(\lambda)}\right) \epsilon(\lambda) \frac{d\lambda}{\lambda^2}, \tag{2.9}$$

where

α = the fine structure constant = 1/137,

$n(\lambda)$ = the index of refraction at wavelength λ,

$\epsilon(\lambda)$ = the detector efficiency at wavelength λ.

Figure 2.7 shows the excitation function described by Eq. (2.9) for C1 and C2 as a function of momentum and particle type. In Figure 2.7 , $\epsilon(\lambda)$ was set to one for wavelengths between 1600 and 5000 Å, zero otherwise.

A fit to the measured number of photons detected by a single counter to the theoretical curve described by Eq. (2.9) yielded the values for the gain and threshold. Once the gains were known for each phototube, it was possible to predict the number of photoelectrons each particle type would generate at a given momentum. For each particle entering the counters, the probability that the particle was of a particular type is calculated based on a comparison between the amount of light actually collected to the expected number of Čerenkov photons for each particle type at a given momentum.

* The light cone can have an elliptical crosssection due to the angle of the particle at production or the transverse kick of the magnet.

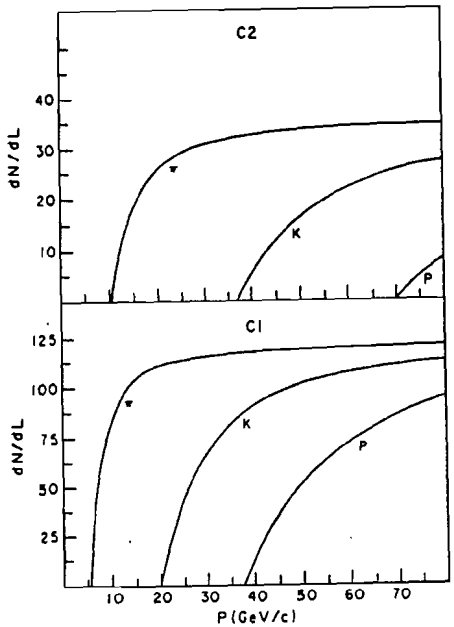

Figure 2.7. The excitation function described by Eq. (2.9) for C1 and C2 as a function of momentum and particle type. $\epsilon(\lambda)$ was set to one for wavelengths between 1600 and 5000 Å, zero otherwise.

The probability was estimated based on Poisson statistics [22]. The probability that n photons are observed in counter i if the particle has type j is given by

$$f_{i,j}(n;\mu) = \frac{\mu^n e^{-\mu}}{n!}, \tag{2.10}$$

where μ is the predicted number of photons for particle type j. Combining the probabilities from the two counters C1 and C2, we get the total probability that a particle of type j produced the observed signals:

$$f_j = f_{1,j} \times f_{2,j}. \tag{2.11}$$

The final probability P_j used for particle identification was normalized by taking into account the a priori expectation based on the assumed natural occurence of each particle type in the data; that is,

$$P_j = \frac{f_j}{\sum_{k=1}^{5} f_k \times A_k}, \tag{2.12}$$

where A_j is the a priori expectation as given in Table 2.7.

Table 2.7 Čerenkov identification parameters: the particle type and a priori probability (the assumed fractional content in an arbitrary event.)

particle type	a priori probability
electron	.02
muon	.01
pion	.81
kaon	.12
proton	.04

2.5 Calorimetry

There were two calorimeters at the Tagged Photon Lab: the Segmented Liquid Ionization Calorimeter (SLIC) (an electromagnetic calorimeter), and the hadrometer, designed to detect energy deposition from hadrons. Both were used as part of the trigger, selecting events with large energy deposition transverse to the beam line. The assumption was that charm quarks, being very massive, should give large transverse energies to their decay products. Used in conjunction with the Čerenkov counters, tracking detectors and the muon wall, the calorimeters were part of the particle identification system since electrons, photons, muons and hadrons have very different energy deposition patterns in the calorimeters.

2.5.1 The SLIC

The SLIC was designed to maximize the energy deposition from particles which interact primarily through the electromagnetic interaction, that is, electrons and photons. Electrically charged particles radiate photons via bremsstrahlung when passing through dense materials called radiators (such as lead) because of acceleration in the electric field of the nucleus. [19] Electrons* are mainly subject to this energy-loss process since the number of bremsstrahlung photons emitted by a particle is inversely proportional to the square of its mass. The radiated photons caused by the bremsstrahlung process convert to e^+e^- pairs in the vicinity of a nucleus. This process of pair production and radiation repeats itself until all the energy of the incoming particle has been radiated away.

The SLIC is constructed of thin layers of lead in which the shower of photons, electrons and positrons develops. Between these passive layers of radiator, an active material (liquid scintillator) detects the electrons and positrons in the shower,

⋆ Unless otherwise noted, "electron" refers to electrons or positrons.

emitting ultraviolet photons. A waveshifting solid material at the edges of the detector absorbs the UV photons and and re-emits them in the visible range where photomultiplier tubes are most sensitive.

The SLIC is composed of 60 layers of lead [24] and liquid scintillator, each layer corresponding to one third of a radiation length. Each liquid scintillation layer was optically separated into parallel strips by means of teflon-coated corrugated aluminum which provided channels with total internal reflection surfaces. The scintillation light which propagated roughly parallel to the axis of the strips exitted the tank and was detected by a wavebar-phototube readout scheme. The axes of the strips were organized so that each shower was detected in three views giving three coordinates for the transverse position of each shower.

Each scintillating layer was 1.27 cm thick. The thickness was determined by the teflon-coated sheet aluminum corrugations which were inserted just after a front aluminum sheet. The corrugations had a square-wave shape with a half wavelength of 3.17 cm which defined the width of the scintillator strips. The axis of the corrugations was at an angle of $\pm 20.5°$ and $90°$ from the vertical, forming the U, V, and Y views, respectively. The corrugations formed 109, 109, and 116 separate U, V, and Y channels. The Y channels were also separated at the midplane into 58 east and 58 west channels. The corrugations and layer pattern are shown in Figure 2.8 and the SLIC parameters are listed in Table 2.8. The light from each channel and 20 layers in depth for each view was collected by a single readout phototube. Each readout, plus the associated liquid scintillation region which is viewed by that readout, is called a "counter".

The light generated in the scintillator layers propagated along the teflon channels within the $20°$ total internal reflection cone. One end of each channel was terminated by a $90°$ mirror with a reflectivity of about 80%. Light propagating in the other direction reached the edge of the SLIC and exitted through a lucite window. This light was collected by phototubes glued to wavelength-shifter bars and converted into linear current pulses. Under ideal conditions, all light entering the wavebar will undergo total internal reflection and reach the photomultiplier tube at the end. However, due to oil which leaked out of the detector onto the wavebars, several of the wavebars did not transmit all the light resulting in a lower light yield at the phototube. Several wavebars, for which this problem was particularly severe, were extensively cleaned before the run began. Voltages applied to the phototubes varied from 1500 to 1800 Volts although several tubes had to be powered at slightly higher voltages to compensate for lower light yield.

In the center of the SLIC, where more particles are incident and hence, finer spatial resolution is needed, each 1.25-inch-wide counter was read out by a single 3-in RCA 4900 photomultiplier tube. At the sides of the detector, 71 U channels, 71 V channels and 36 Y channels were read out with one 5-in RCA 4902 photomultiplier tube for

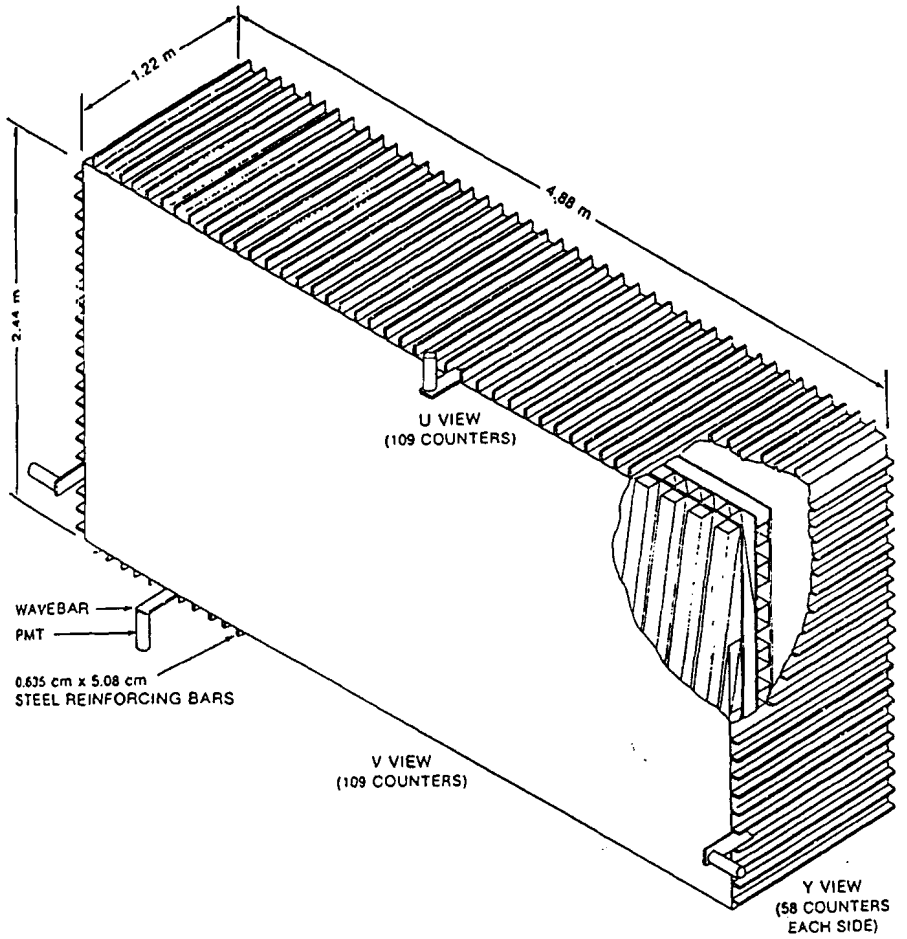

Figure 2.8. A schematic view of the SLIC. The cutaway shows the first layer of the U, V and Y views.

two channels. The overall spatial resolution for locating the centroid of the electron shower was about 7 mm. With a total thickness of 20 radiation lengths, the SLIC design guaranteed good energy containment of electromagnetic showers. Moreover, the multilayer structure provided fine segmentation along the z-direction, allowing the assumption that equal amounts of energy were deposited in all views, an assumption that was used in the calibration process. The energy deposited by a charged particle or photon is proportional to the light collected at the phototube after correcting

Table 2.8 SLIC parameters.

	U channels	V channels	Y channels
number of channels	109	109	116
orientation from vertical	$-20.5°$	$+20.5°$	$90°$
number of layers	20	20	20
single channel width (cm)	3.17	3.17	3.17
channel length (cm)	110.4	110.4	46.25
view ordering	U, V, Y		
upstream z-position (cm)	1866.		
downstream z-position (cm)	1962.		
active area (cm^2)	490. $\times$ 240.		
scintillating material	scintillator doped with mineral oil		
radiating material	lead		
total radiation length	20		
total absorption length	1.5		
energy resolution	$(\frac{\Delta E}{E})^2 \approx \frac{(17.4\%}{E)^2} + (11.5\%)^2$		
position resolution (cm)	~ 0.65		

for attenuation in the scintillator and wavebar. Corrections for attenuation in the scintillator were made once the location of the shower was determined. Corrections for attenuation in the wavebar are made since different types of particles produce energy showers with different energy distributions in depth. This is discussed below in the SLIC calibration section.

2.5.2 The hadrometer

Just behind the SLIC, there was a second calorimeter intended to detect both hadrons and muons. Hadrons can lose energy due to interactions with the nucleus via the strong interaction when travelling in a high density region. About half the incident energy is passed on to additional fast secondaries [19]. A typical secondary hadron is produced with a transverse momentum of about 350 MeV/c, such that hadronic showers tend to be much wider than electromagnetic ones, a fact that was taken into account when designing the hadrometer as will be discussed below. The

second largest energy loss is due to the production of π^0's which in turn decay into two photons, giving rise to an electromagnetic shower within the hadronic shower. Hadrons can also lose energy (but at a much lower rate) through ionization. Since muons principally lose energy through ionization, they deposit only a small fraction of their energy in both the electromagnetic and hadronic calorimeters.

To maximize nuclear interactions with hadrons, and hence, maximize their energy deposition, the hadrometer was made of alternating layers of steel (used as radiator) and plastic (the scintillator). The hadrometer [25] was divided into front and back modules, each consisting of 18 3/8-in thick plastic scintillator layers. These plastic layers were interleaved with 36 one-inch thick steel plates for a total thickness of six interaction lengths. The hadrometer was segmented along two views, with separate scintillating plastic strips in the X and Y directions forming the individual counters. The X counters spanned the full height of the detector whereas the Y counters were divided at the vertical midplane. Each module was read separately resulting in 33 X counters and 38 Y counters in both the front and back modules for a total of 142 hadrometer channels. A single phototube collected the light output along the z-direction. Even though this prevented access to information on the longitudinal development of the shower, comparison between the energy deposited in the front and back modules provided some information to separate muons and hadrons. A detailed view of the device is given in Figure 2.9, and Table 2.9 lists all the relevant hadrometer parameters.

Each wavebar for an individual counter (X or Y, front or back) was connected to a single phototube, a 5-inch EMI 9791KB glued to a lucite lightguide. Since its energy resolution was about $\frac{75\%}{\sqrt{E}}$, the hadrometer's main function was to provide information for the E_t trigger. Since hadronic showers tend to develop more slowly than electromagnetic ones, a longer gate on the digitizers was used to read hadrometer channels than SLIC channels. A 190 ns gate was selected for the hadrometer whereas a 160 ns gate was deemed sufficient for the SLIC.

The hadrometer channels were designed to take into account the width of a typical hadronic shower. The width W of a shower for which 99% of the energy is contained can be estimated as a function of energy as [19]

$$W(E) = -17.3 + 14.3\ lnE, \tag{2.13}$$

where the width is given in cm and the energy in GeV. This yields a width of about 6–40 cm for particles in the 5–50 GeV range. The hadrometer channels were built 14.5 cm wide, yielding a poorer spatial resolution than the electromagnetic calorimeter but well matched to a typical hadronic shower width.

Since the SLIC was 20 radiation lengths thick, good containment of most electromagnetic showers was to be expected. For example, the ratio of energy deposited

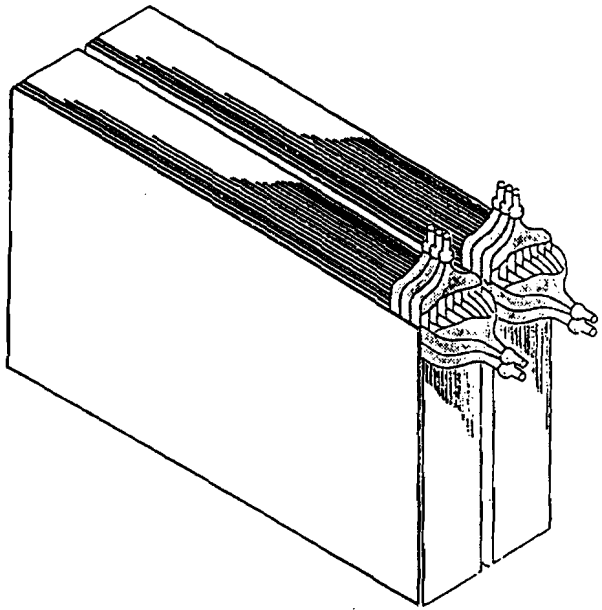

Figure 2.9. Detailed view of the hadronic calorimeter.

in the hadrometer to that deposited in the SLIC was found to be zero for 70% of electrons and positrons from converted photons in the 2 to 40 GeV/c momentum range. For charged pions selected from K_s^0 decays, the ratio of E_{had}/E_{SLIC} is zero for only 34% of pions in the same momentum range. This fact was used in the offline reconstruction to help achieve good e/π separation, as detailed in chapter 4.

2.5.3 Calibration of the calorimeters: Overview

The goal of the calibration procedure was to convert the signal pulse height recorded in the FERA ADC's to the amount of energy deposited by a particle, for each channel of both calorimeters. Four sources of charged particles were available for calibration: isolated muons and isolated electrons from special calibration runs, and isolated electrons and charged hadrons selected from the regular data runs. Because essentially all the electron energy is deposited in the SLIC and because the momentum of each electron is measured in the tracking system, the calibration electrons provided the best absolute calibration. However, the number of channels which received a sufficient flux of electrons in the calibration runs was limited. Therefore, muons were useful because of their complete coverage of the SLIC. But, since muons are minimum-ionizing particles, they produced very small signals corresponding to about the sixth channel out of 2048 channels in the FERA's. Therefore the precision with which the calibration constants can be determined using muons is limited.

Table 2.9 Hadrometer parameters

	X channels	Y channels
number of channels	66	76
number of layers	36	36
single channel width (cm)	14.5	14.5
view ordering	X, Y	
interacting material	steel	
scintillating material	plastic*	
absorber thickness (cm)	2.54	
total interaction length	6	
upstream z-position (cm)	1973.	
downstream z-position (cm)	2131.	
active area (cm^2)	490. × 270.	
energy resolution	$\frac{\Delta E}{E} \approx \frac{75\%}{\sqrt{E}}$	

* polymethyl methacrylate doped with 1% PPO and .01% POPOP

Consequently, as many U and V SLIC channels as possible were calibrated using the special electron calibration runs. Then, with the muon calibration runs, these calibrated channels were used to determine the energy deposited by a muon. This number was then used to determine the absolute calibration of the remaining U and V channels. Finally, the Y channels were calibrated using isolated electrons from regular data runs by setting the signal measured in the Y view equal to the signals measured in the U and V views. For the hadrometer, we injected the conversion factor used by E769 and E691 to determine the absolute energy deposited by muons. The accuracy of this conversion factor was checked by selecting isolated hadronic showers from the regular data runs. The details of these calibration procedures are given in the following sections.

After calibration, electron/positron pairs from converted photons and photon pairs from π^0 decays from regular data runs were used to check the accuracy of the calibration constants. The energy resolution was measured both for isolated electrons from calibration runs and for electrons from photoconversions. The fractional resolution σ_E/E was measured as a function of $1/\sqrt{E}$ and found to be $17.4\%/\sqrt{E}$ plus a constant term of 11.5% (to be added in quadrature) for electrons in normal data.

2.5.4 Calibration procedure with muons

A fairly uniform spray of muons over the whole surface of the calorimeters was obtained by closing collimators upstream from the target. We used the output of a first muon run and participation plots from the online monitoring system to adjust the voltage on each phototube until all gains were roughly balanced. Once the voltage on each phototube was fixed, muon data was collected and analysed to determine the attenuation parameters for each of the 334 SLIC channels and 142 hadrometer channels. This attenuation is due to absorption by the scintillating material and depends on the distance between the shower location and the position of the phototube. The attenuation parameters were extracted from a fit to an exponential decay curve.

After correcting for attenuation, we determined the peak number of ADC counts for muons for each channel by fitting the data to a Landau distribution for each channel separately. The fitting procedure allowed us to determine the peak position to within $\pm$ 5-7%, much better than $\pm$ 1 bin achievable without a fit.

We used the results of ten muon runs covering a period of 130 days throughout the run to monitor the gains for a possible drift over time. Each one of the ten gain files was compared to a standard file, choosen when all adjustments to the high voltage were final. The ten ratios were fitted versus time to a straight line where time is measured relative to the standard run. The intercept and slope were extracted for each SLIC and hadrometer channels. The gains were found to increase on average by about 1.3% per month for the SLIC whereas the hadrometer exhibited an average gain decrease of 1.42% per month. The final gains were corrected channel-by-channel for this drift. Since the muon peak was found around the sixth bin in the FERA's, a change by as little as one count in the pedestal value during a muon run would have been sufficient to account for a 16% change in the gain value. However, monitoring of the pedestal values over time showed that they were stable during a run. Pedestals fluctuated with sigmas of the order of 0 to 0.5 during one run and within 0.1-0.6 over a period of 12 runs. The corrections for drift over time helped smooth out variations due to small changes such as pedestal fluctuations.

2.5.5 Absolute calibration of the hadrometer

Using muons, we could only achieve a relative calibration of the calorimeter channels. To convert the minimum ionizing muon peak position from ADC counts to energy, one must know the exact amount of energy deposited by a muon in the calorimeters. For the hadrometer, we first relied on measurements from all previous experiments at TPL. The conversion factor was known to be about 1.2 GeV/muon, that is, for a muon peak found in the sixth bin, the gain for that channel would be about 5 counts/GeV. To check the validity of that figure and make sure that we had the correct calibration constants for all channels of the hadrometer, we selected

hadrons from normal data and made a scatter plot of the ratio E/p for the energy they deposited in each calorimeter. For relativistic hadrons, one can neglect their mass and expect that their total energy be equal to their momentum. Assume

$$E_{total} = \alpha\ E_{SLIC}\ +\ \beta\ E_{had} \tag{2.14}$$

and $E_{total} = p$. It was found that the values of the parameter α andβ depended on the type of event. An event is said to be congested when other charged tracks in the selected event point to the same hadrometer counters. Congestion occurs for about two thirds of the tracks. The values of α and β for congested events were found to be 2.1 and 1.0 and, for non-congested events, 2.0 and 0.7 . Figure 2.10 plots the total energy as parametrized by equation (2.14) both for non-congested and congested events. The ratio E_{total}/p peaks at one but with a rather broad distribution, especially in the case of congested events.

2.5.6 Absolute calibration of the SLIC using electrons

Electrons were used for absolute calibration since electrons are the only charged particles to deposit all their energy in the SLIC. The electron energy was determined by measuring its momentum in the tracking system and setting the ratio of energy to momentum equal to one.

For electron calibration run, a 20-GeV electron beam hit a thin aluminum plate placed in the beam path near the target, giving a secondary beam of electrons and positrons created by photoconversion. Electrons and positrons in the 3 $-$ 20 GeV energy range were detected in the fiducial volume of the SLIC. The electrons were found on the east side and the positrons on the west side of the SLIC. These special calibration runs were repeated every other week throughout the experiment. The electrons from the electron calibration beam were not uniformly distributed over the surface of the SLIC. They lay in a horizontal plane through the center of the SLIC since the magnets in the beamline and the detector bent charged particles in the horizontal plane. The short outermost U and V channels and most of the Y channels, did not lie in the path of the electrons. About 143 out of 218 U and V channels were hit by the electron beam. We used the full reconstruction code iteratively on this "electron" data and adjusted the calibration constants such that the ratio of energy to momentum was exactly one, as desired for electrons. For these channels, we measured the exact gain by converting ADC counts to GeV using the known momentum of the electrons.

For the remaining channels, we needed to extract the muon equivalent energy deposition. Using the 143 calibrated channels, we compared the muon peak position with the established gain for each channel. The energy deposited in the SLIC by muons was found to be less than what was determined by E691 and E769 due to

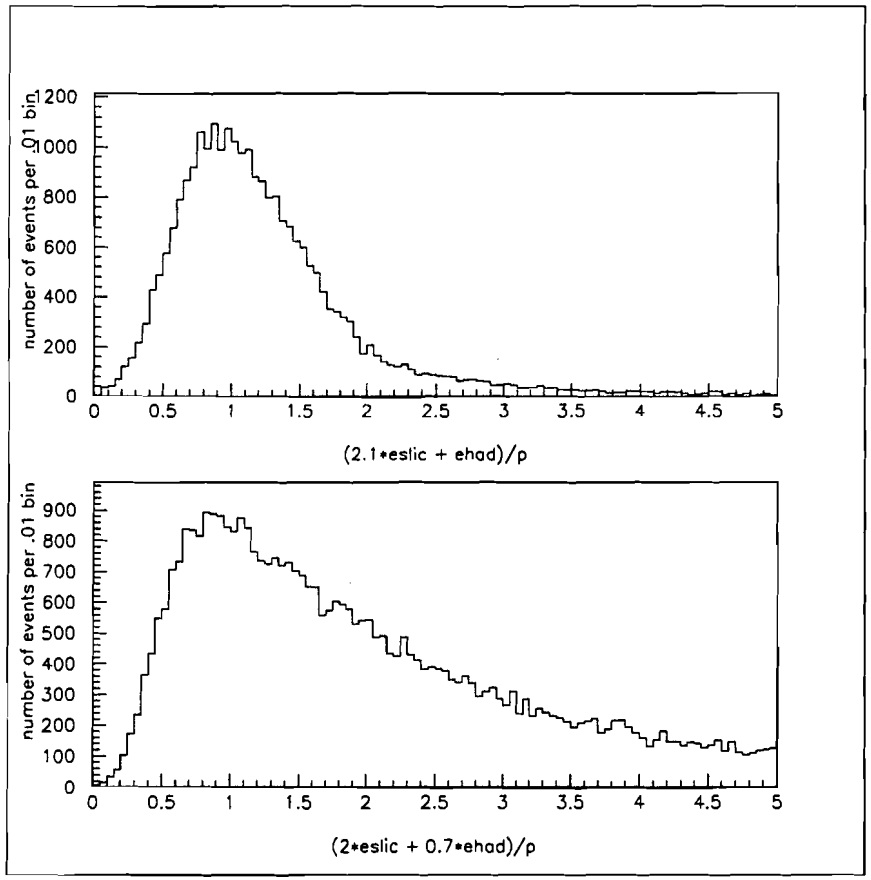

Figure 2.10. Total energy deposited by pions from K^0_s decays in both calorimeters according to the parametric equation given by Eq. (2.14) for non-congested events (top) and congested events (bottom), respectively.

general deterioration in signal transmission in the wavebars. A more careful analysis revealed that the amount of energy deposited by muons varied according to the readout of the channel: the channels near the center were each read out with one PMT tube (single-width readout); near the edges of the SLIC the light from two channels was collected by a single PMT (double-width readout). Moreover, due to spatial restrictions, for some of these double-width channels the phototube only covered half the wavebar and collected only half the light (double-width, half-readout). We extracted three different values for the average equivalent muon energy for the U and V channels, corresponding to channels with single-width readout, or double-width with full or half readout configurations. We obtained a rough estimate of the

gain using these three conversion factors for the channels that had not been directly calibrated using electrons. This first but lengthy step allowed us to get an initial set of calibration constants accurate enough to provide a balanced gain for all channels. This was necessary in order to carry out the next step efficiently.

To obtain a final value for the calibration constants, we compared the energy found in one view to the energy seen in the two other views for isolated electromagnetic showers selected from regular data. We corrected the calibration constants on all channels that had not been hit directly by the electron beam such that the ratio of energy with the two other views would come out to one. By successive iterations, this process allowed us to correct the calibration constants to account for non uniform changes in attenuation over the years due to opacification of the wavebars. Small changes in attenuation in the wavebars over the years affect the relative amount of light produced by muons and electrons differently, since muons deposited their energy uniformly whereas the electrons energy, on average, peak about six radiation lengths into the SLIC. Different changes in attenuation explained why all channels did not have exactly the same value for the muon deposited energy and required some tweaking. A correction to the muon equivalent energy for a given channel was calculated for only one run and applied to all the other runs. On average, the Y channels exhibited different conversion factors for the muon equivalent energy for single and double-width channels, namely 424 and 400 MeV/muon. The muon peak was converted into an absolute gain in counts/GeV using the corrected value of the muon equivalent energy calculated for each channel. A summary of the average deposited energies for the different channel types is given in Table 2.10. The overall uncertainty on the calibration constants was estimated to be about 3% from the fitting procedure, after correcting each channel gain for drift over time.

Table 2.10 Different values of muon equivalent energy by geometry type.

geometry type	U and V channels	Y channels
half readout, double width	341 MeV	
full readout, double width	371 MeV	400 MeV
full readout, single width	352 MeV	424 MeV
E769 universal value	$\sim$ 420 MeV	
E691 universal value	$\sim$ 460 MeV	
E516 universal value	$\sim$ 495 MeV	

The final check of the accuracy of these calibration constants was done by calculating the invariant mass of pairs of photons from normal data. The ratio of the

reconstructed π^0 mass to the real π^0 mass provides a calibration check. A difference is to be expected between electron and photon calibration since the formation of ionizing particles starts roughly one radiation length further into the SLIC for photons than for electrons. Therefore, the light output is slightly more attenuated in the wavebar for photons. From the measured π^0 invariant mass no special correction for photons was deemed necessary.

Finally, we looked at the E/p and $(E-p)/\sigma_E$ ratios for selected electron-positron pairs from photoconversions in normal data. As expected for electrons, the ratio of E/p came out to one. Figure 2.11 displays $\left((\sigma_{E/p})/(E/p)\right)^2$ as a function of $1/p$ for combined electrons and positrons. The points in Figure 2.11 were fit to a straight line. The final resolution σ_E/E was estimated to be about $17.4\%/\sqrt{E}$ plus a constant term of 11.5% to be added in quadrature. A small difference was found between the east and west sides of the SLIC, which can be understood considering that all channels with half readout lay in the east side of the SLIC. The cuts used to select the photoconversion pairs are discussed in more detail in the electron identification chapter.

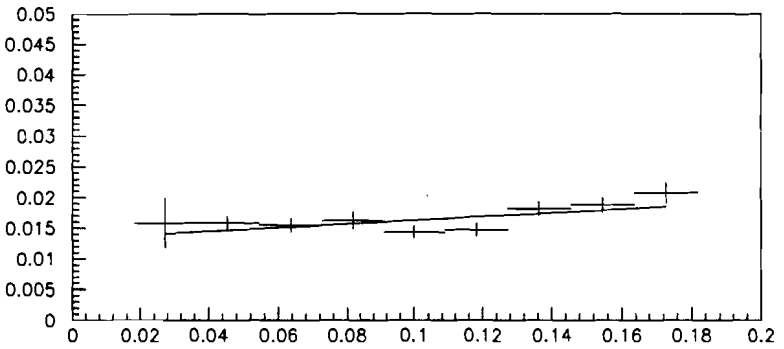

Figure 2.11. $\left((\sigma_{E/p})/(< E/p >)\right)^2$ versus 1/p for electrons and positrons. From the fit, the final resolution σ_E/E was estimated to be about $17.4\%/\sqrt{E}$ plus a constant term of 11.5% to be added in quadrature.

2.6 The muon wall

As seen in the previous section, hadrons lose most of their energy via the strong interaction while photons and electrons interact only electromagnetically, mainly through bremsstrahlung and photoconversion. Hence, most particles are completely absorbed in the two calorimeters. Muons interact mainly through ionization and consequently retain most of their energy even after going through both calorimeters. These minimum ionizing particles are easily detected with simple scintillating paddles attached to phototubes.

E791 had two muon walls made of scintillating paddles placed at the end of the spectrometer directly behind a 106 cm-thick steel shield wall meant to block hadrons that had not interacted in the calorimeters. A 1 m-thick concrete block was also placed between the X and Y walls. Only muons above 4 GeV and a few punch-through hadrons were seen in the muon walls.

The first muon wall, the X-wall, consisted of 15 vertical paddles, each 40.6 cm-wide, placed 2243 cm downstream from the target. The second wall, the Y-wall, was found 176 cm downstream from the X-wall and had 16 14.2 cm-wide paddles. Together, the X and Y-walls covered an area of 300.0 by 224.0 cm. There were four additional shorter paddles covering the central region of the X-wall to lower the noise rate in that area. These shorter paddles were placed such as to overlap another X paddle near the beam axis. Signals from the central X paddles were used in coincidence with the shorter paddles. In the reconstruction algorithms, the noise in the central X paddle could be reduced by 90% by requiring a simultaneous hit in both shorter and longer overlapping paddles. The geometry for both walls can be seen in Figure 2.12.

The light emitted when a charged particle went through the scintillating paddles was collected by photomultiplier tubes connected to each paddle via a light guide. The electrical pulses from the PMT's were sent into discriminators, then to the TDC's to record the time at which the particle reached the wall. The pulses from the X-counters were also sent into latches. This allowed the use of simplified algorithms to identify muons. The spatial resolution transverse to the paddle was determined by the width of the paddles. The spatial resolution along the length of the paddle was obtained from the time of the pulse from the TDC information. The TDC's time resolution was measured to be 3 and 2 ns for the X and Y-wall respectively. Given that the paddles were made of material with different indices of refraction, hence different light velocities, this corresponded to longitudinal spatial resolution of 45 and 25 cm respectively. Table 2.11 summarizes the muon wall characteristics.

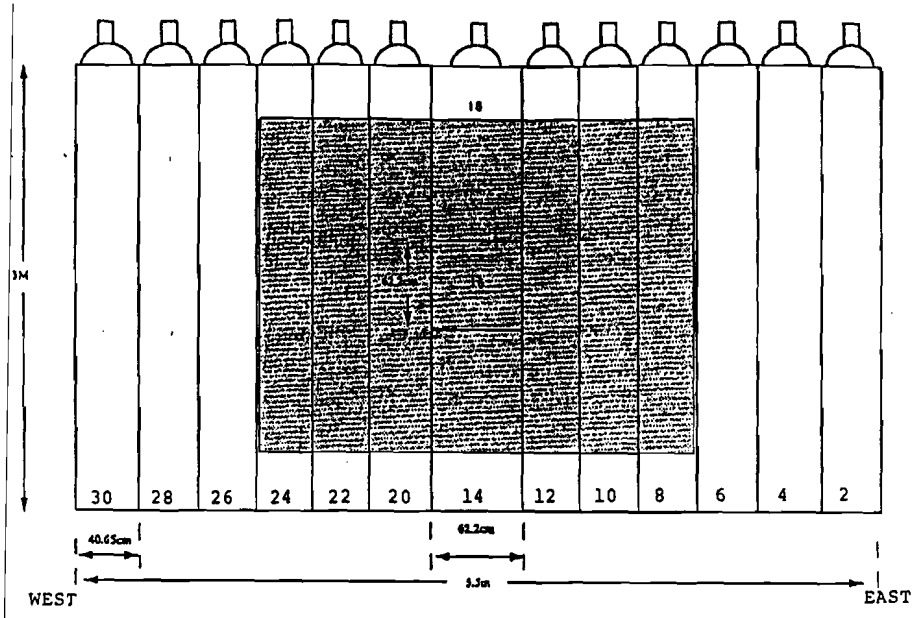

Muon X-wall

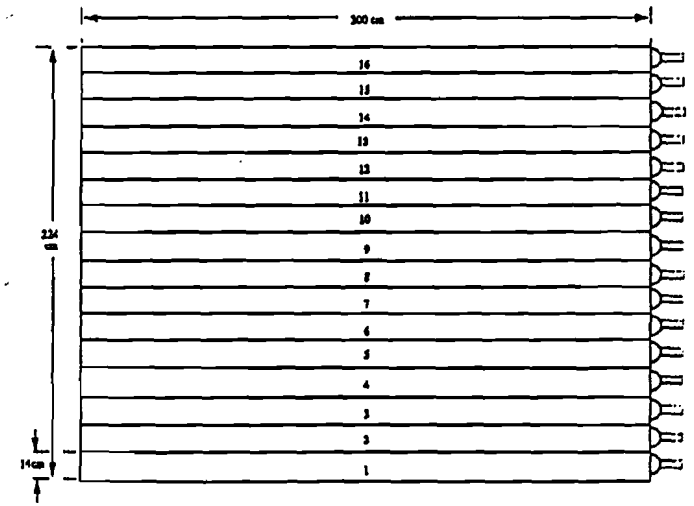

Muon Y-wall

Figure 2.12. The configuration of the X and Y muon walls.

Table 2.11 The various parameters for the muon walls.

	X-wall	Y-wall
number of long channels	15	16
number of short channels	4	0
channel width (cm)	40.6	14.2
z-position (cm)	2243.	2419.
x-position resolution (cm)	11.7	25.
y-position resolution (cm)	45.	3.5
view ordering	X, Y	
scintillating material	plastic	
absorber thickness (cm)	176.	
absorber thickness	11.6 interaction lengths	
active area (cm^2)	300. × 224.	

July 1991: Dressed rehearsal for the E791 data acquisition system

3. Trigger and Data Acquisition System

Since charmed events are difficult to recognize in real time, E791 opted for an open trigger approach. The strategy was to impose only loose constraints when recording data, and select the events of interest offline when time and computing resources are more available. The E791 collaboration decided to maximize the charmed data sample by designing a data acquisition system to collect and record data at a very high rate.

3.1 The Trigger

The trigger strategy was based on the fact that the decay products of relatively massive charm quarks are produced with more transverse momentum than light quark decay products. For this reason, the E791 trigger was designed to select events in which the amount of energy deposited transverse to the beamline is comparable to the charm quark mass. The calorimeters (and not the drift chambers) were used for this measurement because it is impossible to design a track reconstruction algorithm fast enough to meet the trigger requirements. The E791 trigger was a two-level decision making process: a pretrigger decision made in about 160 ns, allowing for an early digitizing start, and a calorimeter-based trigger decision made in about 470 ns.

The pretrigger decision was based on three scintillation counters located in the vicinity of the target. Upstream of the target, a beam spot counter 0.5 in by 0.5 in and 0.1 in thick, was used to determine that one (and only one) beam pion was present. A beam halo counter, consisting of a 3 in by 3 in piece of scintillation counter 0.25 in thick with a 0.375 in diameter hole in it, was used to veto events that contained a particle far from the nominal beam axis. Downstream of the target, an interaction counter with a 0.75 in radius and 0.125 in thick was used to determine if an interaction had taken place. The signal from the interaction counter was required to be at least as large as the mean signal from five charged particles. The positions of the three scintillation counters used for the pretrigger decision are shown on Figure 3.1.

The second part of the trigger decision was based on the amount of transverse energy in the electromagnetic and hadronic calorimeters. Each calorimeter phototube was read through two different outputs: the full anode signal was directed toward the data acquisition system for digitization while the last dynode signal was directed towards the trigger logic which performed a weighted sum of the raw signals, giving more weight to signals far from the beam axis. This weighted sum gave an estimate of the total energy in an event for the trigger decision. A discriminator was used to reject events with transverse energy less than about 3 GeV. In addition, events with more than 700 GeV of total energy were rejected to get rid of events in which more than one beam particle interacted. The cutoff was set higher than the nominal incoming beam energy of 500 GeV to allow for fluctuations in the measured energy.

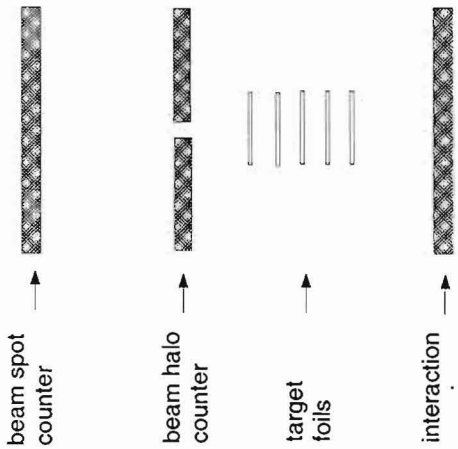

Figure 3.1. The layout of the scintillation counters used by the trigger logic.

The trigger requirements are summarized in Table 3.1. Most of the events recorded by E791 satisfied all the trigger requirements shown in Table 3.1. However, about 10% of the recorded data corresponds to events which satisfied only the pretrigger requirements. These are referred to as interaction triggers.

Table **3.1**. Trigger requirements.

pre-trigger requirements (160 ns)			
trigger definition	hardware used	accept	reject
live	digitizers DA	digitizers ready buffers not full	digitizers busy buffers almost full
good beam	beam spot counter beam halo counter	1 MIP/0.5 μs no signal	$\geq$ 2 beam particles no beam particle off-axis beam particles
interaction	interaction counter	$\geq$ 5 MIP's	no interaction
full trigger requirements (470 ns)			
transverse energy		$\geq$ 3 GeV	light quark production
total energy		$\leq$ 700 GeV	multiple interactions

3.2 Digitization and deadtime

The digitizers of most systems (the ADC's for calorimetry and Čerenkov counters, and the TDC's for the drift chambers and muon wall hodoscopes) had been replaced to match the capabilities of the new, faster data acquisition system (DA). A list of all digitizers used by the E791 DA and the digitization time associated with each is provided in Table 3.2.

The target thickness was chosen so that the deadtime due to digitization was about 50% given the beam rate and digitization time. The average time between beam particles was about 500 ns. Since this is greater than the 470 ns to make the full trigger decision, there was very little deadtime due to the trigger decision. With a target thickness equivalent to 2.2% of an interaction length, one in every 45 incoming pions on average interacted with the target. In other words, an interaction occured roughly every 25 μs. Approximately half of these interactions passed all the trigger requirements. Therefore there was about 50 μs between triggered interactions. It took about 35 μs to digitize an event. This time was extended to 50 μs to reduce electronic noise levels in the SMD amplifiers. Therefore, the total digitization time was about equal to the time between triggered interactions, leading to about 50% deadtime.

Table **3.2**. E791 front end digitization systems.

system	DC muon	calorimeters, Čerenkov	SMD	PWC	CAMAC
digitizer	Phillips 10C6 TDC	LeCroy 4300B FERA ADC	Ohio State, Nanometric N339P and S710/810 latches	LeCroy 2731A latch	LeCroy 4448 latch 4508 PLU 2251 scaler
digitization	30 μs	30 μs	50 μs	4 μs	30 μs
# of channels	6304	554	15896	1088	80
word size in bits	16	16	8	16	1,8,16,24
on tape fraction	50%	27%	18%	3%	2%

3.3 The Data Acquisition System [26]

The data acquisition system (DA) is what differentiates E791 the most from the previous charm experiments conducted at TPL. It was designed to accept large bursts

of data at a faster rate than it could fully process them but made use of dead time in the beam delivery structure to process and record the data to memory in a continuous manner. The Fermilab Tevatron delivered beam during a 23 second spill, with a 34 second gap between spills. The "interspill" was needed to refill the Tevatron.

The DA is composed of three major components: memory buffers, event buffer interfaces and Exabyte tape drives. The general data flow path in the DA is shown on Figure 3.2. The whole DA exhibited a parallel architecture. The data flowed from the front end digitizers along parallel data buses into eight separate large memory buffers. Six VME crates working in parallel housed 54 processors that assembled and compacted the data received from the different digitizers. These processors also controlled 42 exabyte tape drives to which the data was sent in parallel. This parallel structure of the DA allowed 24,000 channels to be read out in 50 μs, such that approximately 9000 events were digitized per second during the spill. Making full use of the interspill dead time, the DA design allowed us to accumulate data on tape at a continuous rate of 9.6 Mbyte/s. The main characteristics of the DA are summarized in Table 3.3.

Table **3.3**. Characteristics of the Data Acquisition System

Digitization time	50 μs
Total memory size	640 Megabytes
CPU	54 ACP II's
Event length	$\approx$ 1.2 kbytes
Acquisition rate	26 Megabytes/s (spill)
	9.6 Megabyte/s (continuous)
	$\approx$ 9000 events/s
output	42 parallel Exabyte tape drives

3.3.1 The memory buffers

The data arriving at the DA was generated by the various detector digitizing systems described earlier. Each digitizer produced data segments, the portion of digitized information corresponding to a specific detector for each event. The data segments were stored into one of the eight event FIFO (First In, First Out) buffers (EFB's). The eight EFB's provided a total of 640 Mbytes of memory, enough to store one spill of data. This allowed the rest of the DA system to be active during both the spill and interspill. Five of these buffers were used to store data from the fastbus TDC's, which digitized the data from the drift chambers and the muon wall.

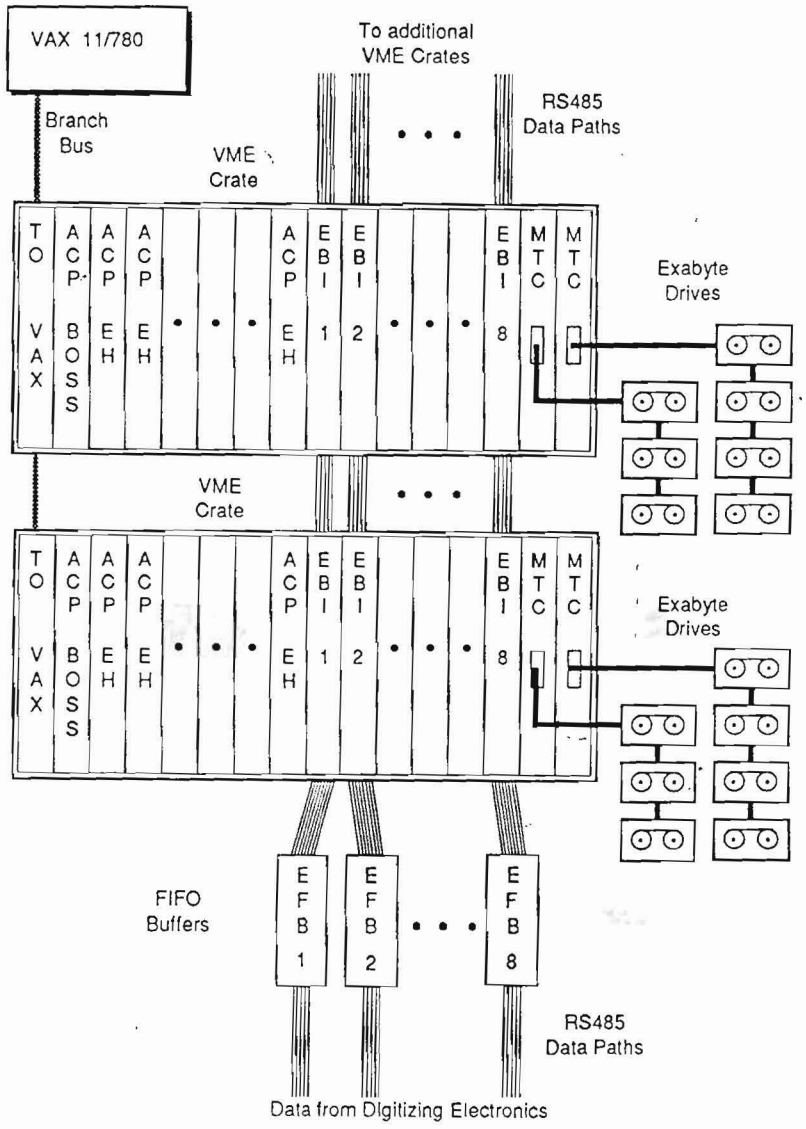

Figure 3.2. Flow of data from the digitizers through the data acquisition system.

The sixth FIFO buffer held the SMD data. The last two buffers held data from the calorimeters, the PWC's, the Čerenkov counters and the scintillation counters from the trigger system. If one of these buffers was nearly full, the trigger logic was disabled (*i.e.*, no new events were accepted) until some of the data had been processed.

Every event was assigned a four-bit event synchronization number (ESN) by the trigger logic which was attached to the first word of each data segment. The first 32-bit word of data from each segment also contained the word count for that event.

3.3.2 The interface

The heart of the DA was the interface between the temporary storage unit (buffers) and the tape drives. Several different functions were performed by units of CPU designed at Fermilab called ACP II's (Advanced Computing Project). Although small enough to fit in a single slot of a VME crate, each ACP II has the equivalent CPU power of 17 Vax-780!

The ACP II processors performed different tasks and were referred to as event buffer interfaces (EBI's) or "grabbers" and event handlers (EH) or "munchers" according to their specific functions. Each VME crate held eight EBI's, one for every memory buffer so that every CPU had access to the output data path from every buffer. The grabber's role was to read event segments from the EFB's and reconstruct the full event information, checking that the event synchronisation number matched for each segment. The data was formatted and compressed by the munchers before being passed to the tape drives. All the different functions performed by the interface were coordinated by a module of CPU called the boss.

3.3.3 The tape drives

Two magnetic tape controllers (MTC) housed in each of the VME crates controlled a series of seven tape drives, to which the data was written in parallel. The MTC supervised loading, initializing and writing the tapes. Exabyte tape drives and 8 mm video tapes were selected for their relatively low cost and high data writing rate.

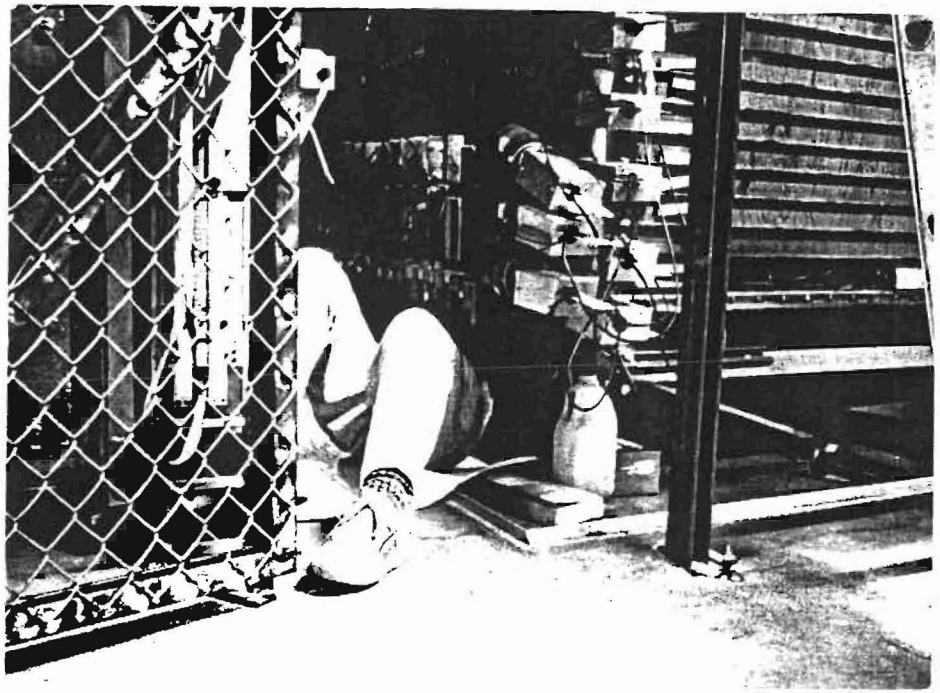

Spring 1991: Repairing an oil leak under the calorimeter before the run

4. Electron Identification

4.1 Introduction

Efficient electron identification and minimum pion misidentification in the data are essential to the form factor analysis involving semileptonic decays. Reducing the amount of contamination from background events leads to more accuracy when extracting the value of the form factors by performing a five-dimensional fit to the data. Moreover, good electron identification over the widest possible range of momenta enhances the precision achieved when performing the fit.

This chapter describes the electron identification algorithm used in the E791 code and evaluates its performance using samples of known electrons and pions from E791 data. The electron-pion discriminating power of this algorithm is compared to the algorithm used by E691. [27, 28, 29] The electron-pion discrimination was significantly improved in E791 for momenta less than 12 GeV/c and slightly improved for momenta greater than 20 GeV/c. In the 12 to 20 GeV/c momentum range, it is about the same as E691.

4.2 Shower Reconstruction

The shower reconstruction algorithm is basically the same as that used by E691. [30]It finds clusters of energy in each of the three views (U, V and Y), associates triplets of clusters (*i.e.*, one cluster from each view) with charged tracks or neutral shower candidates, and uses a least-squares fitting technique (stepwise regression) to find the optimal set of candidate shower energies. More specifically, the following quantity is minimized:

$$\chi^2 \equiv \sum_{\text{cluster } i} \left(e_i - \sum_{\text{candidate } j} \alpha_{ij}\epsilon_j \right)^2 w_i$$

where e_i is the energy measured in cluster i; w_i is the weight for the energy measurement e_i ($w_i = 1/\sigma_i^2$); ϵ_j is the energy candidate j would deposit in the SLIC (ϵ_j are the parameters to be determined by the fit); and α_{ij} is a position-dependent energy correction factor which includes an optical attenuation factor and corrections for physical and optical shower leakage between the right and left Y views. The goal is to find the set of candidates with energy ϵ_j which minimizes the above χ^2. The stepwise regression technique is a method in which candidates are added or subtracted one at a time without having to invert the entire correlation matrix for each step. The conditions under which candidates are added or dropped are described in reference 30.

As well as reconstructing charged and neutral shower candidates in the SLIC and hadrometer, the reconstruction code calculates electron probabilities for charged tracks, identifies e^+e^- pairs from converted photons, and finds π^0 candidates.

4.3 Electron probability

For each charged track, an electron probability is calculated based on the following measured properties of the charged track and the electromagnetic shower associated with it in the SLIC:

- $(E_{SLIC} - p)/\sigma_E$ where p is the momentum of the charged track as measured by the tracking system, E_{SLIC} is the energy in the SLIC associated with the track, and σ_E is the error on the measured energy;
- SECMOM: the second moment of the SLIC energy distribution in the U or V channels, whichever is smaller;
- Δx and Δy: the distance between the centroid of the SLIC shower and the intersection of the charged track with the SLIC, in the x and y directions, respectively;
- E_{had}: the hadrometer energy associated with the charged track.

For each of the above quantities, the probabilities that a real electron and a real pion take on a particular value are determined using electrons from photon conversions and pions from K_s^0 decays in the E791 data. It is assumed that each of the above quantities is independent of the others so that the total probability can be calculated as a simple product of the individual probabilities. The electron probability EMPROB is the probability that, in a beam with *equal* numbers of electrons and pions, the identification of a particle as an electron will be correct:

$$\begin{aligned} \text{EMPROB} &= 100 \times \frac{\prod_i f_i^e}{\prod_i f_i^\pi + \prod_i f_i^e} \\ &= 100 \times \frac{1}{1 + \prod_i (f_i^e / f_i^\pi)} \end{aligned}$$

In the above expression, each product is over the quantities used to discriminate electrons from pions, and f_i^e and f_i^π are the fractions of real electrons and pions, respectively, for which quantity i lies in a particular (narrow) range.

In the next section, the selection of samples of electrons and pions in the E791 data is discussed. Situations in which some or all of the variables are not available to be used for e/π discrimination are described. Finally, the measured electron identification efficiency and the pion misidentification probability in E791 data is presented and the E791 algorithm is compared to that used in E691.

4.4 The Electron Sample

For this study, charged tracks are used only if they were detected in the SMD planes and the first two drift chamber modules, D1 and D2. These tracks were also

required to point into the active volume of the SLIC. A sample of electrons from photoconversions was obtained by first selecting oppositely-charged pairs of tracks with a small amount of transverse momentum relative to the total momentum of the two tracks. [27]That is, a quantity PPSQ was defined as

$$\text{PPSQ} = \sum_{i=1,2} \frac{(\vec{p}_i \times \vec{p}_{tot})^2}{|\vec{p}_{tot}|^2}$$

where $\vec{p}_1$ and $\vec{p}_2$ are the momenta of the two oppositely charged tracks and $\vec{p}_{tot} = \vec{p}_1 + \vec{p}_2$. This variable is related to, but gives better separation from background than, the invariant mass of the pair of tracks or the angle between the two tracks. If either of the two tracks had EMPROB> 90, then the other track was included in the electron sample.* The PPSQ distribution is shown for the range 10^{-8} <PPSQ< 2×10^{-3} $(\text{GeV/c})^2$ in Figure 4.1 †. The photoconversion peak in the region PPSQ< 4×10^{-5} $(\text{GeV/c})^2$ (the first two bins in the histogram) is clear. On a tape with 361,000 transverse energy triggers, 11,449 candidate electrons were found with PPSQ< 4×10^{-5} $(\text{GeV/c})^2$ and $E_{SLIC} > 0$.

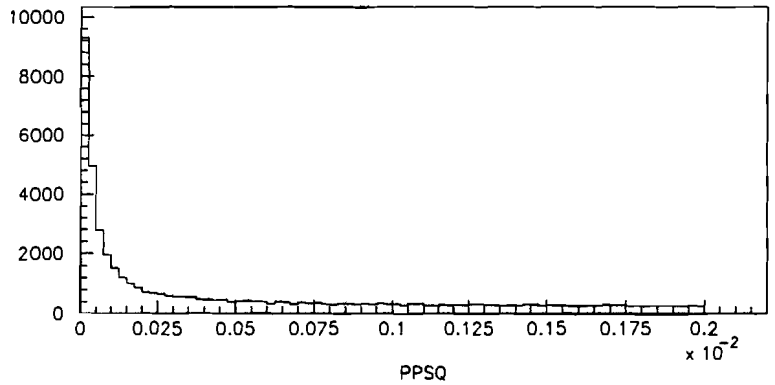

Figure 4.1 Distribution of PPSQ (in $(\text{GeV/c})^2$ for pairs of oppositely charged tracks in which at least one track is identified as an electron. See text for definition of PPSQ. If one track is identified as an electron and PPSQ for the pair is less than 4×10^{-5} $(\text{GeV/c})^2$ (first two bins), the other track is selected as an electron candidate.

The pion contamination in this sample is due to an electron and an oppositely-charged pion accidently having a small PPSQ. To determine the *shape* of the PPSQ distribution for the pion contamination under the photoconversion peak, a background sample was selected by requiring two oppositely charged tracks to each have gone through the SMD's, D1 and D2, to be pointing into the active region of the SLIC and to have EMPROB< 5 (*i.e., not* an electron). With this sample, it was determined that the PPSQ distribution above 10^{-8} $(\text{GeV/c})^2$ is flat at least out to 2×10^{-3}.

Once it was determined that the PPSQ distribution for the background was flat, the tail of the PPSQ distribution for electron candidates (PPSQ values between 1×10^{-3} and 2×10^{-3} $(\text{GeV/c})^2$, or the right half of the histogram in Figure 4.1) could be used to determine the EMPROB distribution of the contamination under the photoconversion peak. This will be described in more detail in a later section. The pion contamination in the electron sample was estimated for six momentum regions and is summarized in Table 4.1. By using the tail of the PPSQ distribution, these backgrounds were taken into account exactly.

Table 4.1 Fraction of the electron sample which is estimated to be due to pion contamination for different momentum ranges.

momentum	$\pi^{\pm}$ contamination
0 - 6 GeV/c	$(1.8 \pm 0.6)\%$
6 - 9 GeV/c	$(1.9 \pm 0.9)\%$
9 - 12 GeV/c	$(4.0 \pm 1.8)\%$
12 - 15 GeV/c	$(4.7 \pm 2.8)\%$
15 - 20 GeV/c	$(7.0 \pm 3.4)\%$
> 20 GeV/c	$(9.6 \pm 3.6)\%$

4.5 The Pion Sample

A pion sample was obtained by searching for the decay $K^0_s \rightarrow \pi^+\pi^-$ for K^0_s decays in the target/SMD region using the following selection criteria:

- at least two vertices in the event;
- a secondary vertex satisfying the following criteria:
  a) two oppositely-charged tracks having passed through the SMD's, D1, and D2, and pointing to the active region of the SLIC;
  b) vertex z-position at least 800 μm from the center of the nearest target and at least 1500 μm from the center of the interaction counter;

* Note that one or both of the tracks can end up in the electron sample.

† The region PPSQ< 10^{-8} is dominated by pairs of charged tracks which share hits in the SMD planes. Since the background in this region is very difficult to estimate, we elimate these photoconversion candidates.

c) vertex z-position between -8.1 cm and 28.0 cm;

d) significance of separation of primary and secondary vertex at least 6;

- net momentum of the charged tracks perpendicular to the direction of the parent particle as determined by the position of the primary and secondary vertices less than 100 MeV;
- momentum asymmetry defined as $|p_1 - p_2|/(p_1 + p_2)$ less than 0.65;
- invariant mass of the pair of tracks between 0.490 and 0.510 $(GeV/c)^2$.

A pion candidate was rejected if it was consistent with forming an e^+e^- pair from a photoconversion with any oppositely-charged track in the event. A total of 85,000 $\pi^+\pi^-$ pairs in the K^0_s peak were extracted. The two-particle invariant mass distribution in shown in Figure 4.2. The wings of the invariant mass distribution were used to take into account electron contamination in the candidate pion sample.

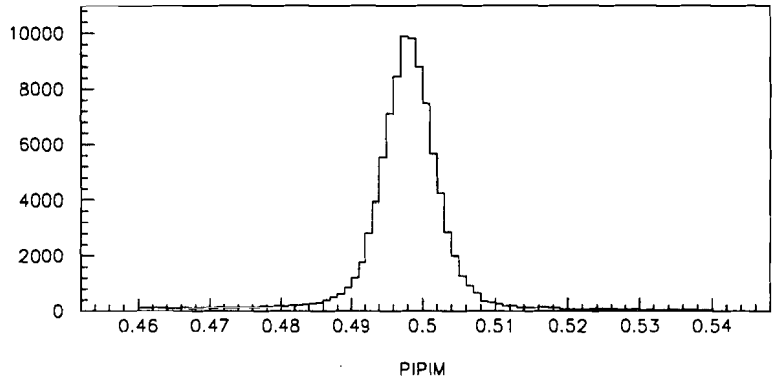

Figure 4.2 Invariant mass distribution for pairs of oppositely charged tracks satisfying the criteria described in the text to select K^0_s candidates. The horizontal axis corresponds to the invariant mass of the $\pi^+\pi^-$ pair in GeV/c^2.

4.6 Tracks with $E_{SLIC} = 0$

When no electromagnetic shower is associated with a charged track, the quantities used to discriminate electrons from pions cannot be calculated. A charged track which extrapolates into the active volume of the SLIC might have no energy associated with it for two reasons:

- It could be a minimum-ionizing particle such as a pion for which the deposited energy is not sufficient to pass the threshold criteria in the shower reconstruction code;

- Two tracks may be so close together in space (at the calorimeter) that they are both consistent with having produced the same shower. The shower is associated with the track whose projection is closest to the shower centroid. The other track will have no associated energy.

Using the samples of electrons and pions selected as described above, the fraction of events for which $E_{SLIC} = 0$ was determined as a function of momentum.* Table 4.2 lists the fraction of electrons and pions for which E_{SLIC} is *greater* than zero, and the ratio of the probability that $E_{SLIC} > 0$ for a pion to that for an electron. For E691 data, this ratio varied between about 0.18 and 0.24. A significantly higher fraction of pions have SLIC energy associated with them in E791 compared to E691. This could be due to the fact that E791 events are more crowded than E691 events so that pions are more likely to have energy from other tracks or showers (hitting the same strips) associated with them.

Table 4.2 Fraction of tracks with $E_{SLIC} > 0$ as a function of track momentum.

momentum	Fraction of tracks with $E_{SLIC} > 0$ electrons	pions	pions/electrons
0 - 6 GeV/c	95.0%	50.0%	0.53
6 - 9 GeV/c	95.1%	63.0%	0.66
9 - 12 GeV/c	96.7%	67.3%	0.71
12 - 15 GeV/c	95.1%	70.0%	0.70
15 - 20 GeV/c	95.0%	72.7%	0.77
>20 GeV/c	96.3%	79.3%	0.82

4.7 Special cases for SECMOM and E_{had}

In the central region of the calorimeter, each channel of the SLIC is read out with a single photomultiplier tube. In the outer regions of the SLIC, where the particle density is lower, adjacent pairs of channels are read out with a single photomultiplier tube. Therefore, the distribution of SECMOM (the second moment, or transverse width, of the energy distribution) has a higher mean and width for double-channel readout than for single-channel readout. Therefore, the variable SECMOM was treated separately for single-channel and double-channel readout.

* All of the electron and pion candidates were required to point to the active region of the SLIC.

The variable E_{had} (energy in the hadrometer associated with the charged track) provides discrimination against pions. In order to keep the electron efficiency as high as possible while still providing some pion rejection, E_{had} was used only if the hadrometer was not "congested" in the region around the charged track (*i.e.*, if there were no nearby tracks or tracks projecting into the same hadrometer strip).

4.8 Distributions of Discriminating Variables for Electrons and Pions

Figures 4.3 and 4.4 show the distributions for the discrimination variables $(E_{SLIC}-p)/\sigma_E$, E_{had}, SECMOM (for single-channel and double-channel readout separately), Δx and Δy, for electron and pions, respectively. The distributions are shown for the 9 to 12 GeV/c momentum range, as an example. These distributions are used to determine f_i^e and f_i^π in the calculation of EMPROB (see section 4.3) for the six momentum ranges listed in Tables 4.1 and 4.2 (0-6 GeV/c, 6-9 GeV/c, 9-12 GeV/c, 12-15 GeV/c, 15-20 GeV/c and above 20 GeV/c).

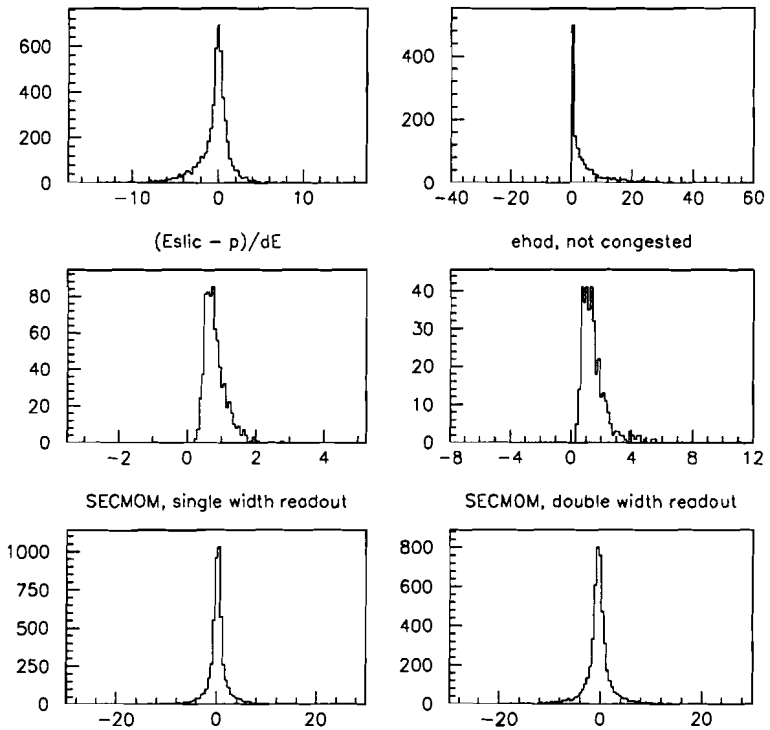

Figure 4.3 Distributions for the discrimination variables $(E_{SLIC}-p)/\sigma_E$, E_{had}, SECMOM (for single-channel and double-channel readout separately), Δx and Δy. The distributions are shown for electrons from photoconversions in the E791 data for the 9 to 12 GeV/c momentum range.

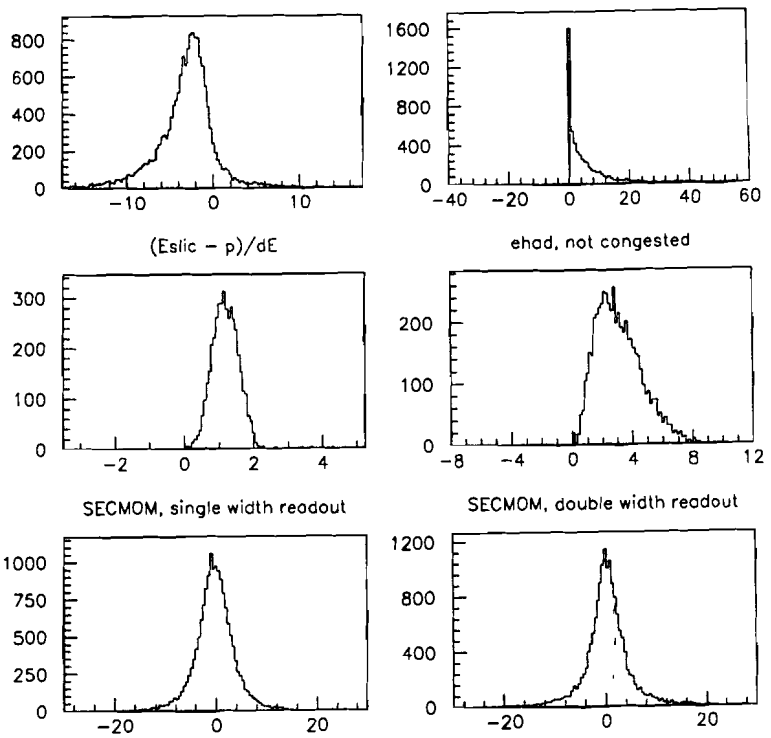

Figure 4.4 Distributions for the discrimination variables $(E_{SLIC}-p)/\sigma_E$, E_{had}, SECMOM (for single-channel and double-channel readout separately), Δx and Δy. The distributions are shown for pions from K_s^0 decays in the E791 data for the 9 to 12 GeV/c momentum range.

For the purposes of determining f_i, the distributions are stored in 25 bins for each variable, for each momentum range, with the first and last bin corresponding to the underflow and overflow entries, respectively. The distributions are all normalized so that the sum over all the bins is equal to 1.

In Figures 4.3 and 4.4, the distributions are *not* normalized and are shown for 125 bins so that one can see any structure in the distribution which is lost in the underflow and overflow bins when calculating EMPROB. Explicitly, the sum of the first 51 bins in the figures is put in the underflow bin for f_i; the sum of the last 51 bins is put in the overflow for f_i; the central 23 bins in the figure correspond to the central 23 bins stored for this particular variable.

4.9 Correlations Between Discrimination Variables

For a fixed set of discrimination variables, EMPROB will provide the best e/π discrimination possible *unless* there are correlations between the discrimination variables for electrons or for pions. In that case, discriminant analysis or binary decision trees can provide better e/π discrimination.

Scatterplots were made of each variable against all other variables to check for correlations. Some illustrative scatterplots are shown in Figures 4.5 and 4.6 for electrons and pions, respectively, for the 9 to 12 GeV/c momentum range. No correlations are observed. That is, the distribution of a particular variable is the same for different slices of a second variable. Therefore, we would not benefit from using discriminant analysis or binary decision trees.

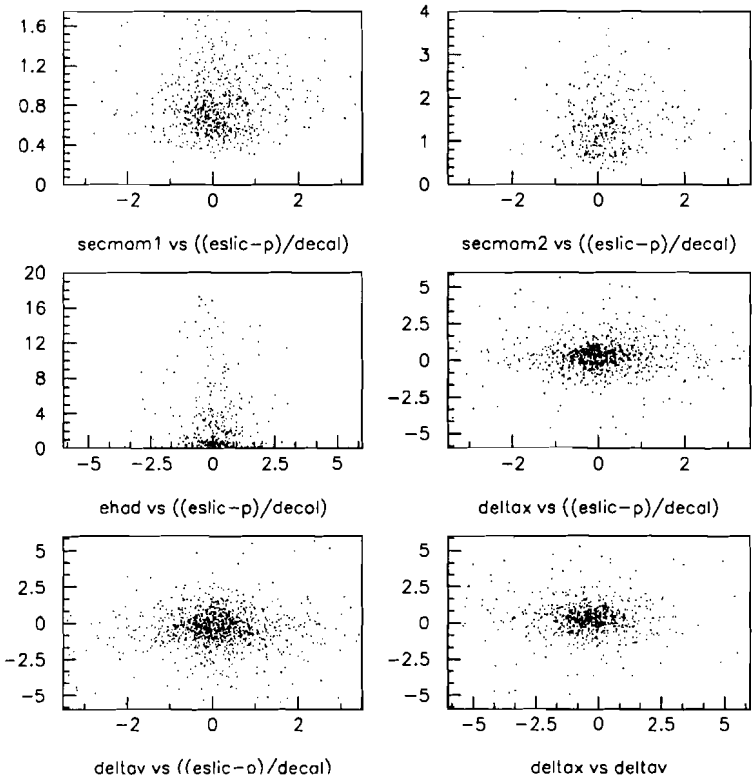

Figure 4.5 A subset of scatterplots of one discrimination variable versus another, for electrons from E791 data, to illustrate that there are no significant correlations between the variables; *i.e.*, the distribution of one variable will not change if we consider slices in the other variable.

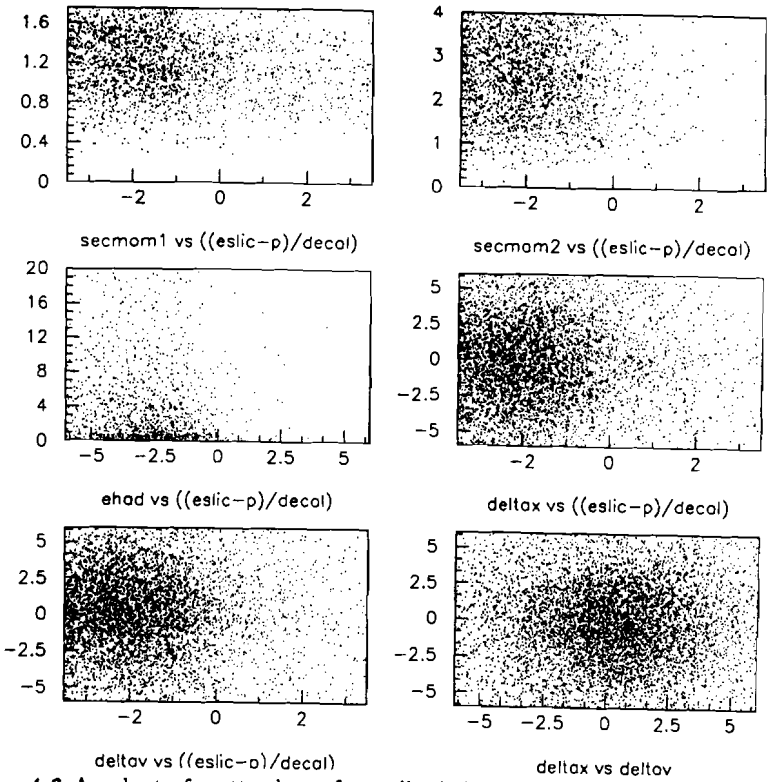

Figure 4.6 A subset of scatterplots of one discrimination variable versus another, for pions from **E791 data**, to illustrate that there are no significant correlations between the variables; *i.e.*, the distribution of one variable will not change if we consider slices in the other variable.

4.10 Electron Identification Efficiency and Pion Misidentification Probability

Using the selected electrons from photoconversions and pions from K^0_s decay, with $E_{SLIC} > 0$, we determined the EMPROB distribution for electrons and pions, respectively. The EMPROB distributions are shown in Figure 4.7(a) for electron candidates and in Figure 4.8(a) for pion candidates, for the 9 to 12 GeV/c momentum range.

Contamination of pions in the electron sample was taken into account by subtracting the EMPROB distribution for candidates in the tail of the PPSQ distribution (1×10^{-3} to 2×10^{-3} (GeV/c)^2), normalized assuming the background has a flat PPSQ distribution. Figure 4.7(b) shows the EMPROB distribution for the PPSQ tail and Figure 4.7(c) shows the background-subtracted EMPROB distribution (Figure 4.7(b) subtracted from 4.7(a)) for electrons.

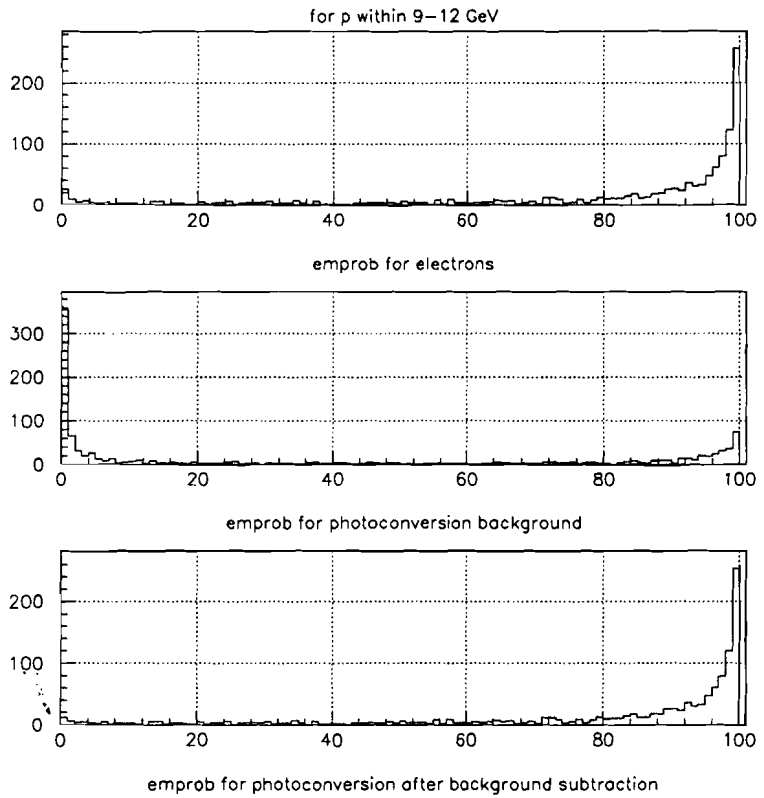

Figure 4.7 The EMPROB distribution for (a) electron candidates for PPSQ< 4×10^{-5} $(GeV/c)^2$ (see Figure 4.1) and (b) background candidates from the PPSQ tail (1×10^{-3} < PPSQ< 2×10^{-3} $(GeV/c)^2$.). The background-subtracted distribution [(b) subtracted from (a) after normalization] is shown in (c). All distributions correspond to the 9 to 12 GeV/c momentum range.

Similarly, the contamination of electrons in the pion sample was taken into account by subtracting the EMPROB distribution for candidates in the wings of the two-particle invariant mass distribution (460 to 480 MeV and 520 to 540 MeV), normalized assuming the background distribution is flat. Figure 4.8(b) shows the EMPROB distribution for the wings and Figure 4.8(c) shows the background-subtracted EMPROB distribution (Figure 4.8(b) subtracted from 8(a)) for pions.

The background-subtracted EMPROB distributions were then used to determine the probability that an electron or pion will have EMPROB greater than a certain minimum value (when $E_{SLIC} > 0$) for each momentum range. These probabilities were then multiplied by the fraction of electron or pion tracks which have $E_{SLIC} > 0$

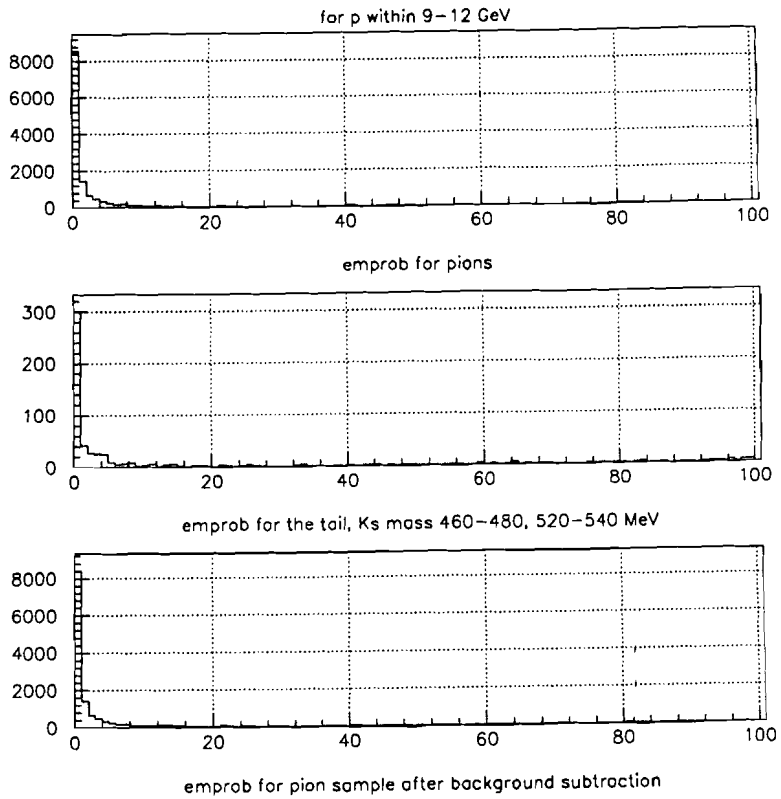

Figure 4.8 The EMPROB distribution for (a) pion candidates from a pair of charged tracks with mass in the K^0_s peak (490 to 510 MeV) (see Figure 4.2) and (b) charged particles in the wings of the K^0_s peak (460 to 480 MeV and 520 to 540 MeV). The background-subtracted distribution [(b) subtracted from (a) after normalization] is shown in (c). All distributions correspond to the 9 to 12 GeV/c momentum range.

(see Table 4.2) to get the final electron identification efficiencies and pion misidentification probabilities. Figure 4.9 summarizes the e/π discriminating power of EMPROB with a plot of electron identification efficiency versus pion misidentification probability for different minimum EMPROB values, for each momentum range. The dot in the lower left-hand corner of each plot corresponds to the fraction of electrons or pions with an EMPROB value greater than 100; therefore, the electron identification efficiency and pion misidentification probability are both zero. The next dot corresponds to the fraction of electrons and pions with an EMPROB value greater than 99. Each consecutive dot corresponds to a minimum EMPROB value one unit smaller.

Note that the position of this curve (and hence the e/π discriminating power of EMPROB) does *not* depend on the apriori probabilities of electrons and pions

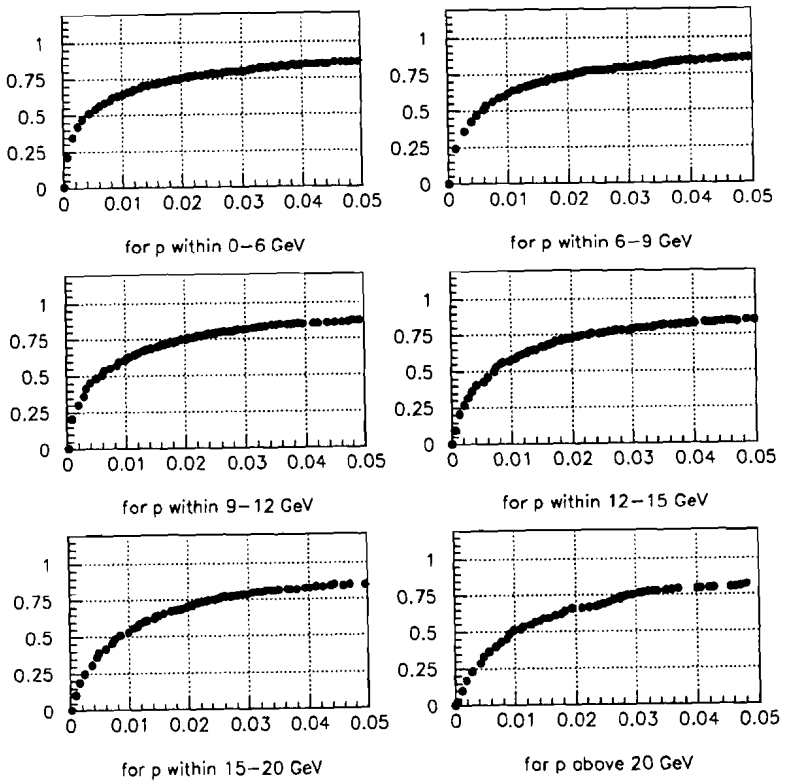

Figure 4.9 e/π discrimination power in the E791 code. Electron identification efficiency is plotted versus pion misidentification probability as a function of minimum value of EMPROB, for six momentum ranges. The efficiencies and misidentification probabilities include the probability that $E_{SLIC} > 0$ from Table 4.2.

assumed in the calculation of EMPROB. These apriori probabilities are dependent on the selection criteria applied to an event before a track is selected and hence are analysis-dependent. The minimum value of EMPROB which should be used for a particular analysis depends on how much one is willing to give up on electron efficiency to get the necessary pion rejection.

Table 4.3 lists the minimum value of EMPROB which will give a pion misidentification probability of 0.5%, 1.0% and 2.0% for each momentum range. A list of the corresponding electron identification efficiencies is also provided.

4.11 Comparison with E691 EMPROB

The algorithm for e/π separation used in the E791 code is basically the same as that used by E691 with the following differences.

Table 4.3 The minimum value of EMPROB which will give a pion misidentification probability P^{π}_{misid} of 0.5%, 1.0% and 2.0% for each momentum range. The corresponding electron identification efficiencies ϵ_e are also listed.

P^{π}_{misid}	0.5%		1.0%		2.0%	
p (GeV/c)	minimum EMPROB	ϵ_e	minimum EMPROB	ϵ_e	minimum EMPROB	ϵ_e
0-6	94	54%	88	65%	74	75%
6-9	96	47%	90	62%	75	74%
9-12	94	48%	87	62%	71	76%
12-15	93	43%	86	58%	65	74%
15-20	94	39%	88	56%	73	70%
> 20	94	33%	88	50%	77	65%

- For E691, only $(E_{SLIC}-p)/\sigma_E$ and SECMOM were used for momenta less than 12 GeV/c. For momenta above 12 GeV/c, these variables plus the hadrometer energy and RSQD, the square of the distance between the centroid of the SLIC shower and the intersection of the charged track with the SLIC (not Δx and Δy separately), were used.
- Only three momentum ranges were used (3 to 6 GeV/c, 6 to 12 GeV/c, and above 12 GeV/c).
- For E691, the distribution for each variable was binned into a small number of bins (typically four to six) rather than the large number of bins (25) used for E791.
- In E691, for momenta above 12 GeV/c, the RSQD probabilities were determined separately for three different categories of tracks depending on their momentum and distance from the center of the calorimeter.

In reference 27, the electron identification efficiency and pion misidentification probabilities are given for electrons and pions with momentum greater than 12 GeV/c in E691 data.* The values were found using samples of electrons from photoconversions and pions from K^0_s decay and are given in Table 4.4 below.

Our sample of electrons from photoconversions and pions from K^0_s decays from E791 data were also used to measure the e/π discriminating power of EMPROB

* Although it is not explicitly stated in reference 27, we assume that these efficiencies take into account the probability that the track does not have any SLIC energy associated with it.

Table 4.4 Electron identification efficiency and pion misidentification probability determined from the E691 data for momentum above 12 GeV/c (from reference 27).

minimum EMPROB	$e^{\pm}$ identification efficiency	$\pi^{\pm}$ misidentification probability
90.0	82%	1.2%
96.0	76%	0.69%
98.0	71%	0.44%
99.0	64%	0.36%
99.2	61%	0.30%
99.4	57%	0.25%
99.6	51%	0.19%
99.8	41%	0.098%

as calculated in the E691 code. Figure 4.10 shows a plot of electron identification efficiency versus pion misidentification probability as a function of the minimum EMPROB value for the usual six momentum ranges. For the momentum range above 12 GeV/c, our measurements are not in agreement with the numbers listed in Table 4.4 from reference 27. This is probably due to the fact that our measurements were made with E791 data and those in Table 4.4 were made with the lower-multiplicity E691 data.

For momenta less than 12 GeV/c, we see large jumps in the electron efficiency. This is due to the coarse binning used for the separation variables in the calculation of EMPROB in the E691 code. Comparing Figure 4.10 (E691 EMPROB) to Figure 4.9 (E791 EMPROB), we see that for momenta below 12 GeV/c the new E791 EMPROB provides much better e/π discriminating power compared to the old E691 EMPROB. Above 20 GeV/c, the new EMPROB is slightly better. In the range 12 to 20 GeV/c, the old EMPROB appears to be slightly better for very high EMPROB cuts. However, the statistical uncertainty on the pion misidentification probability in this range is very significant for the old EMPROB since that study was made on a much smaller sample of pions.

4.12 Conclusions

A new calculation of EMPROB, the variable used for discriminating electrons from pions, was implemented in the E791 code. The basic algorithm is the same as that developed and used by E691 but each discrimination variable is binned more

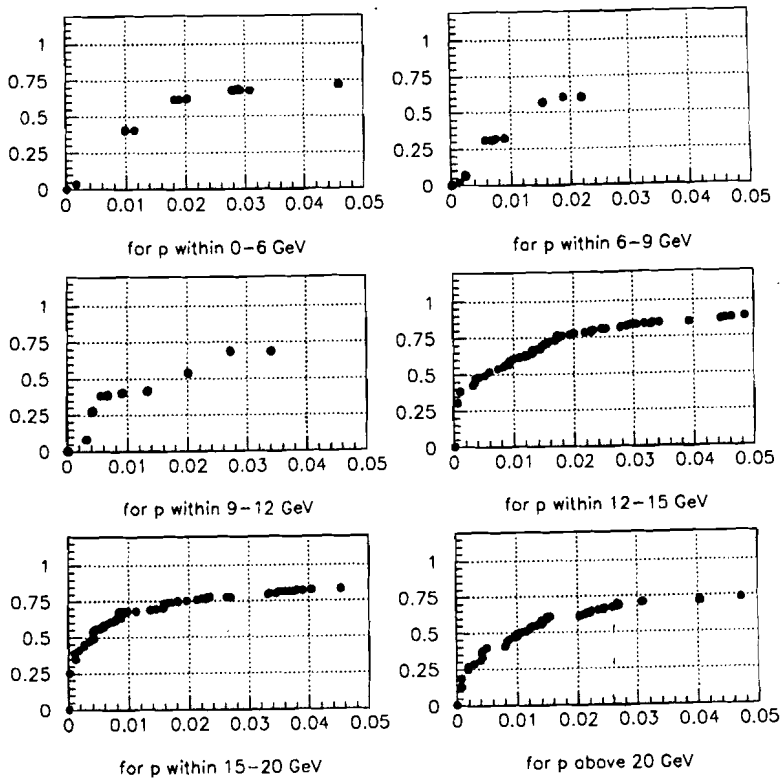

Figure 4.10 e/π discrimination power using EMPROB as calculated in the E691 code. Electron identification efficiency is plotted versus pion misidentification probability as a function of minimum value of EMPROB, for six momentum ranges.

finely (so that we effectively use a continuous probability distribution) and all available discrimination variables are used for all momentum ranges. In addition, we consider six momentum ranges separately; E691 considered only three.

The e/π discrimination power was evaluated for the old E691 EMPROB (see Figure 4.10) and the new E791 EMPROB (see Figure 4.9) using samples of known electrons and pions from the E791 data. The e/π separation below 12 GeV/c is now at least as good as above 12 GeV/c. The E691 semileptonic-decay analysis for $D \rightarrow K^* e\nu$ identified electrons with momentum above 12 GeV/c only.

5. Event Selection

5.1 Introduction

The E791 trigger was primarily designed to tag inelastic interactions of the beam pion with a nucleon in one of the target foils. This approach allowed us to accumulate 20 billion events with little bias for studies of the decay properties of charmed mesons and baryons. Charm identification is done offline. Given the size of our data sample, any attempt at extracting specific decay modes from the bulk of the 24,000 8-mm tapes is bound to be challenging. This motivated the design of a multi-step strategy to reduce the amount of data, while retaining a substantial fraction of the charm content of our sample. The various steps, described in detail below, are:

- The filter is designed to retain most charm decays while reducing the bulk of the data.
- The stripping code looks for all reconstructable charm decay modes.
- The substripping code selects specific decay channels with more stringent cuts intended for physics analysis.

The main strategy in looking for charmed hadron decays is to select events having a decay vertex well-separated from the production vertex. This is possible due to the fact that charmed mesons were produced in our detector in the $20 - 200$ GeV/c momentum range and have lifetimes between 0.2 and 1 picosecond. With $\gamma = E/m \sim \frac{20-200\ GeV}{2\ GeV} \sim 10 - 100$, and $\beta \sim 1$, the mean decay distance $\langle l \rangle \approx \gamma\beta c\tau$ is of the order of a few millimeters. The target foils were placed roughly 1.5 cm apart, and were approximately 1.5 mm thick. Therefore, charmed particles usually decayed outside the target material, and could be distinguished because the separation between the primary and secondary vertices along the beam direction is much greater than the resolution on that separation, which is of the order of 400 μm. The event selection steps are described below, from the initial trigger requirements to the cuts used at the filtering, stripping, substripping and final physics analysis levels. For this analysis, data events and Monte Carlo simulated events were passed through the same set of selection criteria.

5.2 The trigger

To enhance the charm content of our data sample, the online trigger selected events having at least four charged tracks downstream of the target and a minimum amount of transverse energy in the calorimeter. More detail has been provided in chapter 3.

5.3 Reconstruction and filtering

For each event, all charged tracks were reconstructed and used to form a primary vertex and possible secondary vertices. This information was used to decide whether or not to retain the event and analyze remaining detector subsystems. This decision is referred to as the filter. The reconstruction and filtering represented the bulk of the computing effort in data analysis and was performed at four different computing farms located at the University of Mississippi, Kansas State University, Fermilab and CBPF in Rio de Janeiro.

The primary and secondary vertices were reconstructed as follows:

- The primary vertex is found by looking for an intercept between the beam pion track and other tracks at one of the target foil locations.
- Secondary vertices are formed by two or more tracks intersecting downstream of the primary. The separation between the primary and a secondary vertex along the beam direction, measured in units of uncertainty on the separation (called SDZ), was calculated for each secondary vertex. It is defined as SDZ $= \frac{\Delta z}{\sqrt{\sigma^2_{sec} + \sigma^2_{prim}}}$. (The separation transverse to the beam axis is insignificant in comparison.)

To pass the filter requirements, an event had to contain at least one secondary vertex with SDZ > 4 .

5.4 The stripping

The stripping procedure was intended to provide reduced samples of events selected for specific physics analyses. Rather loose cuts were applied in each strip to minimize the bias. Events corresponding to the $D^+ \to \bar{K}^{*0} l^+ \nu_l$ decay mode were selected by the semileptonic 3-prong stripping code. The semileptonic strip was designed to select most semileptonic decays based primarily on lepton identification. Electrons were selected on the basis of the variable EMPROB (described in chapter 4). If a muon wall hit position matched the projected charged track position (within a certain window to allow for multiple scattering and counter width), the track was included in the muon list. The secondary 3-prong vertex was also required to have SDZ> 5 .

5.5 The substrip

The substrip used for this analysis selects a sample rich in $D^+ \to \bar{K}^{*0} l^+ \nu_l$ decays. It relies primarily on particle identification both for the kaon and the lepton. The cuts are:

- The SDZ cut for the 3-prong-vertex was 12 .

- The vertex $\chi^2/d.o.f.$ must be less than 6.0 .
- Each of the three tracks must have $\chi^2/d.o.f. < 6.0$.
- One of the tracks must be identified as a kaon with Čerenkov kaon probability > 0.4 (a priori value is 0.12.)
- One of the tracks must be identified as an electron with EMPROB >50 .

5.6 Signal Extraction

To select the $D^+ \rightarrow \bar{K}^{*0} l^+ \nu_l$ signal, we searched our data for events containing a 3-prong secondary vertex. We made sure that all selected 3-prong vertices satisfied each cut from the filter, strip and substrip levels specifically. That is, the event passed all selection criteria because of the selected 3-prong semileptonic vertex and not by another secondary vertex contained in the same event. Then more stringent cuts were applied on tracks and vertices as listed below:

- The SDZ for the 3-prong vertex was required to exceed 15.
- The three tracks should form a secondary vertex with a $\chi^2/d.o.f.$ less than 5.0 .
- Primary vertices were rejected if they were located in material downstream of the targets. We required $z_{primary} < -1$ cm, whereas the last target foil is located at about -2 cm.
- To eliminate events from secondary interactions, a cut was made on the z-location of the decay vertex. Vertices formed within 0.15 cm of the center of a target foil were rejected.
- The sum of the charges for the three tracks had to be ± 1.
- Each one of the charged tracks had to have a $\chi^2/d.o.f.$ less than 3.5 to reduce contributions from poorly reconstructed tracks.
- Each charged track must have been inconsistent with coming from the primary vertex. The contribution to the $\chi^2/d.o.f.$ of the primary vertex had to exceed 8. This cut is imposed to reject events where poor vertexing allowed a track belonging to the primary vertex to be included in a secondary vertex.

To help distinguish real vertices from fake vertices formed from random tracks not coming from the same parent particle or from incomplete reconstruction of the vertex, we looked at the impact parameter of the vector sum of the visible tracks with respect to the primary vertex, taking into account the possible contribution due to the undetected neutrino. The total momentum vector of the visible particles must point back to the primary vertex within kinematic and resolution limits. One can evaluate the maximum kinematically allowed displacement d_{max} by assuming that all the neutrino momentum is perpendicular to $\mathbf{p}_{vis} = \mathbf{p}_K + \mathbf{p}_\pi + \mathbf{p}_e$ as shown in

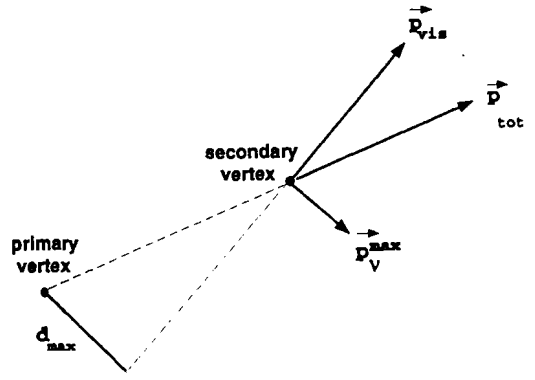

Figure 5.1. The maximum displacement from the line joining the primary and secondary vertex, assuming all neutrino momentum is perpendicular to the visible momentum vector.

Figure 5.1. One can determine $\mathbf{p}_\nu^{max}$, the neutrino momentum corresponding to the maximum displacement d_{max}, by using the D mass constraint:

$$m_D^2 = (p_{vis} + p_\nu^{max})^2 = m_{vis}^2 + 2\ E_{vis}\ E_\nu^{max}. \tag{5.1}$$

Since $E_\nu^{max} = p_\nu^{max}$ this reduces to

$$p_\nu^{max} = \frac{(m_D^2 - m_{vis}^2)}{2\ E_{vis}.} \tag{5.2}$$

With $\mathbf{p}_{total} = \mathbf{p}_\nu^{max} + \mathbf{p}_{vis}$, one obtains d_{max} from figure 5.1:

$$d_{max} = \frac{p_\nu^{max}}{p_{total}} \times \Delta r \tag{5.3}$$

where $\Delta r = |\ \mathbf{r}_{secondary} - \mathbf{r}_{primary}\ |$ is the separation between the primary and secondary vertices along the beam direction.

The distance of closest approach of the vector sum of the momenta of the visible particles (called d_{ip} is checked for consistency with the kinematically allowed distance d_{max}.

- In particular, only events for which $\frac{|d_{ip} - d_{max}|}{\sigma_{d_{ip}}} < 3.5$ are accepted. The resolution $\sigma_{d_{ip}}$ is generally of the order of 365μm while the average d_{max} is less than 20μm.

Finally, we required proper identification of the electron, pion and kaon among the three charged tracks.

- The charged kaon had to be positively identified in the Čerenkov counters. The Čerenkov kaon probability was required to exceed 0.4 for the kaon candidate. (The a priori value is 0.12, that is, one track out of eight is a kaon.)
- The Čerenkov pion probability for the pion candidate had to exceed 0.4. The pion a priori probability is 0.82 .
- Electrons were identified in the electromagnetic calorimeter by requiring that EMPROB be greater than 80.
- Electron candidates consistent with being a member of a photoconversion pair were eliminated by rejecting events where the electron candidate was a member of a pair of oppositely charged tracks with a very small tranverse momentum with respect to their momentum vector sum. We used the variable PPSQ described in chapter 4 and required that all such pairs satisfied PPSQ $> 2\times10^{-4}$.

Note that no explicit momentum cut was applied to the electron sample but geometric acceptance reduced the number of electrons found below 5 GeV/c. The momentum distribution for the electrons in the selected events is shown both for right-sign ($K^{\mp}\pi^{\pm}e^{\pm}$) and wrong-sign ($K^{\pm}\pi^{\mp}e^{\pm}$) events in Figure 5.2. Retaining events containing low momentum electrons will increase sensitivity for the kinematic variables $\cos\theta_l$ and q^2, as will be discussed in chapter 6.

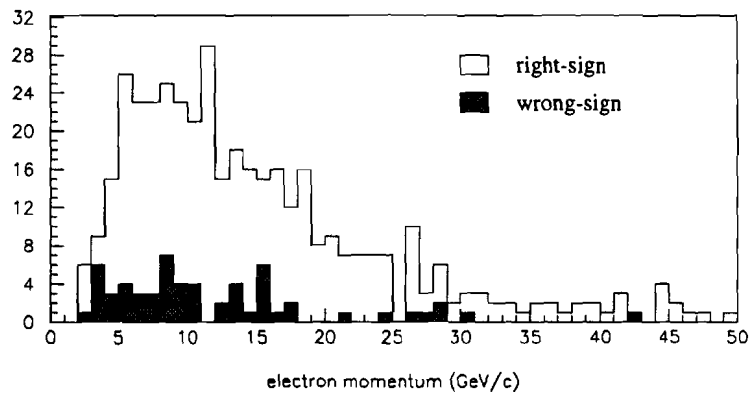

Figure 5.2. The electron momentum distribution for the right-sign and wrong-sign events after all other selection cuts. No cut on the electron momentum was applied in the selection procedure. There is an implicit geometric acceptance limitation at $\approx$ 5 GeV/c.

The $D^+ \rightarrow \bar{K}^{*0}e^+\nu_e$ signal (and its charge conjugate) was extracted by looking for events where the $\bar{K}^{*0}$ decays into $K^-\pi^+$. Note that the kaon charge is opposite to the electron charge. This formed our "right-sign" sample. Events in which the kaon and the electron have the same sign are called "wrong-sign" events. Backgrounds to the right-sign sample are of two kinds: non-charm background events (which can be monitored by wrong-sign events), and charmed backgrounds such as $D^+ \rightarrow K^-\pi^+\pi^+$ where a pion is misidentified as an electron. Eleven events consistent with $D^+ \rightarrow K^-\pi^+\pi^+$ were removed from the final right-sign sample after all other cuts. Contributions from $D^+ \rightarrow K^-\pi^+\pi^+\pi^0$ could be of comparable size but have not yet been studied extensively on this partial data sample. The effect of each cut on the signal was studied using Monte Carlo events. We used wrong-sign events from the data to simulate non-charm backgrounds. Cuts were tuned based on their effects on Monte Carlo signal events and wrong-sign data events. The effects on the signal-to-background ratio in the data of some of these cuts are shown in Figure 5.3 where each of the final cuts is added in turn. Cuts on $\chi^2/d.o.f.$ of the secondary vertex and tracks have already been applied, as well as the SDZ and kaon identification cuts.

The signal-to-background ratios in the $M_{K\pi}$ range of 0.84 to 0.96 GeV/c^2 and $m_{min}{}^{\star}$ range of 1.6 to 2.0 GeV/c^2 are shown in Table 5.1 after all cuts and after removing each cut. The fact that the signal-to-background improves with each cut demonstrates the effectiveness of each cut for some of the cuts described earlier.

The D mass cannot be fully calculated due to missing information on the neutrino, since the longitudinal neutrino momentum can only be reconstructed up to a quadratic ambiguity. The method used to extract the best estimate of the neutrino momentum will be discussed in detail in the next chapter. Even without knowing the full neutrino momentum, one can evaluate the minimum kinematically allowed mass m_{min}, defined as the invariant mass of the K, π, l, ν_l system, neglecting the component of the neutrino momentum along the direction of flight of the D:

$$m_{min} = \sqrt{m_{vis}^2 + p_T^2} + \sqrt{m_\nu^2 + p_T^2}$$

where p_T is the transverse momentum of the visible particles with respect to the D direction (as determined by the primary and secondary vertex positions) and m_{vis} is the invariant mass of the visible particles. Monte Carlo simulations such as the one displayed in Figure 5.4 show a sharp cusp in m_{min} at the mass of the D. Hence, one can reject events with values of m_{min} exceeding the mass of the D, after allowing for smearing due to detector resolution.

Figure 5.5 shows the m_{min} and $K\pi$ invariant mass distributions for decays with an electron in the final state. In Figure 5.5(a) and (b), the solid curve shows the right-sign events and the shaded area represents the wrong-sign events. To extract a clean signal, events are selected within a narrow window for m_{min} between 1.6 and 2.0 GeV/c^2. The invariant mass of the $K\pi$ system is shown in Figure 5.5(b) for these

$\star$ defined later in this section

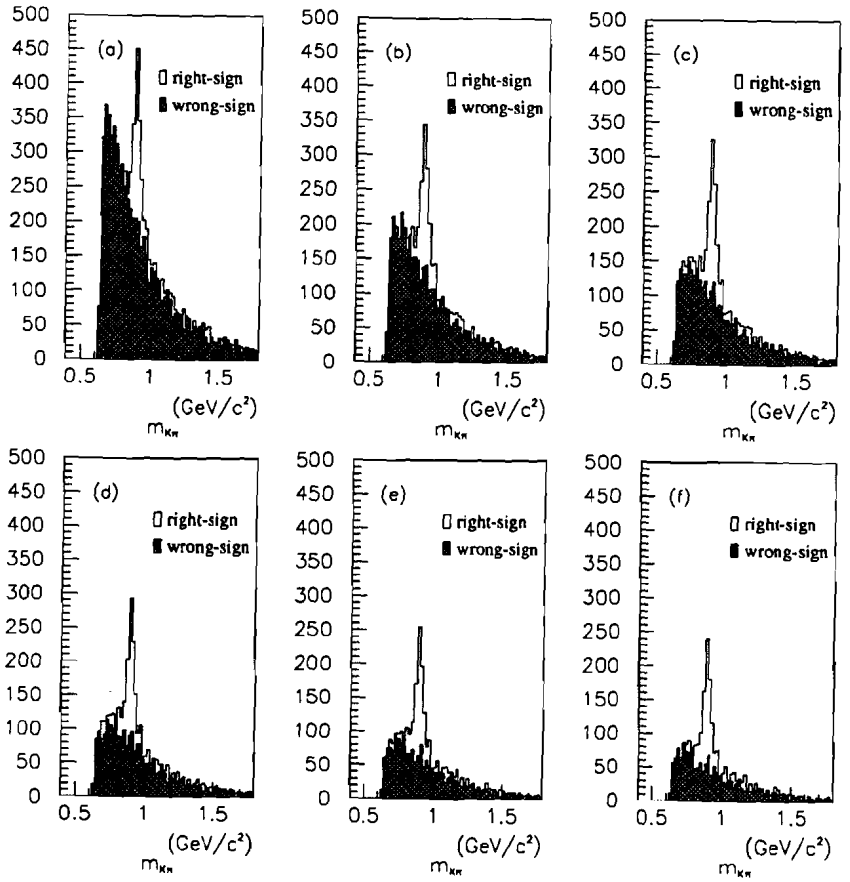

Figure 5.3. The cumulative effects of applying each selection cut on the data. The solid line shows the right-sign data and the shaded area represents the wrong-sign data. In (a), the signal is shown after all previous cuts listed in previous sections have been applied. The subsequent cuts applied here are (b) rejecting electron candidates consistent with being a member of a photoconversion pair, (c) rejecting events with tracks consistent with pointing back to the primary vertex, (d) rejecting events containing tracks consistent with belonging to the primary vertex based on their impact parameter with respect to the primary vertex (e) requiring Čerenkov identification for the π and (f) $\chi^2/d.o.f.$ cut for each track. All cuts are described in the text.

Table 5.1. Effect of the removal of each cut on the signal-to-background ratio for the data after adjusting each cut with Monte Carlo events. The results are shown for data with the wrong-sign data used to monitor the non-charm background.

	signal/background
after all cuts	5.85
removed cut	
eliminate electrons from photoconversion pairs	3.6
total momenta must point back to primary vertex	4.5
e, π , K tracks must be inconsistent with primary vertex	5.0
require χ^2/dof for each track < 3.5	4.13
require Čerenkov identification for π	4.83

events. Only events with a value of $m_{K\pi}$ within 0.84 and 0.95 GeV/c^2 are retained for the final sample. The wrong-sign $M_{K\pi}$ distribution subtracted from the right-sign $M_{K\pi}$ distribution is shown in Figure 5.5(c) fitted to a Breit-Wigner shape of fixed width and mean. The fit shows good agreement between the wrong-sign-subtracted signal and a pure Breit-Wigner distribution indicating that the wrong-sign signal adequately represents the non-charm background and that the signal is dominated by $D^+ \rightarrow \bar{K}^{*0}e^+\nu_e$.

The number of $D^+ \rightarrow \bar{K}^{*0}e^+\nu_e$ candidate events based on $\approx$ 15% of the full E791 data sample are shown in Table 5.2 after all selection cuts and compared to the signals reported by other experiments, for $D^+ \rightarrow \bar{K}^{*0}l^+\nu_l$. [31, 12, 11, 10] Although E791 will have signals in both leptonic channels, only the electron signal is tabulated here. The projected number of signal events for the full E791 data sample is approximately 2600 using the series of cuts described in the text.

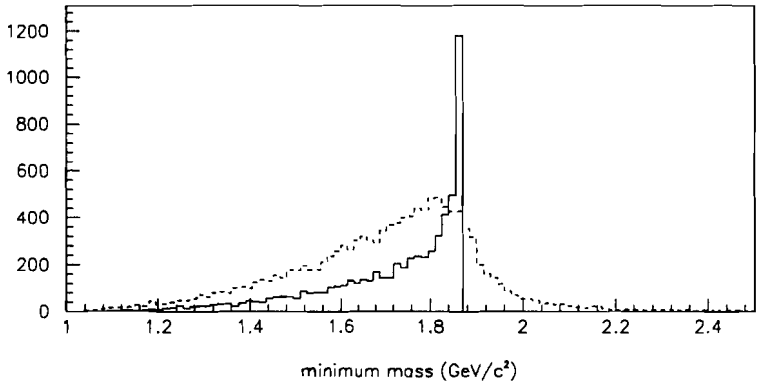

Figure 5.4. The m_{min} distribution obtained from a Monte Carlo simulation for the decay $D^+ \rightarrow \bar{K}^{*0} l^+ \nu_l$. The effects of smearing on this distribution are shown by the dashed curve.

Table 5.2. Comparison of sample sizes for E791 and for other experiments, for $D^+ \rightarrow \bar{K}^{*0} l^+ \nu_l$.

	E691	E653	E687	E791
lepton type	e	μ	μ	e only (15% data)
# of right-sign events	204	305	$\approx$ 1001	418
# of wrong-sign events	21	$\approx$ 30	$\approx$ 126	61
# of signal events	183	$\approx$ 275	875 $\pm$ 44	357$\pm$ 22
signal/background	8.7	$\approx$ 9.2	$\approx$ 6.9	5.9

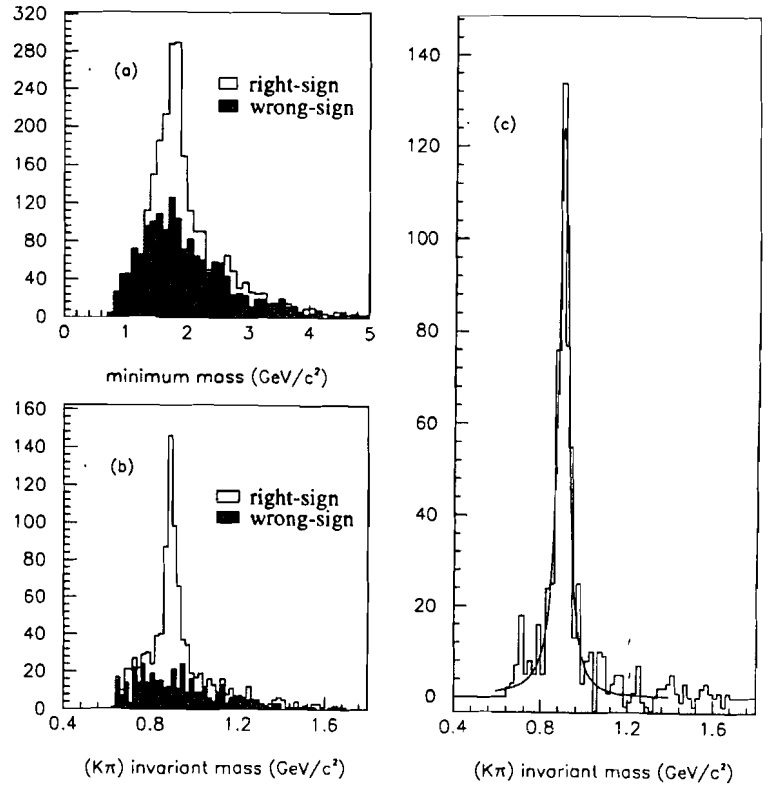

Figure 5.5. (a) Minimum mass distribution for right-sign events (wrong-sign events in shaded area) for the electron signal selected using the cuts described in the text for 15% of the full E791 data sample. (b) $K\pi$ invariant mass distribution for events selected within a m_{min} window of 1.6-2.0 GeV/c^2. (c) Wrong-sign subtracted signal for selected events fitted to a Breit-Wigner shape with fixed width and mean.

6. Fitting Technique

6.1 Maximum likelihood technique

To describe the method used to extract the form factors, we will introduce some general variables. Let μ be the set of parameters to be extracted; in this analysis, μ represents the pair of form factors R_2 and R_V. Let x_i denote the kinematic variables for event i on which the decay rate $\Gamma(x_i,\mu)$ depends; in this analysis, x_i represents the five kinematic variables $\cos\theta_l$, $\cos\theta_V$, χ, $m_{K\pi}$ and q^2 introduced in chapter 1. Then the likelihood $\mathcal{L}$ that a set of n observed events are distributed according to $\Gamma(x_i,\mu)$ is the appropriately normalized product of probabilities for each event [32]:

$$\mathcal{L} = \prod_{i=1}^{n} \frac{\Gamma(x_i,\mu)}{N(\mu)}. \tag{6.1}$$

$N(\mu)$ is the normalization constant $N(\mu) = \int \Gamma(x_i,\mu)dx_i$. The best estimate of the parameter μ is that value of μ which maximizes the likelihood of the data. To avoid taking a product of many small or large numbers, we actually use log likelihood, and since the fitting code we use minimizes functions, we take the the negative log likelihood:

$$-ln\mathcal{L} = -\sum_{i=1}^{n} \Big[ln\Gamma(x_i,\mu) - lnN(\mu)\Big]. \tag{6.2}$$

The relationship between a change in the value of the log likelihood and the number-of-standard-deviations confidence level, n_σ, calculated using a normal distribution, is $\delta ln(\mathcal{L}) = n_\sigma^2/2$. So, for example, a one-standard-deviation confidence level corresponds to a half unit change in $ln\mathcal{L}$.

The technique described above is the standard maximum likelihood method for estimating a set of parameters given an analytic formula for the probablility distribution $\Gamma(x_i,\mu)$. We now discuss how we take into account the fact that our observed distributions are not expected to correspond to the analytic distribution due to acceptance and smearing effects.

6.2 Including smearing and acceptance

The form factor ratios R_2 and R_V determine the dependence of the differential decay rate for $D^+ \to \bar{K}^{*0}l^+\nu_l$ on the five kinematic variables $M^2_{K\pi}$, q^2, $\cos\theta_V$, $\cos\theta_l$ and χ, as described by equation 2.8 in chapter 1. In principle, one can perform a maximum likelihood fit to the observed distribution of kinematic variables to extract the form factors as described in the previous section. However, the distribution of kinematic variables in the data is affected by detector acceptance effects (which can result in events in certain parts of phase space never being observed) and smearing due to both the limited resolution of the detector and the quadratic ambiguity in the determination of the neutrino momentum. A method was devised for a similar analysis [33] to take into account the acceptance and smearing effects using Monte Carlo simulated $D^+ \to \bar{K}^{*0}l^+\nu_l$ decays which have been passed through the same analysis chain as the data. The technique used in our analysis is almost identical except for how the non-charm background events are accounted for in the fit. The technique is described in this chapter with more detail available in references 33 and 34.

To account for smearing and acceptance effects, one can compare the data to a large sample of Monte Carlo events which have also been smeared by the reconstruction algorithm and affected by detector acceptance. Monte Carlo events are generated with a known distribution of the kinematic variables. For each generated Monte Carlo event, the true values of the five kinematic variables are known (the generated values) as well as their smeared values after going through the reconstruction code. Let y_i denote the true Monte Carlo values for the kinematic variables and $\tilde{y}_i$ their smeared value. Of course, for the real data events, we can only measure the smeared values $\tilde{x}_i$. To take into account smearing and acceptance effects, we compare the distribution of $\tilde{x}_i$ from the data to that of the $\tilde{y}_i$ for Monte Carlo events. We calculate the likelihood of each event in the data as the sum of the weights $W(y_j,\mu)$ of those Monte Carlo events which lie within a small multi-dimensional volume in the space of kinematic variables surrounding that data point $\tilde{x}_i$ where the match of Monte Carlo events to the volume is done using the smeared quantities $\tilde{y}_i$. Then eq. (6.2) becomes

$$-ln\mathcal{L} = -\sum_{i=1}^{n} ln\Big(\frac{\sum_{\tilde{y}_j \text{ in } V_i} W(y_j,\mu)}{C(\mu)V_i}\Big) \tag{6.3}$$

where V_i is the volume centered around $\tilde{x}_i$, $C(\mu) = \sum_{j=1}^{m} W(y_j,\mu)$ is the normalization and m is the total number of Monte Carlo events. The weight function $W(y_j,\mu)$ is calculated using the true values y_i.

To avoid generating several sets of Monte Carlo samples with different distributions of the kinematic variables to determine which set best fits the data, one can use one set of generated events and a simple weighting technique to produce differential decay rates for different hypotheses for the parameters μ. The weight for each Monte Carlo event can be evaluated from the known values of the kinematic variables y_i using the relation

$$W(y_i,\mu) = \frac{\Gamma(y_i,\mu)}{\Gamma(y_i,\mu_0)} \tag{6.4}$$

where $\Gamma(y_i,\mu_0)$ is the differential decay rate for the initial values of the parameters μ_0 used to generate the Monte Carlo events, and μ is the new hypothesis for the

parameters. For the parameters μ_0 with which the Monte Carlo events were generated, $W(y_j, \mu_0)$ is just one. In this case, the summation over Monte Carlo events within V_i in equation (6.3) just corresponds to the number of Monte Carlo events in V_i.

6.3 Including the background

To include the effects of non-charm background, we assume our data sample contains N_B background events, where N_B equals the number of wrong-sign events that pass all selection criteria described in the previous chapter. For n observed events and N_B background events distributed according to some normalized probability function $P_B(\tilde{x}_i)$, we can write the likelihood $\mathcal{L}_i$ for event i to be signal or background as

$$\mathcal{L}_i = \left[(n - N_B) \frac{\Gamma(x_i, \mu)}{N(\mu)} + N_B P_B(\tilde{x}_i) \right]. \tag{6.5}$$

Then, eq. (6.3) can be modified to include the effects of background as follows:

$$-ln\mathcal{L} = -\sum_{i=1}^{n} ln \left[\frac{(n - N_B) \sum_{\tilde{y}_j \text{ in } V_i} W(y_j, \mu)}{C(\mu) V_i} + N_B P_B(\tilde{x}_i) \right]. \tag{6.6}$$

For example, assuming flat distributions for the kinematic variables for the background events and no dependence on the fit parameters μ, we can write the normalized probability function for the background, $P_B(\tilde{x}_i)$, as $1/V$ where V is the volume of the multi-dimensional space spanned by the kinematic variables. Then, $\int P_B(\tilde{x}_i)\, dV = 1$ is properly normalized when integrated over the whole volume.

Rather than assuming uniform background distributions, we used the observed distribution of kinematic variables $\tilde{x}_k$ for the wrong-sign events to represent the background. We can write the likelihood that event i in the right-sign data sample is distributed according to the wrong-sign sample as:

$$\mathcal{L}_i = \frac{\sum_{\tilde{x}_k \text{ in } V_i^B} W(x_k)}{C(\mu) V_i^B} \tag{6.7}$$

where V_i^B is the volume centered around data point $\tilde{x}_i$. But $W(\tilde{x}_k) = 1$ because we are assuming the background is distributed like the wrong-sign events. Therefore, $\sum_{k=1}^{N_i} W(\tilde{x}_k) = N_i$ where N_i is the number of background events found within the volume element V_i^B surrounding data point i. The normalization factor $C(\mu) = \sum_{k=1}^{N_B} W(x_k) = N_B$. Putting everything together, we get:

$$P_B(\tilde{x}_i) = \mathcal{L}_i = \frac{N_i}{N_B V_i^B}. \tag{6.8}$$

Substituting eq. (6.8) into eq. (6.6), we get the final result

$$-ln\mathcal{L} = -\sum_{i=1}^{n} ln \left[\frac{(n - N_B) \sum_{\tilde{y}_j \text{ in } V_i} W(y_j, \mu)}{C(\mu) V_i} + \frac{N_i}{V_i^B} \right]. \tag{6.9}$$

With this method, it is possible to make a maximum likelihood fit in any number of dimensions while taking into account acceptance and smearing effects as well as the background contributions.

6.4 Generating the Monte Carlo events

Over one million Monte Carlo events were generated according to the expression derived in chapter 1 for the differential decay rate describing the decay $D^+ \rightarrow \bar{K}^{*0} l^+ \nu_l$:

$$\begin{aligned} \frac{d\Gamma}{dM_{K\pi}^2\, dq^2\, d\cos\theta_V\, d\cos\theta_l\, d\chi} &= G_F^2 |\, V_{cs}\, |^2 \frac{3}{2(4\pi)^5} \frac{M_{K^*}}{M_D^2 M_{K\pi}}\, K q^2 \\ &\times \frac{M_{K^*} \Gamma(M_{K\pi})}{(M_{K\pi}^2 - M_{K^*}^2)^2 + M_{K^*}^2 \Gamma^2(M_{K\pi})} \\ \times \{ \, [\, (1 + \cos\theta_l)^2 \mid H_+(q^2) \mid^2 &+ (1 - \cos\theta_l)^2 \mid H_-(q^2) \mid^2] \, \sin^2\theta_V \\ &+ 4 \sin^2\theta_l \, \cos^2\theta_V \mid H_0(q^2) \mid^2 \\ &- 2 \sin^2\theta_l \, \sin^2\theta_V \, Re\, (e^{i2\chi} H_+^* H_-) \\ &- 4 \sin\theta_l \, (1 + \cos\theta_l) \, \sin\theta_V \, \cos\theta_V \, Re\, (e^{i\chi} H_+^* H_0) \\ &+ 4 \sin\theta_l \, (1 - \cos\theta_l) \, \sin\theta_V \, \cos\theta_V \, Re\, (e^{i\chi} H_-^* H_0) \, \}. \end{aligned} \tag{6.10}$$

The angles θ_l, θ_V and χ refer to the angles shown in Figure 2.2 , q^2 is the invariant mass of the W and $M_{K\pi}$ is the invariant mass of the K^*. The form factor ratios R_2 and R_V defined in chapter 1 are buried in the expressions for the helicity amplitudes:

$$H_\pm(q^2) = (M_D + M_{K\pi})\, A_1(q^2) \mp 2 \frac{M_D\, K}{M_D + M_{K\pi}}\, V(q^2)$$

and

$$\begin{aligned} H_0(q^2) = \frac{1}{2 M_{K\pi} q} \Big[&(M_D^2 - M_{K\pi}^2 - q^2)(M_D + M_{K\pi})\, A_1(q^2) \\ &- 4 \frac{M_D^2\, K^2}{M_D + M_{K\pi}} A_2(q^2) \Big] \end{aligned} \tag{6.11}$$

with $R_2 = A_1(0)/A_2(0)$ and $R_V = A_1(0)/V(0)$. The assumed q^2-dependence of the

form factor, as discussed in chapter 1, is

$$F(q^2) = \frac{F(0)}{1 - q^2/m^2_{pole}}. \qquad (6.12)$$

We used the values measured by the E653 collaboration for the form factor ratios to generate our Monte Carlo events, namely R_2=0.82 and R_V=2.0 . Any values for R_2 and R_V would have been acceptable as a starting point but it is best to generate the data with distributions as close to the data as possible. This allows more efficient use of the generated Monte Carlo events since it brings all the weights closer to one. The projected distributions for four of the kinematic variables used in the fit are shown in Figure 6.1. The distributions are shown before any modification due to acceptance or smearing. The variable $M_{K\pi}$will be discussed later.

To accelerate the Monte Carlo generation process, before simulating the passage of particles through the detector, we discarded events which would be rejected by the reconstruction code due to limited detector acceptance. Events with values of x_F less than -0.1 were rejected, where x_F is defined as the ratio of the D momentum component along the beam axis in the πp center-of-mass to its maximum kinematically allowed value. Decay products from charmed hadrons with negative values of x_F do not enter the detector. Events in which the electron does not enter the fiducial area of the calorimeter were also rejected. Similarly, events which would not pass a mild SDZ cut or in which the beam particle interacted in material downstream from the target were rejected before digitization since these events would be discarded later in the analysis, as discussed in the previous chapter. The effects of these rejection cuts, and all subsequent cuts applied in the analysis, on the distributions of the kinematic variables are discussed in the next section.

6.5 Acceptance and smearing effects

The Monte Carlo events were generated according to eq. (6.10) and passed through the same reconstruction and analysis code as the data. Of the 1,137,300 generated Monte Carlo events, 11,085 passed all the selection criteria. The number of events that passed each stage of the analysis code is shown in Table 6.1.

To study how much the distributions of the kinematic variables were affected by the selection cuts described in the previous chapter, we looked at how these distributions changed after each cut and determined which cut had the largest effect. The acceptance as a function of each kinematic variable is plotted (in arbitrary units for acceptance) in Figure 6.2 when the filtering cuts are applied and a 3-prong vertex with an electron is required, and in Figure 6.3 for the last series of cuts described in Table 6 in chapter 5 . The requirement that the electron point to the active area of the electromagnetic calorimeter causes the low acceptance in $\cos\theta_l$ near $\cos\theta_l = -1$

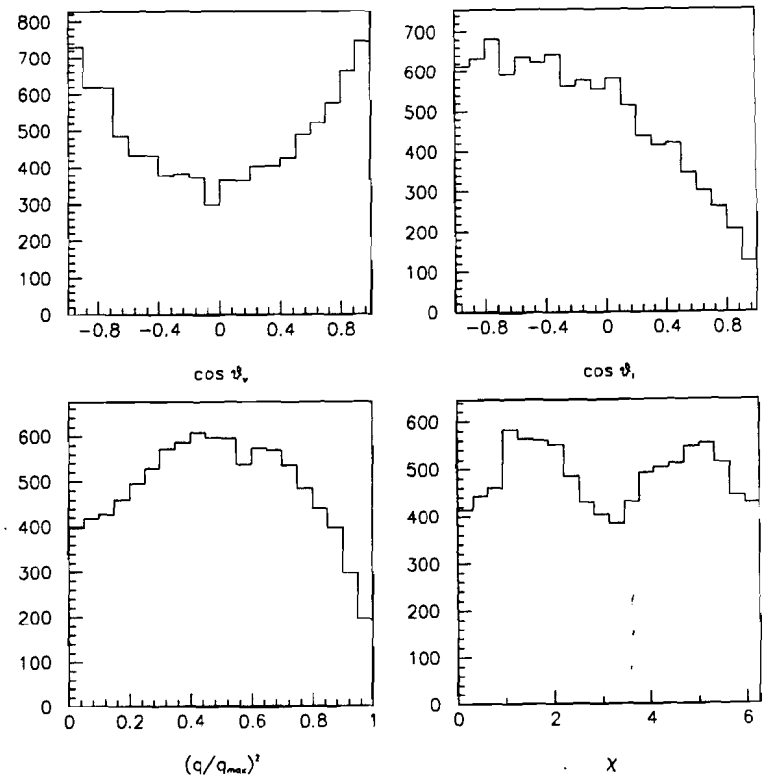

Figure 6.1. The projected distributions of four of the generated kinematic variables in the Monte Carlo. These distributions have not yet been affected by acceptance and smearing. The Monte Carlo events were generated using the values of R_2 and R_V measured by E653, namely 0.82 and 2.0 .

in Figure 6.2. The cut on the minimum mass m_{min} affects the shape of the distributions of both $\cos\theta_l$ and q^2 in Figure 6.3. Both cuts preferentially remove D decays with very low momentum electrons which correspond to low values for $\cos\theta_l$ and q^2. The effects of these cuts on the final results will be addressed in the last chapter when discussing systematic uncertainties.

We also checked that the loss of acceptance at low $\cos\theta_l$ was not caused by a poor Monte Carlo simulation of the variable EMPROB used for electron identification. We replaced the cut based on EMPROB in the Monte Carlo by an electron identification algorithm based on the true identity of the track. An electron track was retained or rejected according to electron identification efficiencies measured in the data as a

Table 6.1. The number of Monte Carlo events retained at each stage of the selection process. About 1,137,300 Monte Carlo $D^+ \to \bar{K}^{*0} e^+ \nu_e$ events were generated.

analysis stage	events retained	fraction of generated events
filter	619986	54.51%
lepton strip	252727	22.22%
all cuts	11085	0.97%

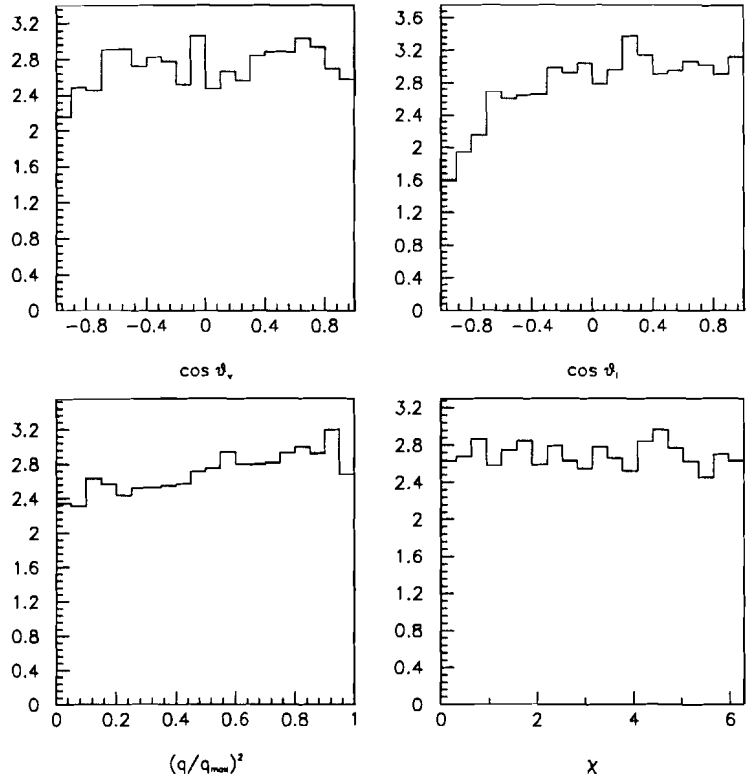

Figure 6.2. Acceptance as a function of each of the four kinematic variables used for the fit after applying the filtering cuts and finding a secondary 3-prong vertex containing an electron track that intercepts the SLIC. The dip in acceptance at low values of $\cos\theta_l$ comes from rejecting low electron momentum tracks pointing outside the active region of the SLIC.

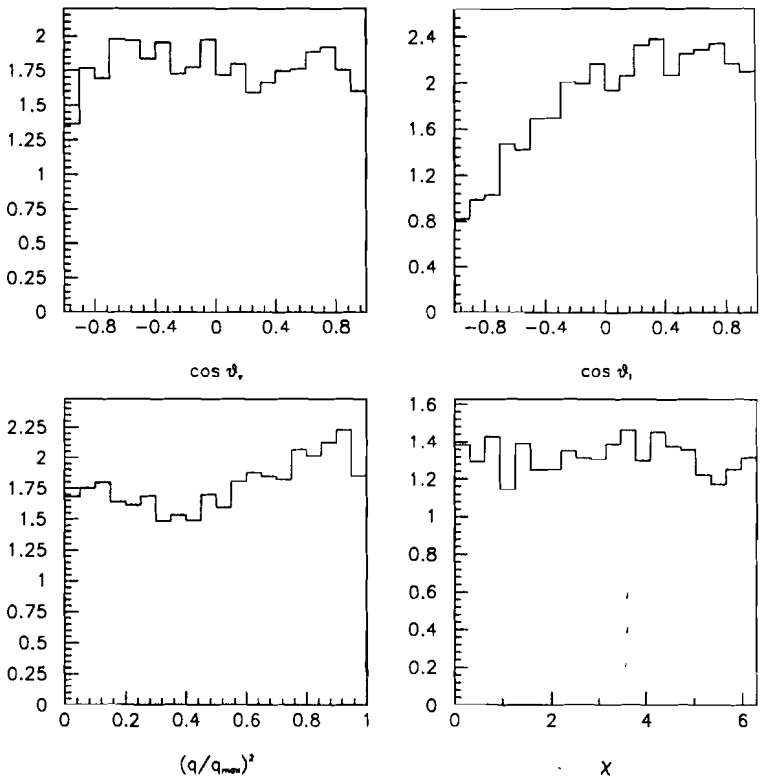

Figure 6.3. Acceptance as a function of four of the kinematic variables used for the fit after applying all the remaining cuts listed in Table 6 in chapter 5 but without any smearing effects due to detector resolution or solving for the neutrino momentum.

function of momentum (see chapter 4). No change in acceptance was noticed when substituting this algorithm for electron identification based on EMPROB. For completeness, we include the distributions of the kinematic variables for both right-sign and wrong-sign sign data samples in Figure 6.4 and Figure 6.5.

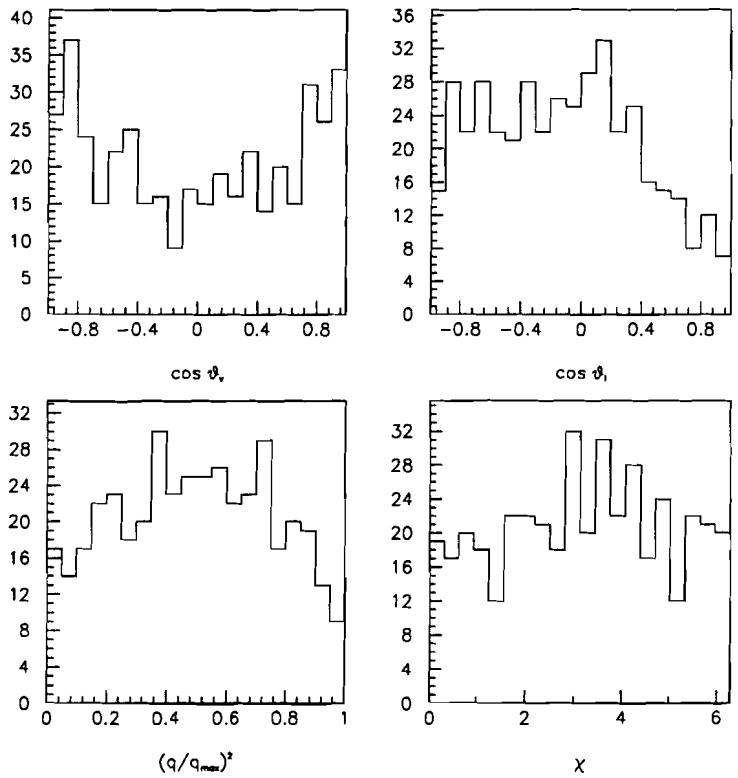

Figure 6.4. The projected distributions of four of the generated kinematic variables in the right-sign data sample.

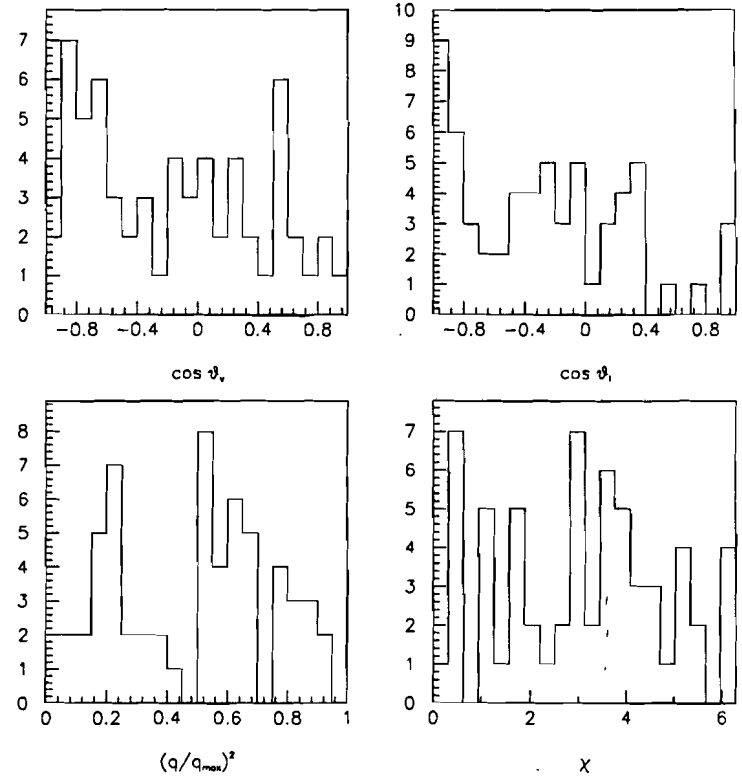

Figure 6.5. The projected distributions of four of the generated kinematic variables in the wrong-sign data sample.

6.6 Testing the uncertainties on the fit

To perform the maximum likelihood fit, we used the MINUIT fitting package from CERN [4]. As a check of the validity of the uncertainties on the fit parameters calculated by MINUIT, we divided our Monte Carlo data into 31 smaller, independent samples each the size of our data sample after background subtraction, that is 357 events. We treated each smaller Monte Carlo sample as "data" and performed the fit using the remainder of the Monte Carlo events in the usual way. We first used the generated momenta for the four D decay products (K, π, e, ν) to avoid any smearing effects. The values for the form factor ratios R_2 and R_V from the fit are expected on average to be the ones with which the Monte Carlo was generated. The distribution of R_2 and R_V from the fits for the ensemble of Monte Carlo samples was plotted and the RMS of these distributions was calculated. The mean on the uncertainties on the best fit values returned by MINUIT were also calculated. The results are shown in Table 6.2. The spread of best fit values for R_2 and R_V (column 4) compares very well with the mean of the uncertainties returned by MINUIT (column 5). The distributions of $(\mu_{true} - \mu_{meas})/\sigma_\mu$ should be centered at zero with an RMS value of 1. The actual distributions show a systematic bias toward a lower value for R_2 and a slightly higher value for R_V. The RMS of these disributions is close to one for both R_2 and R_V, confirming the validity of the error on each fit parameter calculated by MINUIT. The systematic shift in the returned values of the fit parameters will be taken into account in the next chapter.

Table 6.2. Results of the fit to an ensemble of 31 independent samples of 357 Monte Carlo events each to check the uncertainties on the fit parameter calculated by MINUIT. The fit was performed separately with each sample using the generated values of the kinematic variables, leaving out any smearing effect due to detector resolution or quadratic ambiguity in determining the ν momentum. Here, $\langle\mu\rangle$ represents the mean value of the parameter μ and $\langle\sigma_\mu\rangle$ is the mean error on this parameter for 31 fits performed by MINUIT. The RMS for μ corresponds to the root-mean-square distribution of 31 values of μ. The last two colums show $\langle(\mu_{true} - \mu_{meas})/\sigma_\mu\rangle$ and the RMS on this distribution. These results show a systematic bias toward a lower measured value for R_2 and a higher value for R_V but confirm the accuracy of the uncertainties returned on the fit parameters by MINUIT.

parameter	true value	$\langle\mu\rangle$	RMS for μ	$\langle\sigma_\mu\rangle$	RMS for σ_μ	$\langle(\mu_{true} - \mu_{meas})/\sigma_\mu\rangle$	RMS
R_2	0.82	0.68	0.29	0.24	0.04	-0.49	1.19
R_v	2.0	2.10	0.33	0.33	0.04	0.22	0.92

6.7 Effect of volume sizes V_i

In equation (6.3), V_i is a volume centered around data event i. Monte Carlo events within this volume are used to calculate the likelihood of event i for a particular set of form factors. This calculated likelihood will be a good estimate of the true probability for this event if the differential decay rate changes at most linearly across the volume and if there are sufficient Monte Carlo events within the volume to limit the statistical uncertainty. The volume size V_i must be chosen so that neither of these effects dominates. In addition, there is no benefit in making V_i much smaller than the size of the smearing of the kinematic variables. To take into account these sometimes conflicting needs, we performed the fit using different volume sizes around each data point to find the range in which the fit is stable. Again, the use of an ensemble of Monte Carlo samples proved to be very useful. We first rejected any "data" point which did not contain at least four Monte Carlo events within its surrounding volume. This proved to be unecessary since the overall normalization constant in the expression for the maximum likelihood properly weights data points with few Monte Carlo events within their surrounding volume. For data points located near the edges of the distributions of the kinematic variables, we adjusted the volume size such that the data point remained at the center of the volume surrounding it. This reduced the number of Monte Carlo points found within these shrunk volumes such that some of these data events were rejected. Volumes were shrunk in one dimension only if the size of the volume corresponded to less than a fifth of the kinematic range for this variable. We used a coarser binning for the angle χ since it was the most sensitive to smearing effects due to limited resolution in determining the D meson direction of flight from the position of the primary and secondary vertices. Although $M_{K\pi}$ does not contain information on the form factors, it provides significant discrimination power between real $D^+ \to \bar{K}^{*0} e^+ \nu_e$ and non-charm background. The results of the fit are shown in Table 6.3 for different volume sizes, both when we reject data points with less than one or less than four Monte Carlo points within their surrounding volume. The results of the fit are stable for volume sizes chosen between 1/1296 to 1/3000 of the total volume, as seen in Figure 6.6 for R_2 and R_V. The systematic shift towards lower values has disappeared for R_2 but R_V exhibits a shift towards a higher value. This will be taken into account when we fit for R_2 and R_V in the data. For the rest of this analysis (unless specified otherwise), we use a volume corresponding to 1/1458 of the total volume, and we do not use the variable χ in the fitting procedure.

6.8 Determining the neutrino momentum

With real data, no tracking information is available for the neutrino but it is possible, given the momenta of the three visible particles, to calculate the neutrino momentum up to a quadratic ambiguity. From momentum and energy conservation laws, we can write

$$m_D^2 = (p^{vis} + p^\nu)^2 = m_{vis}^2 + 2\,(p^{vis} \cdot p^\nu)\,. \tag{6.13}$$

As well as having information about the 4-momenta of the charged D decay products, we can also estimate the direction of the D meson from the position of the primary and secondary vertices. We have a constraint on the transverse momentum of the neutrino with respect to the direction of the D meson: $\vec{p}_\perp^{\,\nu} = -\vec{p}_\perp^{\,vis}$. If we boost the visible 4-momenta along the direction of the D meson to the frame where the component along the D direction $p_\parallel^{vis}$ is zero, then we can easily transform the relation (6.13) into a relation for $p_\parallel^\nu$ in terms of measurable quantities:

$$\begin{aligned} m_D^2 &= m_{vis}^2 + 2\,(E^{vis}E^\nu - p_\parallel^{vis}p_\parallel^\nu + p_\perp^{vis}p_\perp^\nu) \\ &= m_{vis}^2 + 2\,(E^{vis}E^\nu + (p_\perp^{vis})^2) \\ &= m_{vis}^2 + 2\left[E^{vis}\sqrt{(p_\perp^{vis})^2 + (p_\parallel^\nu)^2} + (p_\perp^{vis})^2\right]. \end{aligned} \tag{6.14}$$

Therefore,

$$\sqrt{(p_\perp^{vis})^2 + (p_\parallel^\nu)^2} = \frac{m_D^2 - m_{vis}^2 - 2(p_\perp^{vis})^2}{2E^{vis}}$$

and finally

$$p_\parallel^\nu = \pm\left[\left(\frac{m_D^2 - m_{vis}^2 - 2\,(p_\perp^{vis})^2}{2\,E^{vis}}\right)^2 - (p_\perp^{vis})^2\right]^{1/2}. \tag{6.15}$$

Table 6.3. Results of the fit for different volume sizes. These results were established using an ensemble of Monte Carlo events generated with $R_2 = 0.82$ and $R_V = 2.0$. The full range of each kinematic variable is as follows: $\cos\theta_l = [-1, 1]$, $\cos\theta_V = [-1, 1]$, $q^2/q^2_{max} = [0, 1]$, $\chi = [0, 2\pi]$, and $m_{K\pi} = [0.85, 0.94]$ GeV/c^2.

fraction of total volume	# of points rejected	$\Delta\cos\theta_l$	$\Delta\cos\theta_V$	$\Delta q^2/q^2_{max}$	$\Delta\chi$	$\Delta m_{K\pi}$	$\langle R_2\rangle$	$\langle\sigma_2\rangle$	$\langle R_V\rangle$	$\langle\sigma_V\rangle$
require at least 4 Monte Carlo points per volume										
1/512	16	0.25	0.25	0.13	6.28	0.09	0.70	0.36	2.42	0.59
1/1000	37	0.20	0.20	0.10	6.28	0.09	0.75	0.33	2.47	0.50
1/1536	85	0.25	0.25	0.13	6.28	0.03	0.71	0.35	2.54	0.51
1/3000	172	0.20	0.20	0.16	6.28	0.03	0.58	0.42	2.62	0.56
require at least 1 Monte Carlo point per volume										
1/343	4	0.29	0.29	0.14	6.28	0.09	0.71	0.32	2.18	0.49
1/512	5	0.25	0.25	0.13	6.28	0.09	0.71	0.31	2.17	0.46
1/1000	8	0.20	0.20	0.10	6.28	0.09	0.78	0.28	2.15	0.45
1/1029	13	0.29	0.29	0.14	6.28	0.09	0.79	0.28	2.16	0.40
1/1296	37	0.33	0.33	0.17	2.09	0.03	0.83	0.25	2.13	0.32
1/1458	17	0.22	0.22	0.17	6.28	0.03	0.83	0.26	2.12	0.36
1/1536	18	0.25	0.25	0.13	6.28	0.03	0.81	0.27	2.17	0.32
1/2058	50	0.29	0.29	0.14	3.14	0.03	0.80	0.30	2.19	0.40
1/2400	34	0.20	0.20	0.13	6.28	0.03	0.83	0.24	2.15	0.32
1/2916	63	0.22	0.22	0.17	3.14	0.03	0.80	0.26	2.21	0.32
1/3000	26	0.20	0.20	0.16	6.28	0.03	0.82	0.25	2.18	0.34
1/3072	65	0.25	0.25	0.13	3.14	0.03	0.79	0.25	2.21	0.33
1/3087	51	0.29	0.29	0.14	2.09	0.03	0.86	0.24	2.18	0.31
1/4800	89	0.20	0.20	0.13	3.14	0.03	0.81	0.25	2.30	0.32
1/10125	121	0.13	0.13	0.07	3.14	0.03	0.77	0.25	2.20	0.31

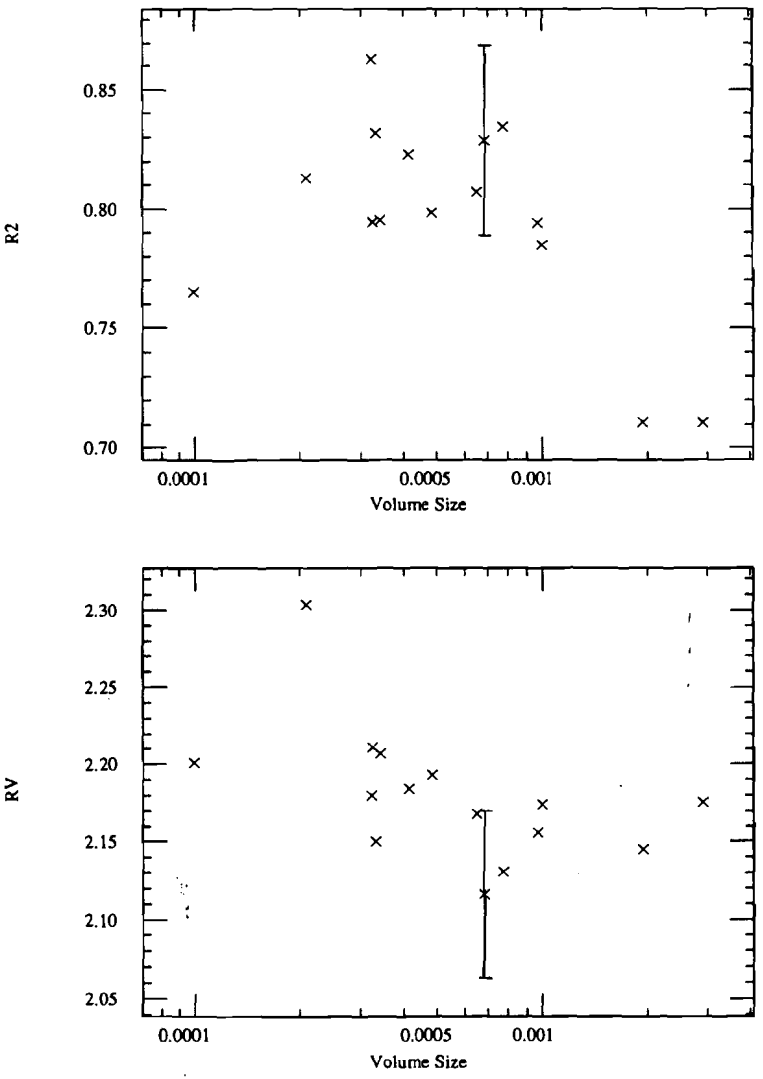

Figure 6.6. Measured value of R_2 (top plot) and R_V (bottom plot) for an ensemble of Monte Carlo samples for various volume sizes. The generated values of R_2 and R_V are 0.82 and 2.0, respectively. The results of the fit are not sensitive to the volume size when it is in the range 1/1296 to 1/3000 of the total volume. The volumes are shown on a logarithmic scale.

Table 6.4. Results of the fit to an ensemble of 35 independent Monte Carlo samples to determine the best solution for the neutrino momentum. The negative solution introduces less smearing of the kinematic variables and yields smaller errors on the form factors ratios R_2 and R_V. The variable $\langle\mu\rangle$ refers to the mean value of the parameter μ obtained from 35 fits performed by MINUIT.

		negative solution		positive solution	
parameter	true value	$\langle\mu\rangle$	$\langle\sigma_\mu\rangle$	$\langle\mu\rangle$	$\langle\sigma_\mu\rangle$
no smearing from detector resolution					
R_2	0.82	0.78	0.26	0.69	0.25
R_V	2.00	2.15	0.35	2.14	0.35
including smearing from detector resolution					
R_2	0.82	0.83	0.27	0.69	0.28
R_V	2.00	2.12	0.37	2.24	0.38

Both E691 and E653 determined that the negative solution for $p_{\|}^{\nu}$ introduced less smearing of the kinematic variables than the positive solution. We tested this assertion using our Monte Carlo sample. Each solution for the quadratic equation for the neutrino momentum from eq. (6.15) is compared to the real value of the neutrino momentum as generated in the Monte Carlo. The positive solution corresponds to the generated value $(55.0 \pm 0.6)\%$ of the time. When the neutrino momentum is not reconstructed correctly due to the quadratic ambiguity, the kinematic variables are also reconstructed incorrectly. To determine the effect of this smearing of the kinematic variables on the extracted form factors, we again use an ensemble of 35 sets of Monte Carlo events which we treat as "data" in the maximum likelihood fit as described in the previous section. We first use the generated momenta of the charged particles to determine the neutrino momentum up to the quadratic ambiguity. We then calculate the average value of the form factors and the average value of the errors from the 35 fits for the positive solution for the ν momentum and for the negative solution. The results are shown in the top half of Table 6.4. We repeated the study using smeared (reconstructed) values for the charged particles momenta. The results are shown in the bottom half of Table 6.4. By comparing the true value to the fit value of the form factors for each solution we determine that the negative solution yields a better measurement of the form factor ratios R_2 and R_V. Comparing these results to Table 6.2 (where the fit was performed with the generated values of the neutrino momentum), we note that the systematic bias of the fitting procedure is somehow cancelled when smearing is introduced.

7. Results and Conclusion

7.1 Introduction

In this chapter, we present the results for R_2 and R_V obtained using the fitting technique described in the previous chapter applied to the candidate $D^+ \to \bar{K}^{*0}e^+\nu_e$ decays in the data. We also evaluate the contributions to the systematic uncertainty on the form factor ratios R_2 and R_V. Our results are compared to previous experimental measurements. Finally, some projections on the size of the uncertainties on the final result from the full E791 data sample are made.

7.2 Results

The results of the fit to the 418 candidate $D^+ \to \bar{K}^{*0}e^+\nu_e$ decays in the data are shown in Table 7.1. We use the negative solution of the quadratic equation to determine the neutrino momentum. The fit was performed using a volume size V_i of 1/1458 of the total volume to compare the data event to the Monte Carlo generated events. The volume size V_i^B around each data point used to compare the data to the background corresponds to 1/81 of the total volume. The choice of V_i and V_i^B will be justified in the following section. The correlation coefficient between the two fit parameters is -0.324 .

Table 7.1. Results of the fit to the data using a data sample corresponding to 15% of the full E791 data sample.

parameter	measured value	statistical uncertainty
R_2	0.32	$^{+0.26}_{-0.27}$
R_V	2.40	$^{+0.39}_{-0.37}$

7.3 Contributions to the systematic uncertainty

Systematic uncertainties due to the effect of the m_{min} cut, the choice of volume size for signal and background in the fit, and the simulation of the D momentum in the Monte Carlo are discussed in this section.

7.3.1 Uncertainty from the m_{min} cut

As mentioned in the previous chapter, the m_{min} cut is very efficient at rejecting non-charm background but strongly affects the acceptance in $\cos\theta_l$ and q^2, particularly at low $\cos\theta_l$ and q^2. To study the effects of this cut on the final result, we relaxed

the m_{min} cut from its initial value of 1.6 to 1.3 and then 1.0 GeV^2. The primary effect of relaxing the m_{min} cut is to greatly contaminate the data sample. Even with a poorer signal-to-background ratio, we can still use the same fitting method since it is designed to take into account background contamination. The results of the fit for different ranges in m_{min} are shown in Table 7.2.

Table 7.2. Effect of m_{min} and background volume size on the fit results for the data. The signal-to-background ratio (S/B) increases as the m_{min} range is increased. Since the fitting technique takes care of the increased contamination from non-charm decays, this allows us to test the effects of the background volume size.

volume size for background $V_i^B = 1/16$ of total volume							
m_{min} range	right-sign events	wrong-sign	S/B	R_2	σ_{R_2}	R_V	σ_{R_V}
1.0 – 2.0	633	151	3.19	0.10	0.32	2.89	0.47
1.3 – 2.0	587	122	3.81	0.10	0.31	2.78	0.46
1.6 – 2.0	418	61	5.85	0.21	0.29	2.47	0.43
volume size for background $V_i^B = 1/81$ of total volume							
1.0 – 2.0	633	151	3.19	0.24	0.28	2.62	0.38
1.3 – 2.0	587	122	3.81	0.22	0.28	2.56	0.34
1.6 – 2.0	418	61	5.85	0.32	0.27	2.40	0.38
volume size for background $V_i^B = 1/256$ of total volume							
1.0 – 2.0	633	151	3.19	0.32	0.26	2.59	0.35
1.3 – 2.0	587	122	3.81	0.33	0.26	2.53	0.35
1.6 – 2.0	418	61	5.85	0.43	0.25	2.36	0.35

7.3.2 Uncertainty from the volume size for the signal

In the previous chapter, we investigated the effect of the choice of volume size for the signal V_i using an ensemble of Monte Carlo samples. It was determined that the volume could vary from 1/1000 to 1/3000 of the total volume size without appreciable changes in the fit results. We perform a similar study using the data sample and look for changes in the fit results when different volume sizes are used. The results are shown in Figure 7.1 for volume sizes ranging from 1/1029 and 1/3000 of the total volume size. For all volumes considered, the fit was performed using the

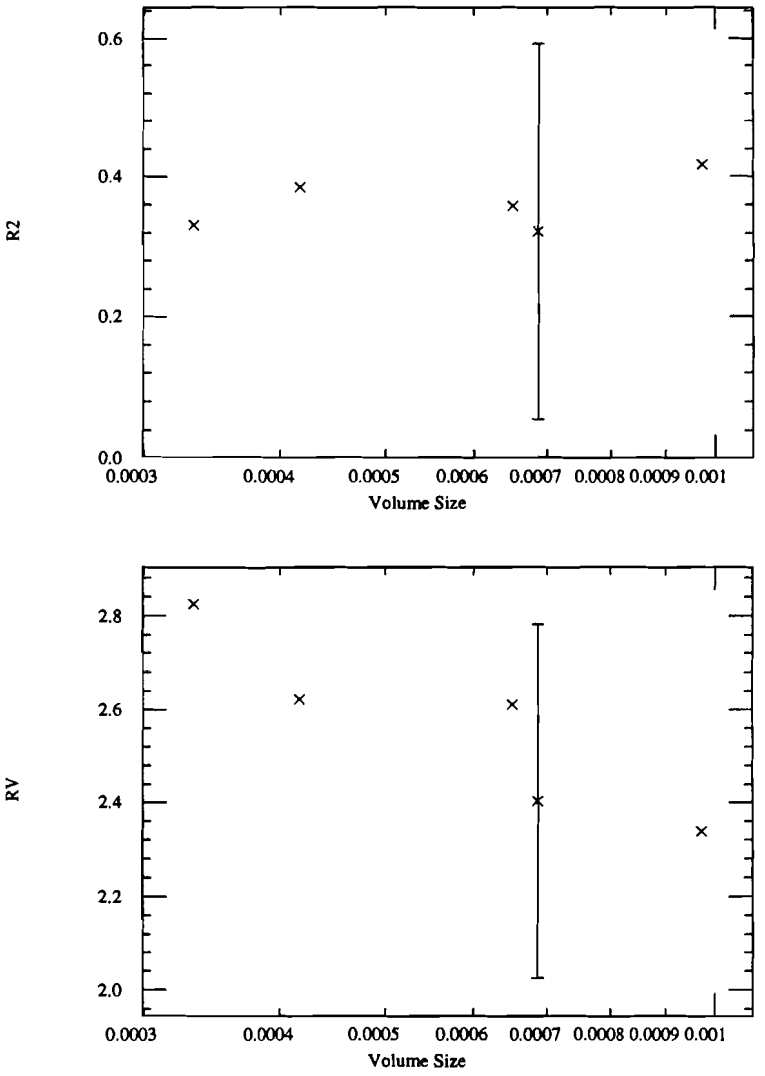

Figure 7.1. Measured value of R_2 (top plot) and R_V (bottom plot) for various volume sizes for the signal V_i expressed as a fraction of the total volume. The volumes are shown on a logarithmic scale.

four kinematic variables: $\cos\theta_l$, $\cos\theta_V$, q^2 and $M_{K\pi}$. From the plots, we estimate the systematic uncertainty attached to the choice of volume size to be 0.06 for R_2 and 0.20 for R_V.

7.3.3 Uncertainty from the volume size for the background

In equation 6.9, V_i^B is a volume centered around data event i. Wrong-sign events within this volume are used to calculate the likelihood of event i being a background event. The volume size V_i^B must be chosen so that there are sufficient background events within the volume to minimize the statistical uncertainty on the likelihood.

Having relaxed the m_{min} cut, we now have more events in our wrong-sign event sample which we can use to test the effect of varying the volume size when fitting to the background. The motivation for using the smaller volume size is to make sure the fit is as sensitive as possible to the distributions of the kinematic variables in the wrong-sign sample. This reduces the uncertainty on each fit parameter as can be seen in Table 7.2. This study also shows that for the tighter m_{min} cut, a change in the volume size for the background introduces a systematic shift of 0.11 for R_2 and 0.07 for R_V for a nominal volume size for the background corresponding to 1/81 of the total volume. This particular choice for the background volume size yields an intermediate value for the fit parameters for each of the three different values of the m_{min} cut. Several other volume sizes were studied and are shown in Figure 7.2. This study indicated that the chosen volume size was reasonable. Two extreme cases are shown: for the first case, we chose V_i^B equal to the total volume. This is equivalent to assuming flat distributions for all kinematic variables for the background. The second case with V_i^B chosen so small that very few points are asscociated with background events corresponds to the assumption that we have a very pure sample. Both these assumptions are deemed unreasonable and we do not consider these two points when evaluating the systematic uncertainty. The systematic uncertainty associated to the choice of volume size for the background is extracted from Figure 7.2 and evaluated at 0.06 for R_2 and 0.07 for R_V.

7.3.4 Simulation of D momentum in the Monte Carlo

Since this whole analysis rests on comparing the data with a large Monte Carlo sample, it is essential that the Monte Carlo properly simulates the data. In particular, the analysis depends on the accurate simulation of the D momentum in the lab frame for the following two reasons. First, geometric acceptance for the D decay products depends heavily on the D momentum distribution in the lab. Secondly, the momentum of the daughter electron depends on the D lab momentum. In turn, the electron identification efficiency depends on the electron momentum. Figure 7.3 displays normalized distributions for (a) the D momentum and (b) the D momentum transverse

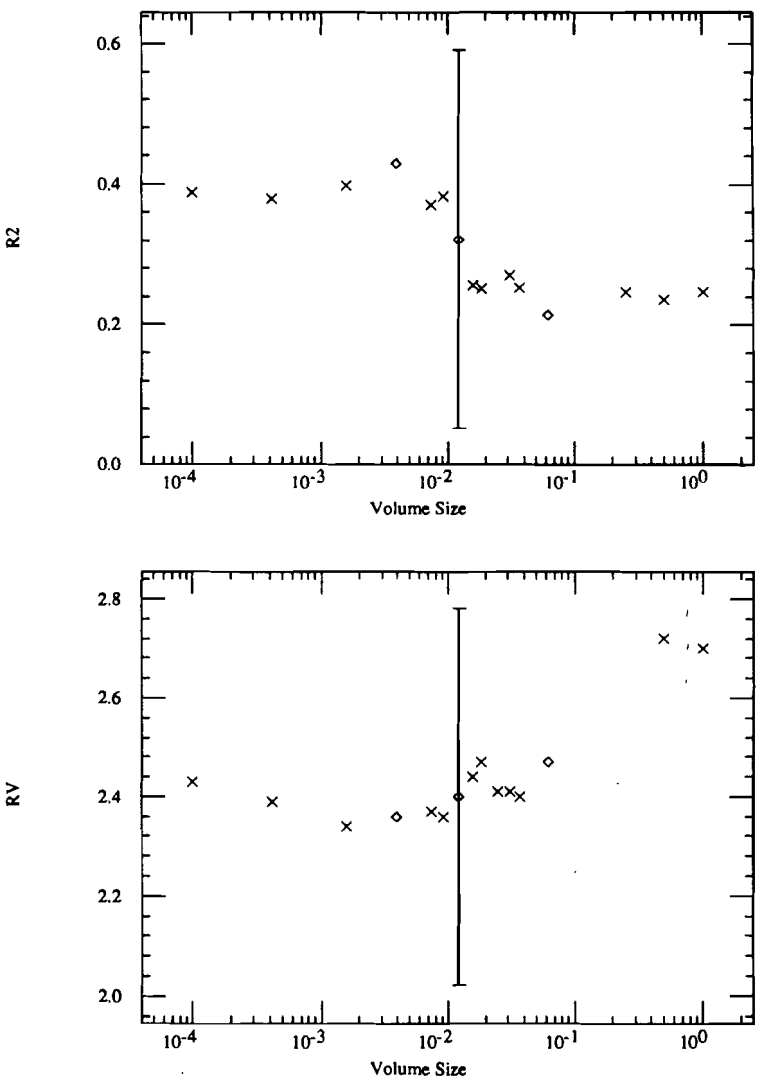

Figure 7.2. Measured value of R_2 (top plot) and R_V (bottom plot) for various volume sizes for the background V_i^B. The volumes are shown on a logarithmic scale.

to the beam axis for both data and Monte Carlo after all selection cuts have been applied. The distributions of the total D momentum agree very well between data and Monte Carlo. The average D momentum transverse to the beam axis is higher in data than in Monte Carlo. However, the effect is not very significant. Hence, no contributions to the systematic uncertainty will be associated with the simulation of the D momentum in the Monte Carlo.

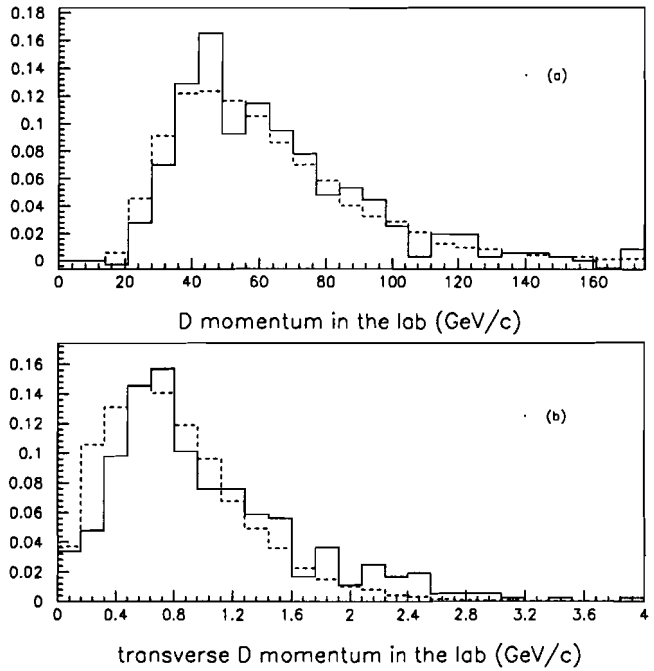

Figure 7.3. The normalized distributions of (a) the total D momentum and (b) momentum transverse to the beam axis for wrong-sign subtracted data (solid curve) and for Monte Carlo (dashed curve) after all selection criteria have been applied.

7.4 Systematic Corrections

All the effects discussed in the previous section introduce some uncertainty in the final value of the measured parameters R_2 and R_V. In addition, the fitting procedure can produce systematic shifts in the measured values of the parameters. If so, the final results from the data will have to be corrected to account for these shifts. This effect will be quantified now.

If there was no systematic bias, the fitting procedure should, on average, return the "true" values of the parameters when using an ensemble of several Monte Carlo samples. From Table 3 in chapter 6, one realizes that there is no sign of a systematic shift for R_2 when we performed the fit using the measured (*i.e.*, smeared) values of the kinematic variables and the negative solution but a difference of two σ between the "true" and measured values of R_V. This can easily be seen in Figure 3 in chapter 6.

To better quantify these systematic shifts, we generated about 133,000 Monte Carlo events with R_2 at 0.26 and R_V at 2.7, values chosen close to the values measured in the data. Of those events, 1554 passed all selection criteria. We used four independent samples of 357 events each and performed the fit four times. The results are compiled in Table 7.3. Again, we observe a systematic shift for the mean value of the fit parameters, even though the statistical uncertainty on this measurement is much larger than for the larger Monte Carlo sample. Until further investigation is completed, no correction will be made to the data to correct for a possible systematic shift.

Table 7.3. Results of the fit to two different ensembles of Monte Carlo samples. The first set of 31 samples corresponds to 1,137,300 events generated with $R_2 = 0.82$ and $R_V = 2.0$. The second set of 4 samples corresponds to about 133,000 Monte Carlo events produced with $R_2 = 0.26$ and $R_V = 2.7$. In each case, the sample of Monte Carlo events generated with R_2=0.82 and R_V=2.0 was used to perform the fit.

parameter	true value	$\langle\mu\rangle \pm \sigma_{\langle\mu\rangle}$
R_2	0.82	0.83 ± 0.05
R_v	2.0	2.12 ± 0.06
R_2	0.26	0.53 ± 0.15
R_v	2.7	2.50 ± 0.23

7.5 Systematic Uncertainty

All contributions to the systematic uncertainty are listed in Table 7.4. The total systematic uncertainty is calculated by adding the individual contributions in quadrature and is shown in Table 7.4. At this point, the uncertainty on our measurement is dominated by statistical uncertainty. All of these contributions, although systematic in nature, will be substantially reduced when more data becomes available. For example, with a larger sample of wrong-sign events available, one could reduce the uncertainty attached to the choice of volume size for the background, V_i^B, by performing more tests to determine the optimal volume size. One can also produce more Monte Carlo events to reduce the systematic uncertainty due to choice of V_i

and the systematic shift. In particular, the uncertainty on the systematic correction can be reduced by generating large samples of Monte Carlo events with values of the form factor ratios close to the measured values in the data, after correction. This is particularly crucial for R_2.

Table 7.4. Various contributions to the systematic uncertainty. All these contributions are added in quadrature.

source	contribution to σ_{R_2}	contribution to σ_{R_V}
m_{min} cut	0.10	0.16
size of V_i	0.06	0.20
size of V_B^i	0.06	0.07
systematic uncertainty	0.13	0.27

7.6 Conclusion

The final values of the form factors ratios are shown in Table 7.5 along with previous experimental measurements. We have improved the maximum likelihood technique method [2] by introducing ensembles of Monte Carlo samples to determine sources of systematic uncertainties, and using the wrong-sign events to fit to the background. When the full E791 data becomes available, these improvements will allow the E791 collaboration to make the most accurate measurement of the form factor ratios. Based on this partial sample (15% of E791 full data sample), we project that the statistical uncertainty can be reduced to about ± 0.10 for R_2 and ± 0.15 for R_V. The size of the systematic uncertainty should be comparable.

Table 7.5 Comparison of the E791 measurements of R_2 and R_V with previous experimental measurements from other experiments [10,11,12].

Group	R_2	R_V	# of events used for measurement
E687	$0.78 \pm 0.18 \pm 0.10$	$1.74 \pm 0.27 \pm 0.28$	875
E653	$0.82^{+0.22}_{-0.23} \pm 0.11$	$2.00^{+0.34}_{-0.32} \pm 0.16$	≈ 275
E691	$0.0 \pm 0.5 \pm 0.2$	$2.0 \pm 0.6 \pm 0.3$	183
E791	$0.32\ ^{+0.26}_{-0.27} \pm 0.13$	$2.4\ ^{+0.39}_{-0.37} \pm 0.27$	357

October 1993: The author in full thesis defense attire

REFERENCES

1. *Semileptonic B and D decays in the quark model,* N. Isgur, D. Scora, B. Grinstein, and M. B. Wise, Phys. Rev. D 39, 799 (1989).
2. *Analysis of semileptonic decays of mesons containing heavy quarks,* F.J. Gilman and R.L. Singleton, Phys. Rev. D 41, 142 (1990).; T. Altomari and L. Wolfenstein, Phys. Rev. Lett. 58, 1583 (1987); T. Altomari and L. Wolfenstein, Phys. Rev. D 37, 681 (1988)
3. *Form factor effects in exclusive D and B decays,* M. Bauer and M. Wirbel, Z. Phys. C 42, 671 (1989).
4. *Exclusive semileptonic decays of bottom mesons in the spectator quark model,* J. G. Korner and G. A. Shuler, Z. Phys. C 38, 511 (1988).
5. *Weak transition form-factors between heavy mesons,* Nathan Isgur and Mark B. Wise, Phys. Lett. B 237, 527 (1990).
6. *New symmetries of the strong interaction in Heavy Quark Physics; recent development by Isgur and Wise,* Patricia Burchat, University of California at Santa Cruz. Presented at the E791 Physics Workshop, Santa Cruz, CA, July 1992.
7. *Relationship between form factors in semileptonic anti-B and D decays and exclusive rare anti-B meson decays,* Nathan Isgur and Mark. B. Wise, Phys. Rev. D 42, 2388 (1990).
8. *Evidence for Penguins: First observation of* $B \to K^*(892)\gamma$, R. Ammar *et al.*, the CLEO collaboration, Phys. Rev. Lett. 71, 674 (1993).
9. *Semileptonic decays of heavy flavors,* D. Bortoletto, Talk given at the 1992 Physics in Collision Conference, Boulder, Colorado, 1992, Purdue University preprint PU-92-662.
10. *Analysis of the decay mode* $D^+ \to \bar{K}^{*0}\mu^+\nu_\mu$, P. L. Frabetti *et al.*, E687 Collaboration, Phys. Lett. B 307, 262 (1993).
11. *Measurement of the form factor ratios in the decay* $D^+ \to \bar{K}^*(892)^0\mu^+\nu$, K. Kodama *et al.*, E653 Collaboration, Phys. Lett. B 274, 246 (1992).
12. *Measurement of the form factors in the decay* $D^+ \to \bar{K}^{*0}e^+\nu_e$, J.C. Anjos *et al.*, E691 Collaboration, Phys. Rev. Lett. 65, 2630 (1990).
13. *Measurement of the hadronic structure of semileptonic* D^0 *and* D^+ *decays,* Z. Bai *et al.*, Mark III Collaboration, Phys. Rev. Lett. 66, 1011 (1991).
14. *A study of the semileptonic decay* $D^+ \to \bar{K}^{*0}e^+\nu_e$, M. Adamovich *et al.*, WA82 Collaboration, Phys. Lett. B 268, 142 (1991).
15. *Form factors of semileptonic D decays from QCD sum rules,* Patricia Ball, V. M. Braun, and H. G. Dosch, Phys. Rev. D 44, 3567 (1991).

16. *The calculation of the transition form factor* $D^+ \to \bar{K}^{*0}e^+\nu_e$ *and the Kobayashi-Maskawa matrix element* U_{cs}, T. M. Aliev, V.L Eletskiĭ and Ya. I. Kogan, J. Nucl. Phys. 40, 527 (1984).
17. *Lattice study of semileptonic decays of charm mesons into vector mesons,* C. W. Bernard, A. X. El-Khadra, and A. Sone, Phys. Rev. D 45, 869 (1992).
18. *First calculation of* $D^+ \to \bar{K}^{*0}e^+\nu_e$ *in lattice QCD,* V. Lubicz, G. Martinelli and C. T. Sachrajda, Nucl. Phys. B 356, 301 (1991).
19. *Introduction to experimental particle physics,* R. Fernow, Cambridge Press (1986).
20. Adapted from J. Raab thesis, University of California, Santa Barbara (1987).
21. *Performance of the Čerenkov counters in the Fermilab Tagged Photon Spectrometer facility,* D. Bartlett *et al.*, Nucl. Instr. Meth. A 260, 55 (1987).
22. Review of Particle Properties, Phys. Lett. B 239, III.29 (1990).
23. E791 offline document #44 on Čerenkov detector software, L. Cremaldi, (1992).
24. *A large area liquid scintillation multi-photon detector,* V. K. Bharadwaj *et al.*, Nucl. Instr. 228, 283 (1985).
25. *Hadron calorimetry at the Fermilab Tagged Photon Spectrometer Facility,* J. Appel *et al.*, Nucl. Instr. Meth. A 243, 361 (1986).
26. *The E791 parallel architecture data acquisition system,* S. Amato *et al.*, Nucl. Instr. Meth. A 324 535 (1992).
27. *EMPNEW,* R. J. Morrison, E691 memo, Feb.4, 1987.
28. *Study of electron identification efficiencies,* R. J. Morrison, E691 memo, Feb. 9, 1987.
29. *Electron identification efficiencies,* J. E. Duboscq, E691 memo, Oct. 14, 1987.
30. *Reconstruction of a strip geometry calorimeter xsing stepwise regression,* D. Summers, Nucl. Instr. Meth. 228, 290 (1985).
31. *Experimental study of the semileptonic decay* $D^+ \to \bar{K}^{*0}e^+\nu_e$, J. C. Anjos *et al.*, E691 collaboration, Phys. Rev. Lett. 62, 722 (1989).
32. *Review of particle properties,* Phys. Rev. D 45, III-32 (1992).
33. *A general method of estimating physical parameters from a distribution with acceptance and smearing effects,* D. M. Schmidt, R. J. Morrison, M. S. Witherell, Nucl. Instr. Meth. A 328, 547 (1993).
34. *Form factor analysis in E691 data,* D. M. Schmidt thesis, University of California at Santa Barbara, 1992.
35. *MINUIT function minimization and error analysis reference manual,* Application Software Group, Version 92.1, CERN (1992).